PADERBORN UNIVERSITY
The University for the Information Society

Remote Heteroepitaxy of $In_xGa_{1-x}As$ on graphene covered GaAs-(001) substrates

Presented to the Faculty of Science
Department of Physics
Paderborn University

In partial fulfilment of requirements
for the degree of
Dr. rer. nat.

Dissertation

by

Tobias Henksmeier

5th November 2021

Doctoral committee:
Prof. Dr. Dirk Reuter
Prof. Dr. Artur Zrenner
Prof. Dr. Wolf Gero Schmidt
Dr. Christof Eigner

Abstract

The heteroepitaxial growth of lattice mismatched films is crucial for modern semiconductor device fabrication, but it is a significant challenge in epitaxy. Growth of lattice mismatched materials creates strain in the epitaxial layer, which is usually relaxed by introducing crystal defects deteriorating the device performance. Remote epitaxy on graphene covered substrates was recently proposed to offer a different relaxation pathway for the strained films.

In this thesis, remote heteroepitaxy growth by molecular beam epitaxy of $In_xGa_{1-x}As$ films ($0 < x \leq 0.5$) on transfer graphene covered GaAs-(001) substrates is investigated for the first time.

First of all, the wet transfer of CVD-monolayer-graphene onto freshly oxide stripped GaAs-(001) oriented substrates is investigated. XPS-measurements reveal, that the GaAs substrate re-oxidises during wet graphene transfer in agreement with reports from literature. A careful optimised short and mild H+Ar-plasma treatment followed by thermal annealing in UHV removes the oxide layer. Raman-spectroscopy reveals a mainly intact graphene monolayer after this treatment.

Secondly, molecular beam epitaxy of $In_xGa_{1-x}As$ was performed on the graphene-covered GaAs-(001) substrates. Detailed studies on the nucleation of the $In_xGa_{1-x}As$ layers ($0 < x \leq 1.0$) reveal remote epitaxial island growth on the graphene-covered GaAs substrate. The coalescence of the nuclei is observed at a nominal coverage of about 5 nm and indium fractions $x \leq 0.50$.

200 nm thick $In_xGa_{1-x}As$ films ($0 < x \leq 0.5$) are grown by an one-step and a two-step process on graphene-covered GaAs substrates and also on bare GaAs substrates for comparison. HRXRD and TEM measurements

show crystalline growth on large areas with the same crystal orientation as the substrate. Detailed studies on the strain relaxation of 200 nm thick films on graphene covered GaAs and for comparison on bare GaAs are presented. Films grown on graphene show homogeneous and stronger relaxation, while films grown on bare GaAs show stronger relaxation along the [110]-direction. These films also exhibit a well known tilt, in contrast to films grown on graphene-covered GaAs.

Kurzfassung

Das heteroepitaktische Wachstum von gitterfehlangepassten Schichten ist für die Herstellung moderner Halbleiterbauelemente von entscheidender Bedeutung, stellt jedoch eine große Herausforderung für die Epitaxie dar. Das Wachstum gitterfehlangepassten Materialien führt zu Spannungen in der Epitaxieschicht, die in der Regel durch die Einführung von Kristalldefekten abgebaut werden, was die Leistung der Bauelemente beeinträchtigt. Kürzlich wurde die Remote-Epitaxie auf mit Graphen bedeckten Substraten vorgeschlagen, um einen anderen Entspannungsweg für die verspannte Schichten zu bieten.

In dieser Arbeit wird zum ersten Mal die Remote-Heteroepitaxie von $In_xGa_{1-x}As$-Filmen ($0 < x \leq 0,5$) auf mit Graphen bedeckten GaAs-(001)-Substraten durch Molekularstrahlepitaxie untersucht.

Zunächst wird der Nasstransfer von CVD-Monolagen-Graphen auf frisch geätzten GaAs-(001) orientierten Substraten untersucht. XPS-Messungen zeigen, dass das GaAs-Substrat während des Graphen-Transfers korrodiert, was mit Berichten aus der Literatur übereinstimmt. Eine sorgfältig optimierte, kurze und milde H+Ar-Plasmabehandlung, gefolgt von einem Ausheizschritt im UHV, entfernt die Oxidschicht. Die Raman-Spektroskopie zeigt, dass das Graphen nach dieser Behandlung weitgehend intakt ist.

Danach wurde die Molekularstrahlepitaxie von $In_xGa_{1-x}As$ auf den mit Graphen bedeckten GaAs-(001)-Substraten durchgeführt. Detaillierte Untersuchungen zur Keimbildung der $In_xGa_{1-x}As$-Schichten ($0 < x \leq 1.0$) zeigen ein remote-epitaktisches Inselwachstum auf dem mit Graphen bedeckten GaAs-Substrat. Das Zusammenwachsen der Keime wird bei einer nominalen Bedeckung von etwa 5 nm und Indiumanteilen $x \leq 0,50$ beobachtet.

200 nm dicke $In_xGa_{1-x}As$-Filme ($0 < x \leq 0,5$) werden in einem einstufigen und einem zweistufigen Verfahren auf mit Graphen bedeckten GaAs-Substraten und zum Vergleich auch auf blanken GaAs-Substraten gezüchtet. HRXRD- und TEM-Messungen zeigen ein kristallines Wachstum auf großen Flächen in gleicher Kristallorientierung wie das Substrat. Detaillierte Untersuchungen zur Verspannungsrelaxation von 200 nm dicken Schichten auf mit Graphen bedecktem GaAs und zum Vergleich auf blankem GaAs werden vorgestellt. Auf Graphen gewachsene Schichten zeigen eine homogene und stärkere Relaxation von bis zu etwa 44%, während auf blankem GaAs gewachsene Schichten eine stärkere Relaxation entlang der [110]-Richtung zeigen. Diese Filme weisen auch eine wohl bekannten Verkippung auf, im Gegensatz zu Filmen, die auf mit Graphen bedeckten GaAs gewachsen sind.

Contents

Chapter 1

Introduction

Nowadays, semiconductor heterostructures play a major role in many optoelectronic devices. The integration of different materials has always been of great interest to combine their individual intrinsic electronic and optical properties and create new device functionalities. However, heteroepitaxy suffers from the lattice mismatch of different semiconductors, especially between film and substrate, causing a strained film. This strain is plastically relaxed above a critical thickness, by the formation of dislocations in the epitaxial film deteriorating the optical and electrical performance. Thick metamorphic buffers with various grading schemes have been employed to reduce the dislocation density in the active region of a layer stack [1–3]. In contrast, nearly complete decoupling of layer and film is achieved in van-der-Waals epitaxy [4–9] However, high quality growth of III-As van-der-Waals semiconductor heterostructures such as gallium arsenide (GaAs) or indium gallium arsenide ($In_xGa_{1-x}As$) was not possible so far, due to the low substrate surface potential [8, 9]. The low wettability of the surface and the missing crystal stability without an interacting substrate caused problems.

Recently, remote epitaxy was proposed as a promising approach to weaken the substrate-layer binding by a graphene (mono-)layer placed on the substrate, while still transferring the crystal orientation to the growing layer [10–17]. Layers grown on this graphene covered surface can be peeled-off allowing the fabrication of free-standing semiconductor films and substrate

reuse [10–17]. In the more delicate way of remote heteroepitaxy, a layer slip on the graphene as an alternative strain-relaxation mechanism apart from dislocation introduction was observed [12, 17]. Exceeding a critical strain energy, the layer starts to relax by slipping over the graphene surface instead of forming dislocations [17]. Remote epitaxy by metalorganic chemical vapor deposition (MOCVD) of several semiconductor material combinations has been demonstrated, e. g., GaAs on GaAs [10, 11], gallium nitride (GaN) on GaN or on silicon carbide (SiC) [13,17], indium gallium phosphide (InGaP) and gallium phosphide (GaP) on GaAs [17]. Often, a dry transfer method was employed to transfer monolayer graphene to the substrates rather than the simpler wet transfer method of chemical vapour deposition (CVD)-graphene [18]. During wet transfer, the freshly oxide striped GaAs substrate re-oxidises and thus prevents remote epitaxy [18]. However, commercially available CVD transfer graphene is arguably the simplest way to cover large substrate areas, even entire wafers, with graphene.

In this dissertation, a study of remote heteroepitaxy by solid-source molecular beam epitaxy (MBE) of $In_xGa_{1-x}As$-films on CVD-monolayer-graphene covered GaAs-(001) substrates is presented. A plasma assisted preparation method to remove surface oxides from the GaAs after graphene transfer and polymer residuals from the graphene is elaborated. The nucleation of $In_xGa_{1-x}As$-films ($0 < x \leq 1.0$) on graphene covered GaAs is investigated as well as growth of 200 nm thick $In_xGa_{1-x}As$ ($0 < x \leq 0.5$) films. An one-step growth approach is compared to a two-step growth approach.

All necessary fundamental properties to understand this thesis are elaborated in the chapter *Fundamentals*. The crystallographic structure of GaAs and $In_xGa_{1-x}As$ is derived. Then, the basic properties of heteroepitaxial growth are elaborated. Thermodynamic and atomistic-kinetic considerations are presented and the strain relaxation mechanism by the introduction of crystal defects in mismatched systems is discussed. Further, the basic principle and the necessary conditions for successful remote epitaxy are described.

Lastly, the reciprocal space is employed with a focus on its application in high-resolution X-ray diffraction (HRXRD) and reflection high-energy electron diffraction (RHEED).

In chapter *Experimental set-up*, an in-depth description of the used measurement techniques MBE, reactive-ion etching (RIE), atomic force microscopy (AFM), HRXRD, scanning electron microscopy (SEM), transmission electron microscopy (TEM), X-ray photoelectron spectroscopy (XPS) and Raman-spectroscopy is presented.

In the fourth chapter, *Graphene transfer and sample preparation*, the graphene transfer to freshly oxide striped GaAs substrates is elaborated. The methods and parameters for cleaning the graphene from polymer residuals and the GaAs from surface oxides are described.

The major part of this thesis is chapter 5, *Results*. Within the first section, the GaAs-graphene surface cleaning by thermal annealing and mild plasma cleaning is discussed. A method to prepare wet transferred graphene for remote epitaxy is derived. In the second part, the nucleation behaviour of $In_xGa_{1-x}As$ ($0 < x \leq 1.0$) on graphene covered GaAs is discussed. SEM images of the sample surface and TEM images of individual nuclei are analysed. Finally, the growth of thicker $In_xGa_{1-x}As$ films ($0 < x < 0.5$) by a one- and a two-step process are investigated. Their crystallographic properties and surface morphologies are analysed by HRXRD measurements, Raman-spectroscopy and AFM measurements, respectively.

Lastly, the results are concluded and an outlook for future investigations is given in the *Conclusion and Outlook*.

Chapter 2

Fundamentals

In the following chapter, the fundamental physical properties and characteristics that are necessary to understand this thesis are elaborated. Firstly, the fundamental physical properties of GaAs and $In_xGa_{1-x}As$ are described and a brief overview of their crystallographic structure is given. Secondly, the basic principles of heteroepitaxy are discussed. Atomistic-kinetic and thermodynamic aspects of layer nucleation and growth are derived. The strain relaxation mechanism in lattice-mismatched systems with a focus on GaAs/$In_xGa_{1-x}As$ is presented, followed by an overview on defects and dislocations. Then, the basic principles of remote epitaxy are described. The layer-substrate separation by a monolayer graphene is highlighted. Lastly, the reciprocal space is introduced. Its application to investigate crystal structures by X-ray diffraction and electron diffraction is described.

2.1 Properties of GaAs and $In_xGa_{1-x}As$

In the following section, the basic properties of III-As semiconductors with a focus on GaAs and $In_xGa_{1-x}As$ are discussed. The crystallographic structure and the band structure are described.

III-V semiconductors and especially III-As semiconductor heterostructures are decent building blocks for the fabrication of modern optoelectronic devices. Widely spread examples are laser diodes and detectors, but also

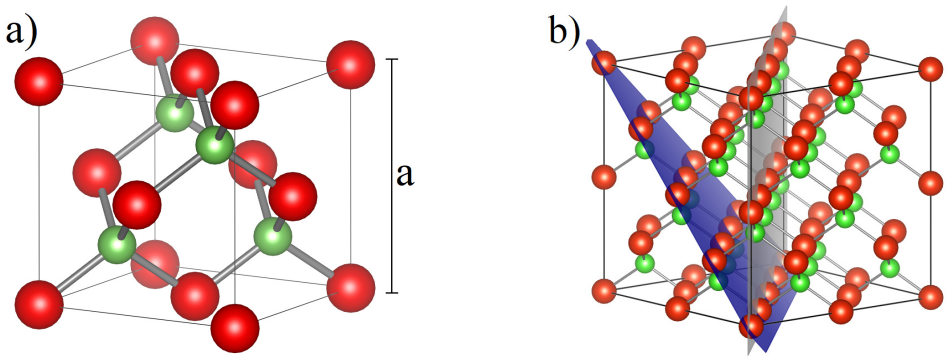

Figure 2.1: a) Unit cell structure in a zinc blende crystal. b) The important (111) and (110) planes are sketched within the crystal lattice in blue and grey, respectively.

$In_xGa_{1-x}As$ quantum dot heterostructures may be used as single photon sources in future applications [19–24]. $In_xGa_{1-x}As$ containing heterostructures operating in the telecommunication bandwidth offer a wide application range [20–22]. Investigation on $In_xGa_{1-x}As$ began in the early 1970s with the development of light-emitting diode sources on GaAs substrates and a few years later on InP substrates [24]. Later, laser structures and high-speed field-effect transistors were manufactured [24]. Most structures are grown on InP and GaAs substrates. While $In_{0.53}Ga_{0.47}As$ is lattice matched to InP, all other compositions exhibit a lattice-mismatch with respect to the substrates and are strained [24]. The strain is mostly relaxed by the introduction of dislocations. Thick $In_xGa_{1-x}As$ buffer layers are required to relax the strain in a controlled way and to separate the active region from the dislocations [20–22, 24].

The thermodynamically stable phase of GaAs and $In_xGa_{1-x}As$ is the zincblende structure with a diatomic base, as exemplarily shown in figure 2.1 for a GaAs crystal. There are two face-centred-cubic (fcc) lattices, one shifted by a quarter of the lattice constant along the space diagonal. One lattice is occupied by Ga cations, the other by As anions [20–22]. The atoms are tetrahedrally coordinated, i.e. a Ga atom is bonded to four As atoms and vice versa. This results in an AaBbCc layer stacking sequence of the two sub-lattices where the cations and anions exhibit the ABC and abc stacking,

respectively. The {110} crystal facets are of special interest, as they consist of the same number of anions and cations. They are non-polar and exhibit the weakest bond [20–22]. The crystal can be easily cleaved along these planes. The {111} planes play an important role in layer strain relaxation, which is described later in more detail [20–22]. In figure 2.1, a sketch of the (111) and (110) surface in a zincblende crystal is shown.

The length of the unit cell depicted in figure 2.1 is the lattice constant. GaAs exhibits a lattice constant of around $a = 5.6533$ Å and InAs of $a = 6.0584$ Å at room temperature, respectively [25, 26]. An $In_xGa_{1-x}As$ alloy adopts an intermediate lattice constant, depending on the indium fraction x, which is calculated by a linear interpolation referred to as Vegard's rule [27]. It describes the behaviour of an alloy crystal lattice constant concerning the concentrations of the constituent elements. The lattice constant of an alloy formed by two different materials A and B with the same crystal structure and lattice the constants a_A and a_B, respectively, is hence given by equation (2.1) and especially in the case of $In_xGa_{1-x}As$ by equation (2.2).

$$a_{alloy} = a_a x + a_b(1 - x) \tag{2.1}$$

$$a_{InGaAs} = a_{InAs} x + a_{GaAs}(1 - x) \tag{2.2}$$

Besides the lattice constant, the direct band gap of a crystal at the Γ-point, is an important parameter dictating the optical and electrical characteristics of a material, for example, the light absorption and emission wavelength. The usability of a usual semiconductor as GaAs ($E_{g,300K} = 1.424$ eV [25]) or InAs ($E_{g,300K} = 0.354$ eV [26]) is thus very limited, because their band gap cannot be tuned. However, combining both semiconductors opens a rather large band gap window. The band gap E_{alloy} of the alloy lies between the band gap of the individual semiconductors and is calculated by the empirical quadratic relation from equation (2.3) [20–22]. Especially for $In_xGa_{1-x}As$, equation (2.4) is obtained with the bowing factor $b = 0.477$ [21]. The band gap is tuned, by choosing the composition x of both materials.

$$E_{g,alloy} = E_{g,A} x + E_{g,B}(1 - x) - bx(1 - x) \tag{2.3}$$

$$E_{g,InGaAs} = E_{InAs}x + E_{GaAs}(1-x) - 0.477x(1-x) \tag{2.4}$$

The technologically important value of $E_g = 0.8$ eV $\widehat{=}\lambda = 1.55$ μm is calculated to approximately 47% indium by equation (2.4) [24]. A semiconductor's band gap energy usually decreases with increasing temperature, as the atomic vibrations amplitude increases. The band gap temperature dependence is described by the Varshni-equation (2.5) [28]. Here, the coefficients α and β are material-related constants determined experimentally.

$$E_g = E_{g,0K}x + \frac{\alpha T^2}{T+\beta} \tag{2.5}$$

2.2 Properties of Heteroepitaxy

The manufacturing of tailored heterostructures requires a highly controllable method. Thin film growth of a crystalline film on a crystalline substrate, where the orientation of the substrate is transferred to the film is known as epitaxy. Heteroepitaxy refers to the case, when layer and substrate material differ and homoepitaxy refers to the case, when film and substrate are the same material [21]. There are several epitaxy methods, the most prominent ones are probably MOCVD, liquid phase epitaxy (LPE), and MBE. A proper overview of these methods is given in [21, 29]. The following description is related to these books. All samples discussed in this dissertation are grown via MBE. MBE is performed by evaporating materials from individual solid sources to generate a molecular beam towards the heated substrate. Growth is performed in ultra-high vaccum (UHV), to reduce the incorporation of parasitic atoms in the film [21]. A more detailed description is presented in chapter 3.

The driving force of crystallisation is the difference in the chemical potential of the gaseous and the solid (crystalline) phase. Crystal growth occurs if the potential is lower in the solid phase [21, 29, 30]. It is controlled by several process parameters, like the substrate temperature, the molecular beam flux, and strongly depends on the materials properties. Some general trends of epitaxial crystal growth are drawn by thermodynamic and atomistic-kinetic

models. Usually, thermodynamics describe collective motions of particles in terms of macroscopic growth affinity [21]; for example, the nucleation and formation of islands on the substrate or the description of layer-by-layer growth. However, growth conditions are sometimes far from equilibrium and are more better described by atomic-kinetic considerations, especially on a short time scale and at atomic distances [21, 29, 30]. Exemplarily is the surface reconstruction during growth or the molecule migration on the sample surface.

In the following part, some general kinetic considerations are discussed [21, 29, 30]. Molecules adsorbed on the crystal substrate surface, where they diffuse. After a certain migration time, they may meet other migrating atoms to nucleate, or they re-evaporate, or they are incorporated in the crystal lattice at kinks and etches, or they are captured by nuclei. Figure 2.2 gives an overview of the various processes. For layer growth, the nucleation and incorporation of adatoms is important. Small nuclei will either loose atoms, or acquire more atoms and grow above a critical thickness, where they are stable at normal growth conditions [21, 29, 30]. The probability p of process occurrences is well described by a temperature activated Arrhenius term from equation (2.6); with the temperature T, the probability constant p_0, the Boltzman-constant k_B and the activation energy of the process ΔE.

Impinging atoms diffuse in a random walk process consisting of a jump series to respective adjacent substrate sites on the sample surface. Their diffusion length λ exhibits an Arrhenius like behaviour and is calculated by equation (2.7) [21, 29, 30].

$$p = p_0 \exp\left(\frac{-\Delta E}{kT}\right) \tag{2.6}$$

$$\lambda(T) = \lambda_0 \exp\left(\frac{E_a - E_d}{2k_B T}\right) \tag{2.7}$$

Therefore, the surface diffusion length λ of an adsorbed atom only depends on the temperature T and the difference between the adsorption activation energies E_a and the diffusion barrier E_d. At high temperatures, the surface diffusion length λ decreases exponentially with T as the adsorption

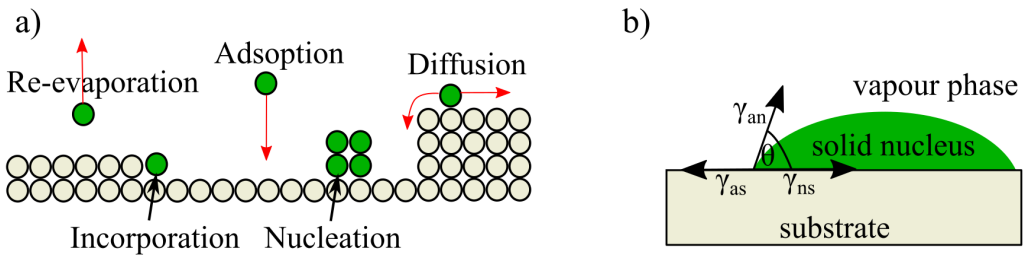

Figure 2.2: a) Sketch of the kinetic processes on a sample surface. b) Sketch of a nucleus on a substrate. The surface tension determines the nuclei shape and the surface wettability.

time is short and thus adatomes are likely to evaporate before being incorporated in the crystal. For low temperatures, the re-evaporation becomes negligible, and the atoms stay longer on the surface before they are incorporated. However, the diffusion length also decreases for too low temperatures. The smoothest films are obtained for temperatures, where the diffusion length is large and the temperature is slightly below the temperature for which significant re-evaporation occurs [21, 30].

From the perspective of macroscopic layer growth affinity, layer growth starts with the nucleation on the substrate in the initial stage of growth, followed by continuous layer growth. Some energy is released by the partial destruction of the pre-existing substrate surface through heterogeneous nucleation of small nuclei [21, 29]. If a potential nucleus is too small, the energy that would be released by forming its volume is not enough to create its surface, and nucleation does not proceed [21]. Thus, nucleation is energetically unfavourable below a critical nucleus size, due to the unfavourable creation of the boundary to the initial phase [21]. Only large enough nuclei are stable. The nuclei shape strongly depends on the substrate nucleus interface, i.e. on the material wettability on a substrate surface. Regarding Young's relation, the absolute values of surface tension amongst nucleus (n), substrate (s) and ambient phase (a) in balance determine the wetting angle Θ by $\gamma_{as} = \gamma_{ns} + \gamma_{an} \cos\Theta$ [31]. A schematic sketch is presented in figure 2.2b). Usually, it is aimed for the growth of smooth films in epitaxy and thus a high wettability and a low wetting angle is favourable, respectively. In this

case, a large area of the substrate is covered by the deposited material and growth occurs in a layer-by-layer fashion also referred to as Frank-van der Merve growth mode [30]. In contrast, if the deposited atoms are stronger attracted to each other than to the substrate, the substrate wettability is small and separate nuclei are grown on the substrate [21]. This three-dimensional island growth is referred to as Volmer-Weber growth mode [30]. The surface energy of the layer plus substrate is minimised, if a maximum of the substrate surface is not covered by the deposited material [30]. A special case is the Stranski-Krastanow growth mode, which is famous for the growth of defect-free InAs quantum dots on GaAs [21, 30]. Here, the growth starts in the Frank-van der Merve growth and after exceeding a critical coverage thickness, the mode changes to the three-dimensional Volmer-Weber mode. Due to the high lattice mismatch, strain is accumulated in the wetting layer, which is then released by the three-dimensional growth [21, 29].

Once the film growth has started, there is an adoption of the film lattice to the substrate lattice. Heteroepitaxial film growth of a material with a lattice constant a_l on a substrate with a lattice constant a_{sub} results in a strained film. The relative difference between the substrate and film lattice constant is called misfit f_0 and is calculated by equation (2.8) [20, 21].

$$f_0 = \frac{a_{sub} - a_l}{a_l} \tag{2.8}$$

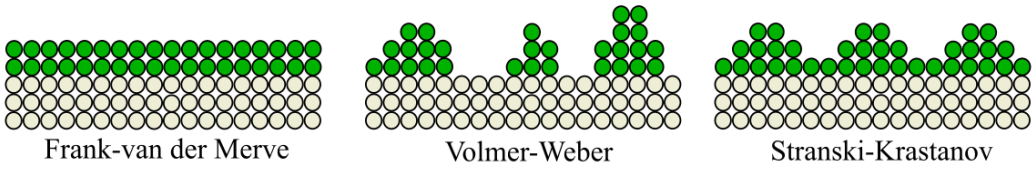

Figure 2.3: Different layer growth modes are presented. A low substrate wettability of the deposited material results in island growth (Volmer-Weber growth mode), whereas a high wettability results in layer-by-layer growth (Frank-van der Merve growth mode). A special case is the Stranski-Krastanow growth mode. Here, the growth starts in the layer-by-layer growth and at some point changes to the island growth mode.

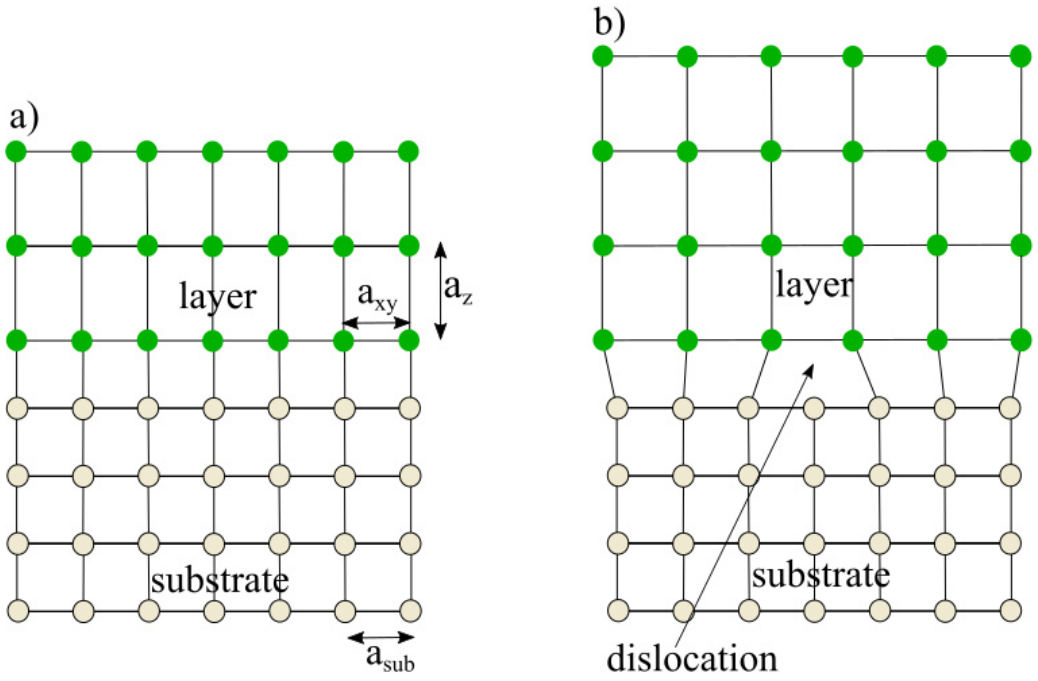

Figure 2.4: a) Schematic sketch of a pseudomorphic film grown on a substrate with a different lattice constant. b) Above a critical thickness, dislocations are formed to relax the build-up strain and the film is relaxed.

$$E/A = 2G\epsilon_{||}^2 \frac{1+\nu}{1-\nu} \tag{2.9}$$

Considering an $In_xGa_{1-x}As$ film grown on GaAs as depicted in figure 2.3. In the beginning, the $In_xGa_{1-x}As$ layer will adopt the in-plane lattice constant of the GaAs and is compressively strained in the in-plane direction, while being stretched along the growth direction according to Poisson's ratio [20, 21]. The resulting strain energy per area is calculated by equation (2.9). It depends on the in-plane strain $\epsilon_{||}$, the shear modulus G, the Poisson' ratio ν and the material related quantities [20, 21]. During growth the strain energy increases and at a critical thickness the built-up energy is large enough, to introduce plastic relaxation by a distortion of the film lattice [21]. Dislocations are formed. Dislocations not only influence the crystal structure, but also the electrical and optical characteristics of semiconductor devices. Heteroepitaxial $In_xGa_{1-x}As$ film growth on GaAs is known to exhibit dislocations above a certain critical thickness. However, the conditions during

MBE growth are often far from equilibrium, so that the critical thickness is more an estimation for the onset of dislocations than a fixed value. The growth rate and the substrate temperature play an important role in layer relaxation as shown in [32–34].

2.3 Defects in III-As films

In general, there is a variety of defects such as dislocations, stacking faults, grain and twin boundaries that may occur in heteroepitaxial grown films. Here, a brief description of the important defects in zinc blende $In_xGa_{1-x}As$ and GaAs is presented. For an in-depth discussion, please refer to [35].

Dislocation can be introduced in a crystal, when the build-up strain energy in lattice mismatched films becomes too large and is plastically relaxed. Dislocations are line defects along which the crystal is shifted by a certain amount [20,35]. The line vector $\vec{l}$ lies along the dislocation line and the difference of a closed path around the dislocation with respect to an ideal crystal is the Burger's vector $\vec{b}$. Most prominent in the zincblende system are the edge ($\vec{b} \perp \vec{l}$), screw ($\vec{b} \parallel \vec{l}$) (schematically sketched in figure 2.5) and 60°-mixed type dislocation. All exhibit a Burger's vector of $\frac{a}{2} \times < 110 >$, so the Burger's vector is a primitive translation of the fcc structure [20]. In contrast, dislocations with other Burger's vectors leading from a lattice site to a crystallographic not equivalent site are referred to as partial dislocations. These lead to a change in the AaBbCc layer stacking order of the {111} planes and thus they introduce stacking faults [21, 35]. The regular stacking is changed by the introduction or omission of one lattice plane, for example in the case of an AaBb|AaBbCc layer stacking. In the zincblende structure, the dislocations may either lie on a row of As anions or Ga, In cations. They are termed α if $\vec{l} \parallel [-110]$ and β if $\vec{l} \parallel [110]$ [20]. It was reported that this different atomic configuration can cause inhomogeneous relaxation behaviour for {111} slip planes [36]. In an ideal crystal, the formation of a dislocation requires energy, as the atom's position is distorted in a small area. The energy of a dislocation is derived from the atom's displacement and the related cost of elastic energy required to form the dislocation. Considering the 60°

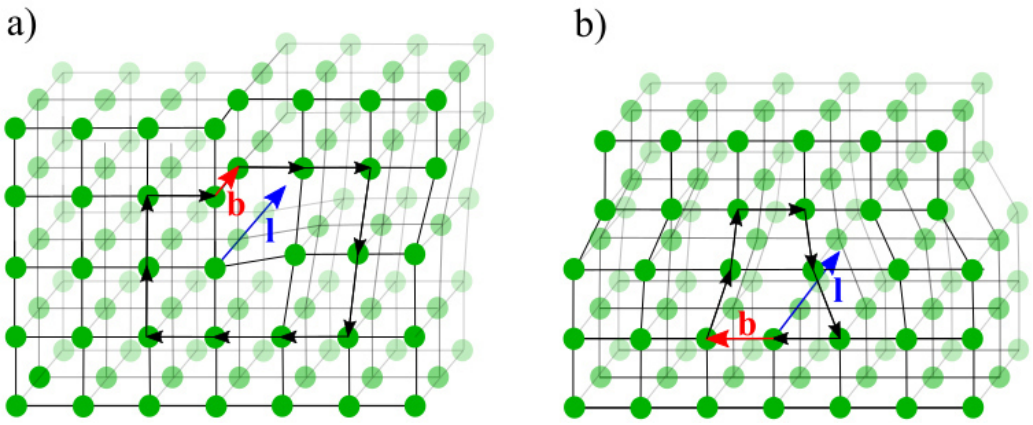

Figure 2.5: Schematic sketch of an edge and a screw dislocation in a film. a) The Burger's vector $\vec{b}$ is collinear to the line vector $\vec{l}$ for a screw dislocation. b) Both vectors are orthogonal for an edge dislocation.

dislocations in the $In_xGa_{1-x}As/GaAs$ system, a general relation of the dislocation energy of a film containing dislocations is given by equation (2.10) with $b = \frac{a}{2} \times [110]$, $\alpha = 60°$ and $\beta = 54.7°$ [21]. G is the layer shear modulus, ν the Poisson's ratio, f_0 the mismatch, ϵ the film's strain and R is the radius of the dislocation.

$$\frac{E_D}{A} = \frac{Gb}{2\pi}\left(\frac{|\epsilon + f_0|(1 - \nu\cos^2\alpha)}{(1-\nu)\sin\alpha\cos\beta}\right)\ln\left(\frac{4R}{b}\right) \tag{2.10}$$

Stacking faults, grain and twin boundaries are also often found in films. A Grain boundary is the interface of two crystallites and often occurs, when individual crystallites grow on a substrate and at some point match [20, 21, 35]. They are usually observed in polycrystalline films. Twin boundaries occur when two crystallites grown with a slight misorientation merge [20, 21, 35]. As a consequence, the crystal stacking order changes. In stacking faults, the local layer's stacking sequence is changed [20, 21, 35]. Stacking faults may origin from defective film nucleation on steps, defects or due to local strain [20, 21, 35].

2.4 Remote Epitaxy

It becomes clear, that defects like dislocations alter the crystal structure and therefore also influence a device performance. State-of-the-art attempts to overcome large lattice mismatches with reduced dislocation densities are metamorphic buffers with various grating schemes or compliant substrates, to reduce the dislocation density in the active region of a film [1–3, 37, 38]. In contrast, nearly complete decoupling of layer and film is achieved in van-der-Waals epitaxy [6–9]. However, due to the low substrate surface potential, successful high quality van-der-Waals epitaxy of III-As semiconductors has not been achieved so far [8,9]. The low wettability of the substrate surface and the missing crystal stability without an interacting substrate poses problems. Recently, remote epitaxy was proposed as a promising approach to weaken the substrate-film binding, but still transferring the crystal orientation to the growing layer [5, 7, 10–13, 17, 18]. A monolayer graphene placed on the substrate introduces a substrate-film-interaction gap as exemplarily shown in figure 2.6a). An $In_xGa_{1-x}As(001)$ film is separated from the GaAs(001) substrate. A top view image in b) shows the graphene layer on top of the GaAs substrate. There is no alignment between the GaAs lattice and the graphene lattice. A monolayer graphene is non-polar and exhibit barely any out-of-plane binding-potential, so it influence on the penetrating substrate potential is low.

Density-functional theory calculations reveal, that the substrate-film binding strength drops significantly with increasing interaction gaps [10, 11]. Figure 2.7 shows the substrate potential fluctuations through 1 and 2 monolayer graphene on GaAs and GaN. The maximum substrate-film separation depends strongly on the material bond ionisities [10, 11]. GaAs exhibits an ionisity of 31%, while GaN and InAs exhibit an ionisity of 50% [10,11,39].The GaAs potential fluctuation amplitude through 1 and 2 monolayer graphene is around 15 meV and 5 meV, respectively. It drops significantly for more than a monolayer graphene and thus remote epitaxy is only possible for 1 monolayer graphene on GaAs, see figure 2.7. In contrast, the potential fluctuation amplitude of GaN through 2 monolayer graphene is even large enough

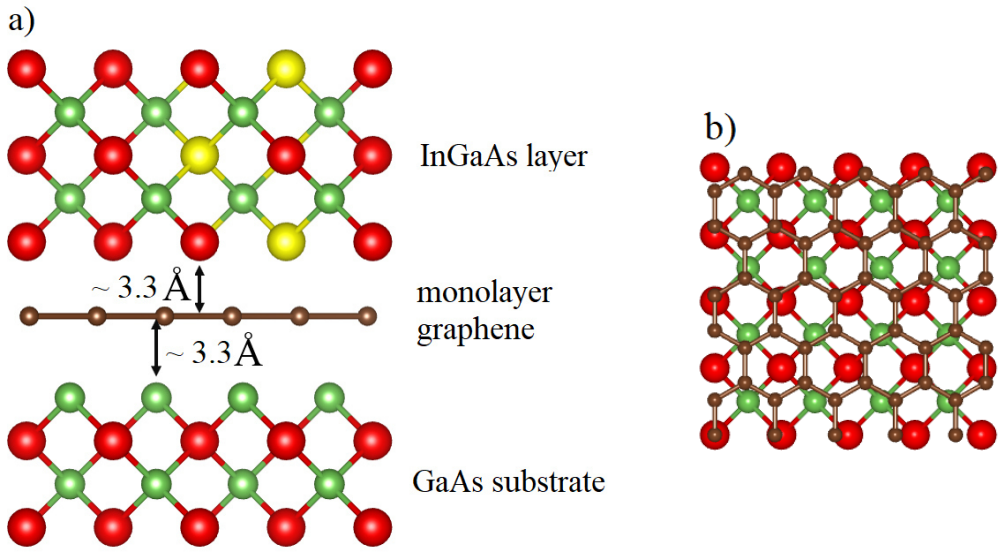

Figure 2.6: a) Schematic sketch of a GaAs substrate-graphene-InGaAs layer stack with the characteristic interaction gap generated by the graphene layer. b) Top view on the graphene covered GaAs surface.

to allow remote epitaxy.

The reduced layer-substrate interaction allows the layer peel-off and thus the fabrication of free-standing semiconductor films. It also provides the substrate reuse [5–7, 10–13, 15–18]. In the more delicate way of remote heteroepitaxy, a layer slip on the graphene as an alternative strain-relaxation mechanism rather than the introduction of dislocations was observed [12, 16]. Exceeding the critical strain energy, the layer starts to relax by slipping over the graphene surface instead of forming dislocations [12, 16]. The energy required for a layer slip is significantly smaller compared to the energy to introduce a dislocation. So far, remote epitaxy of several semiconductor material combinations was demonstrated, for example GaAs on GaAs [10, 11], GaN on GaN or on SiC [10, 13, 17], InGaP and GaP on GaAs [12].

In most cases, the growth was performed by MOCVD and a dry transfer method was used to transfer a monolayer graphene to the substrates, rather than the simple wet transfer method. It has been shown, that during wet transfer, the freshly oxide striped GaAs substrate re-oxidises and thus prevents remote epitaxy [18]. However, commercially available CVD transfer

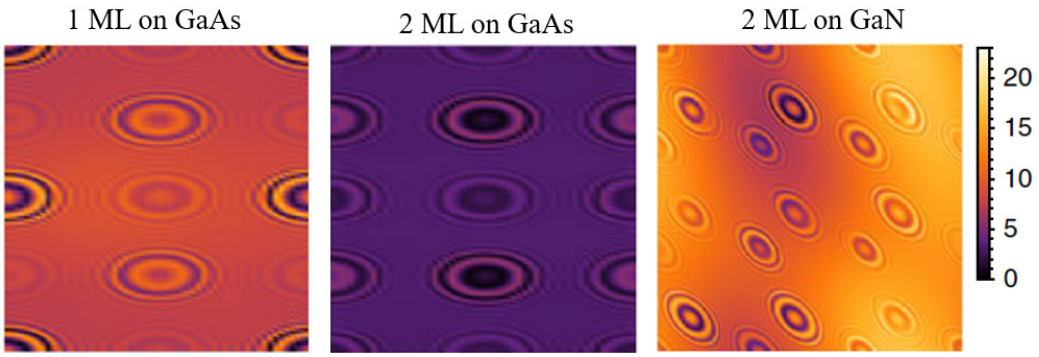

Figure 2.7: DFT simulations of a potential fluctuation (meV) map at the epitaxial surface of monolayer and bilayer graphene covered GaAs and GaN [11].

graphene was tested in [10] and is arguably the easiest way to cover large substrate areas, even entire wafers, with graphene.

2.5 Diffraction phenomena

The reciprocal lattice of a crystal is crucial for the description of diffraction phenomena on periodic crystal structures [20,21,29,40,41]. Popular examples are HRXRD, where X-rays are diffracted by a crystal lattice and RHEED, where electrons are diffracted on the quasi-two-dimensional surface. The reciprocal lattice is the quasi-Fourier transformation of the crystal Bravais lattices. The reciprocal lattice base vectors $\vec{b_i}$ are defined by equation (2.11), where $\vec{a_j}$ represents the corresponding Bravais lattice base vectors [20,40,41].

$$\vec{b_i}\vec{a_j} = 2\pi\delta_{ij} \tag{2.11}$$

The individual reciprocal crystal lattice vectors $\vec{b_i}$ are calculated by equation (2.12) for three dimensions [20, 40, 41].

$$\vec{b_1} = 2\pi\frac{(\vec{a_2}\times\vec{a_3})}{\vec{a_1}(\vec{a_2}\times\vec{a_3})} \qquad \vec{b_2} = 2\pi\frac{(\vec{a_3}\times\vec{a_1})}{\vec{a_1}(\vec{a_2}\times\vec{a_3})} \qquad \vec{b_3} = 2\pi\frac{(\vec{a_1}\times\vec{a_2})}{\vec{a_1}(\vec{a_2}\times\vec{a_3})} \tag{2.12}$$

Considering the fcc lattice of GaAs or InGaAs, the reciprocal lattice is

the body-centred cubic (bcc) lattice. An arbitrary reciprocal lattice vector $\vec{G}$ is calculated by equation (2.13). The indices h, k, l denote the family of planes orthogonal to $\vec{G}$. In real space they indicate the crossing point of the plane with integer multiples of the unit cell vectors. While the notation (hkl) indicates a certain plane, $\{hkl\}$ denotes the set of all equivalent lattice planes [20, 21, 40].

$$\vec{G} = h\vec{b_1} + k\vec{b_2} + l\vec{b_3} \tag{2.13}$$

In the two-dimensional case, a_3 becomes the unit vector $\vec{e_z}$ perpendicular to the surface plane and b_3 is no longer defined. Then, the 2D reciprocal lattice is defined by equation (2.14). A reciprocal lattice of a two-dimensional lattice contains periodically aligned infinite long rods rather than lattice points [40].

$$\vec{b_1} = 2\pi\frac{(\vec{a_2} \times \vec{e_z})}{\vec{a_1}(\vec{a_2} \times \vec{e_z})} \qquad \vec{b_2} = 2\pi\frac{(\vec{e_z} \times \vec{a_1})}{\vec{a_1}(\vec{a_2} \times \vec{e_z})} \tag{2.14}$$

In the following, the diffraction of incident waves on a crystal lattice is derived. Diffraction can be described by an oscillator model, where incident plane waves with wave vector $\vec{k}_{in}$ are scattered by the atom's shell electrons [40, 41]. Considering X-ray diffraction on a crystal, the electromagnetic field wave is scattered and due to the penetration of the X-ray in the crystal, all three dimensions are considered. In contrast, diffraction of an electron wave function in RHEED appears only on the crystal surface, due to the grazing electron incident. A two-dimensional description of the surface is sufficient. In the following, the scattering mechanism of electromagnetic waves on a three-dimensional crystal is considered, but the general findings are also valid for the diffraction of electron beams. Considering an electromagnetic wave with a wave vector $\vec{k}_{in}$ incident on a crystal surface. This incoming wave periodically excites the atom's shell electrons which re-emit an electromagnetic signal with amplitude E_{refl} and wave vector $\vec{k}_{out}$ [40, 41]. In the Born-approximation, this amplitude depends on the electron distribution in the crystal as described in equation (2.15) [41]. The diffraction vector $\vec{q} = \vec{k_{out}} - \vec{k_{in}}$ is defined by the difference of the incoming wave vector $\vec{k}_{in}$ and the diffracted wave vector $\vec{k_{out}}$ [41].

$$E_{refl} \propto \int_V n(\vec{r}) e^{-i(\vec{k}_{in}-\vec{k}_{out})\vec{r}} dV \propto \int_V n(\vec{r}) e^{-i\vec{q}\vec{r}} dV \tag{2.15}$$

In a periodic crystal, the shell electron density is related to the crystal symmetry and thus the periodicity allows a Fourier expansion $n(r) = \sum_G n_G e^{i\vec{G}\vec{r}}$. Inserting this into equation (2.15) and calculating the intensity $I_{refl} = |E_{refl}|^2$ leads to equation (2.16) [41].

$$I_{refl} \propto \sum_{\vec{G}} n_{\vec{G}} \int_V e^{i(\vec{G}-\vec{q})\vec{r}} dV \tag{2.16}$$

The Laue-condition follows from these considerations, as $I_{refl} \neq 0$ only holds for $\vec{G} = \vec{q} = \vec{k_{out}} - \vec{k_{in}}$. All other contributions cancel out for integration over the entire crystal volume. The Laue-condition is valid for scattering on both, quasi-two-dimensional-lattices (for example observed in RHEED) as well as for three-dimensional lattices (for example observed in HRXRD). Only if the scattering vector is equal to the reciprocal lattice vector, the incoming waves interfere constructively along the directions of the scattered wave vector. This is schematically visualised in figure 2.8a). X-rays diffracted on the sample surface exhibit strong reflections, if the Laue-equation is fulfilled. Here, this is shown exemplarily for the (224)-reflex of a fcc crystal. Due to the geometric limitations $2\theta < \omega$ and $\omega < 0°$, the grey filled areas are not accessible in experiments. Basically, the wave vector of the incident wave determines the scattering process. In RHEED only the quasi-2D-surface lattice diffracts the incident beam, so in the reciprocal space, there are reciprocal rods rather than reciprocal lattice points. It yields the same as before, if $\vec{G} = \vec{q}$ the scattering vector hits a rod and intense spots are observed [40,41]. This is exemplarily sketched in figure 2.8b) for the (01)-rod. The spots are elongated as there is some overlap of the Ewald sphere and reciprocal rod due to the finite beam size and non-perfect lattice.

An intuitive way to find the reciprocal lattice reflexes related to experimental conditions is derived from the Laue-equation by introducing $2k \sin\omega = |\vec{k_{out}} - \vec{k_{in}}|$ where ω is the incident wave angle with respect to the sample surface and $|\vec{G}| = \frac{2\pi}{d_{hkl}}$, which is given by the definition of the

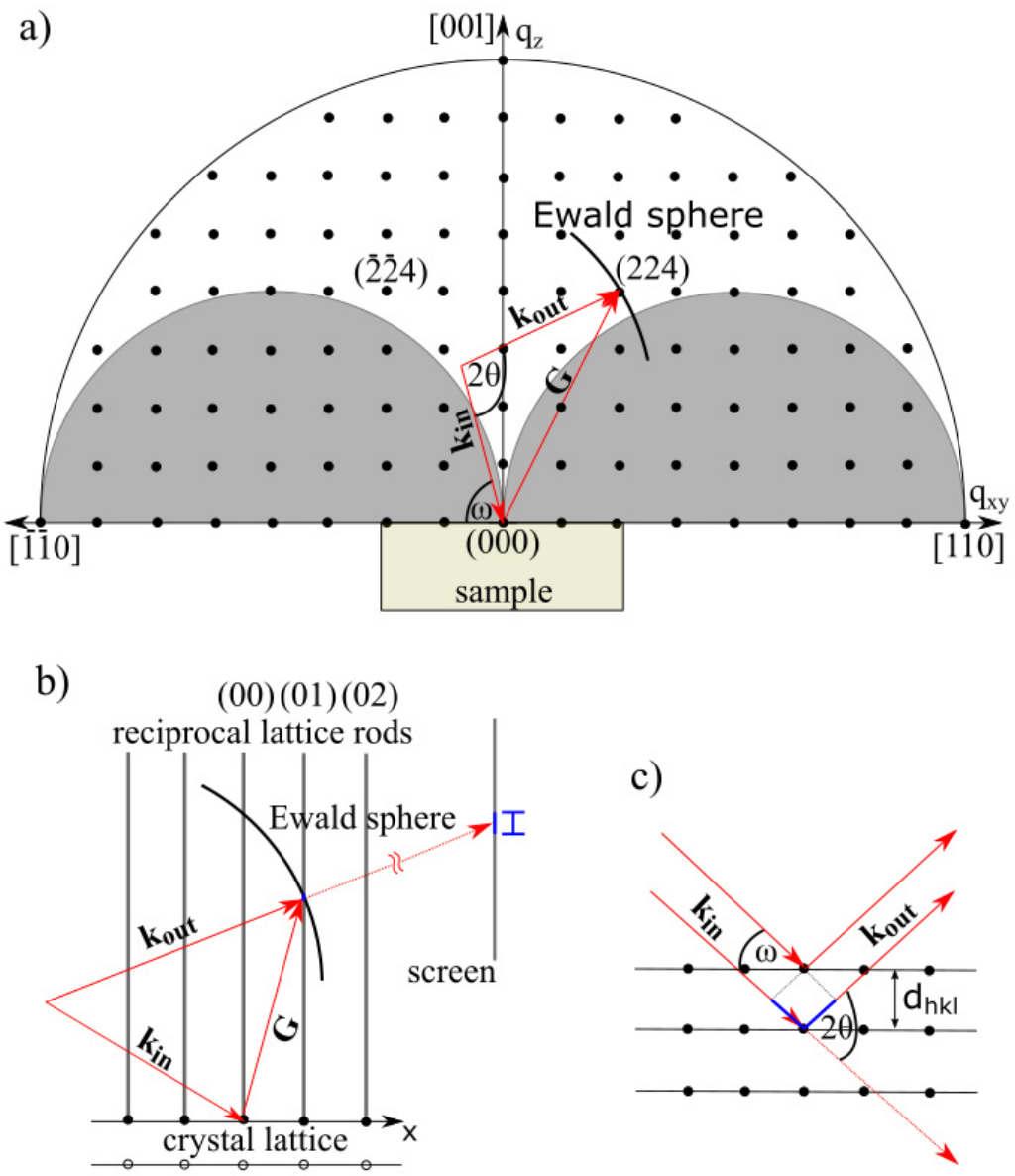

Figure 2.8: a) Schematic sketch of X-ray diffraction on a crystal. If the Laue-condition is fulfilled and the scattering vector equals the reciprocal space vector, decent reflexes are observed [40, 41]. b) Schematic sketch of electron beam diffraction on a crystal surface lattice under shallow beam incidence. Decent spots are observed if the reciprocal lattice vector $\vec{G}$ hits the reciprocal lattice rods. The observed spots exhibit a certain elongation on the screen (blue marker) due to a finite lattice size and slightly varying electron wave vectors [40,41]. c) A visualisation of the Bragg-equation is shown. Constructive interference is observed when path differences $d_{hkl} \sin \omega$ (blue lines) equal integers of $\frac{1}{2}\lambda$.

reciprocal lattice vector in equation (2.13) [20, 21, 41]. Each $\vec{G}$ is normal to a lattice plane of the real lattice which exhibits the Miller indices (hkl) [21]. Note that due to the lattice periodicity $\vec{G} = n\vec{G}_{hkl}$. The Bragg equation (2.17) is derived by combining both considerations from above [42].

$$\begin{aligned} \frac{2\pi n}{d_{hkl}} &= 2k \sin\omega \\ \Leftrightarrow n\lambda &= 2d_{hkl} \sin\omega \end{aligned} \tag{2.17}$$

Constructive interference of diffracted beams is observed for specific incident wave angles ω concerning the sample surface; the path difference $d_{hkl} \sin\omega$ of two X-ray beams must equal integers of $\frac{1}{2}\lambda$ [21, 41, 42]. A schematic sketch is shown in figure 2.8c).

The appearance of certain reflexes was thoroughly described so far. However, to have an impression of the intensity of certain reflexes, equation (2.16) is reconsidered [41]. First, note the quadratic dependence of the scattered intensity on the excited volume. For small samples and thin films, the intensity drops significantly. Further, I_{refl} depends on the electron distribution n_{Gq}; also known as the structure factor F [41]. Its absolute value determines the amplitude of the diffracted wave scattered by all electrons of a unit cell [21, 41]. F is expanded in a Fourier expansion given in equation (2.18) and is a function of the atomic scattering factor f which expresses the scattering intensity of a certain atoms electron distribution [21, 41].The electron distribution is generally stretched around the individual crystal atoms. It also depends on the atom's and electron's position in the unit cell. The structural factor differs for different crystal planes [21]. In a fcc lattice of a zinc blende crystal such as GaAs or $In_xGa_{1-x}As$, there are 2 kinds of atoms, e.g. Ga and As. F is calculated for different planes (hkl) by equation (2.18) with the unit cell vectors in units of the the lattice constant: $(u, v, w) = (0, 0, 0)$ for Ga and $(u, v, w) = (1/4, 1/4, 1/4)$ for As [21].

$$F_{hkl} = \sum_{n=1}^{N} f_n e^{i2\pi(h\vec{u}+k\vec{v}+l\vec{w})} \tag{2.18}$$

The largest value F is obtained for $h + k + l = 4n$ with h,k,l are all even; This is for example the case for the (224) or (004) plane. Reflection on these planes show bright spots. Less intense reflection occurs for example on the (002) plane. Destructive interference ($F = 0$) is observed, if the (hkl) values are mixed even and odd, so for example for the (003) plane. Note that the structure factor can also be derived for the 2D-case similarly. Details are presented in [40]. The RHEED spot intensity along the rods is modulated [40]. However, the used set-up only allows to observe the spots on the first Laue-ring.

In general, there are plenty of additional factors determining the diffracted waves intensity. On the one hand, limits imposed by the beam incident angle play a role, for example in the Lorentz or Debye-Waller factor. Detailed information is provided in [41]. On the other hand, in real crystals, the perfect crystal structure is perturbed by strain fields or defects resulting in lower reflected peak intensities and reflex peak broadening by slightly distorted, tilted or twisted diffraction planes. This makes diffracted waves suitable for analysing crystal properties [20, 21, 40].

Chapter 3

Experimental set-up

In the following chapter, the experimental set-up and the measurement techniques used to grow and analyse $In_xGa_{1-x}As$ films on graphene covered GaAs substrates are described. Firstly, the MBE system and the growth process is explained. Then, the RIE set-up used to clean the graphene layer from polymer residuals is described. In the second part, the devices used to analysed the grown $In_xGa_{1-x}As$ films are presented. The surface quality of thin $In_xGa_{1-x}As$ films is investigated by AFM and SEM, to understand the nucleation behaviour and to find proper epitaxial growth conditions of thicker films. The intensively used HRXRD set-up is presented as a powerful tool, to provide information on the $In_xGa_{1-x}As$ film crystal structure. Lastly, TEM, XPS and Raman-spectroscopy are briefly explained. These three measurement techniques were performed by collaboration partners. XPS reveals the surface quality of the graphene layer and the GaAs substrate surface after graphene transfer and cleaning. TEM measurements provide crystal structure information on an atomic scale. The graphene quality and the $In_xGa_{1-x}As$ crystal structure were analysed by means of Raman-spectroscopy.

3.1 Molecular beam epitaxy

In this work, $In_xGa_{1-x}As$ heteroepitaxial growth on graphene covered GaAs substrates was performed by an MBE apparatus. MBE has continuously

played a pivotal role in the research of modern semiconductor devices since the beginning of MBE-GaAs growth in the late 1960s and later the fabrication of the first semiconductor quantum-well reported by Arthur [43], LePore [44] and Cho [45] at the Bell Laboratories [19, 46]. Operated in UHV conditions, MBE provides precise control of layer thickness, composition and dopant incorporation up to the atomic scale. It enables high-quality structure fabrication with a low parasitic molecule concentration due to the ultra high vacuum conditions. These abilities allow the preparation of tailored novel heterostructures with sharp interfaces [19, 46, 47].

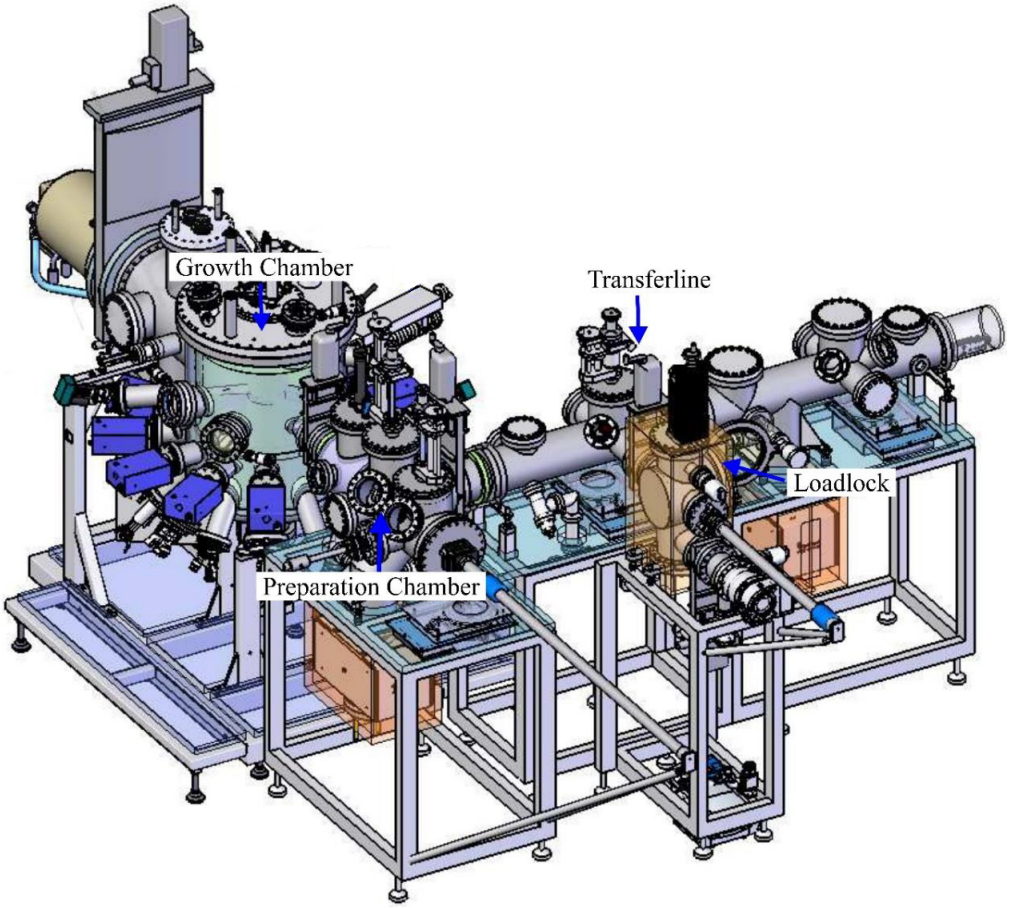

Figure 3.1: Schematic sketch of the operated MBE system from *Dr. Eberl MBE-Komponenten GmbH* [48].

The film growth is performed in a MBE chamber from *Dr. Eberl MBE-*

Komponenten GmbH, enrolled to perform III-As and III-Sb semiconductor growth. A sketch is shown in figure 3.1 [48]. The entire set-up is divided into four individual chambers. In the load lock, wafers mounted on molybdenum platen are introduced into the MBE-system and taken out after growth. A turbo molecular pump achieves a vacuum of $< 1 \times 10^{-7}$ mbar within a few hours. When loading samples, the platens are exposed to air, so moisture, carbon, oxygen, etc. are trapped on the platen, the porous unintentionally deposited III-As layer on the platen and on the wafer surface. To preserve the vacuum integrity of the other chambers, the platen and the wafer are baked for 8 h at 120°C, prior to further transfer, to evaporate the contaminants. The second chamber, the transfer line, is used to transfer the wafers from the load lock to the preparation chamber, where they are stored in an 8-way magazine. The preparation chamber is equipped with a heating station and an atomic hydrogen source. Each wafer is placed on the heating station and baked again for 1 h at 200°C to degas any contaminants trapped on the wafer or platen prior to transfer into the growth chamber. Atomic hydrogen cleaning was not utilised. For a detailed description refer to [47]. The transfer, preparation and growth chamber are all individually pumped by a ion-getter pump armed with titanium supplementation filaments (TSP-IGP) to a background pressure of $< 10^{-10}$ mbar. In addition, the growth chamber is pumped by a closed-cycle cryopump and cooling shrouds filled with liquid nitrogen during MBE operation, to reduce the desorption of parasitic atoms from the chamber walls. A schematic sketch of a III-V growth chamber during operation is depicted in figure 3.2.

The wafer is mounted on a rotating and heated substrate manipulator, usually operated at 10 rpm to ensure homogeneous material deposition all over the wafer. The sample backside is heated radiatively by a tantalum heating filament located behind a pyrolytic boron nitride diffuser plate for optimised temperature homogeneity. The substrate temperature during growth is a critical parameter and must be controlled precisely due to the exponential temperature influence on the growth kinetics, as described in chapter 2. The temperature is measured by a type-C thermocouple mounted located behind the manipulator heater and in parallel by a kSA-BandiT system measuring

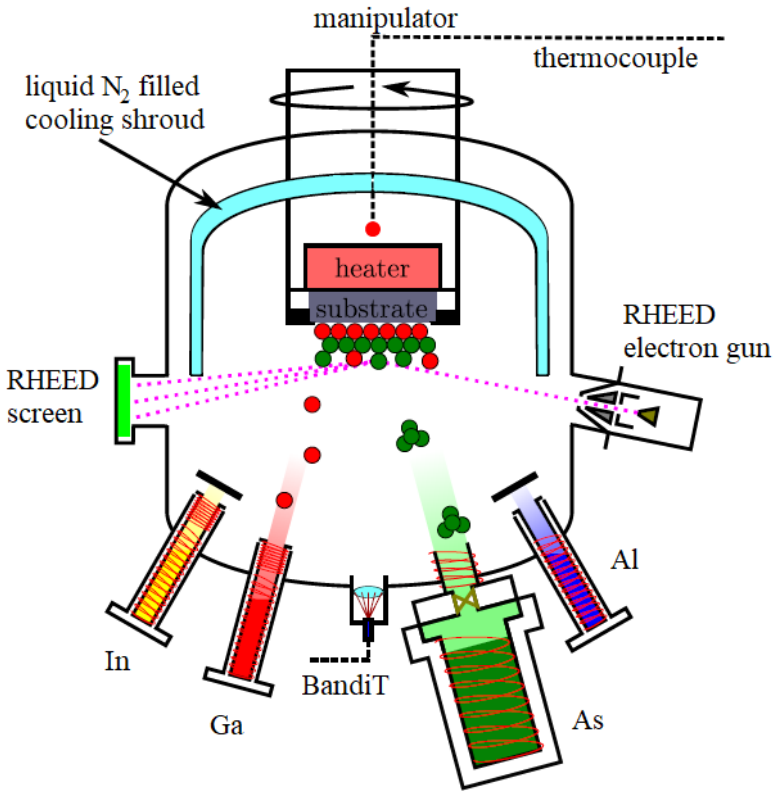

Figure 3.2: Schematic sketch of the III-As MBE growth chamber. [49].

the samples temperature depending optical absorption edge shift (the band gap-temperature dependence related to the Varshni-equation (2.5) is analysed) [50]. Because the thermocouple is located behind the heater, there is always an offset in the measured temperature and the real sample temperature, e.g. the thermocouple temperature shifts for different platen and different mounted 1/4 3" wafer flats. In contrast, the BandiT system calculates the temperature directly from the wafer's optical absorption, so the influence of the platen and the wafer form or size is cancelled out. The detected spectrum is fitted to the band edge absorption by the BandiT-system. The kSA-generated calibration files are used to determine the temperature [50]. All temperatures in the following were measured by the Bandit system; the uncertainty is $\pm 2°C$.

There are several effusion cells filled with high purity materials ($> 5N$), each may be individually heated and used. A total of seven different materials

(Al, As, C, Ga, In, Si, Sb) are available in the present MBE system. However, all following structures only utilises gallium (Ga), indium (In) and arsenic (As). While gallium and indium are evaporated from effusion cells, arsenic is evaporated from a valved cracker source with a motorised valve control unit. This allows a fast switch in the arsenic-flux, without a need to change the cell's temperature. At low cracker temperature of around 450°C, As_4 is evaporated. This configuration is used for the entire growth discussed in the following. The molecular beams evaporated from the cells can be blocked either by individual cell shutters or by the substrate shutter. This allows precise monolayer film deposition. Prior to growth, the molecular beam fluxes arriving at the sample are measured by a Bayard-Alpert type ionization-gauge, also known as beam-flux-monitor. It can be moved directly underneath the substrate manipulator. The measured ion-current is translated to a beam-equivalent-pressure (BEP), so the III-V ratio can be calculated [48]. In this work, $In_xGa_{1-x}As$ growth is performed in As_4 overpressure within the commonly used III-V ratio range between 10 and 100; Detailed ratios used in this work are presented in chapter 5. III-As growth is self-regulated above ≈ 300°C as long as there is excess As, because the As sticking coefficient is zero above 300°C when no metal atoms are present [19, 21].

3.1.1 Reflection high-energy electron diffraction

A very important tool in MBE systems is RHEED. It is employed to monitor the growth process in-situ and delivers information on the surface crystallography and surface kinetics [21, 29, 51]. Here a Staib-RHEED set-up is used, operated at 10 kV and 1.5 A. The electron gun and the phosphorescence RHEED-screen is mounted at a shallow angle with respect to the substrate manipulator, as shown in figure 3.2. The generated and finely collimated electron beam is directed towards the substrate surface at a grazing angle of around $1° - 3°$. The penetration depth of the electrons is only a few angstroms, due to the shallow angle, making this method extremely surface sensitive [21,29,51]. The scattered electron diffraction pattern reveals the crystals surface reconstruction if the electron beam is in alignment with the low miller

indices crystal directions. On the surface, dangling bonds re-arrange to minimise their energy [21,29,46,51]. Figure 3.3 shows different RHEED patterns and the corresponding surface structures; for example, spots on the Laue-ring confirm a smooth single crystalline surface. The surface reconstruction changes with temperature. Various reconstructions of GaAs can be found in [52]. The GaAs surface reconstruction changes from c(4x4) to (2×4) for example, when the sample is heated above the thermal de-oxidation temperature of around 590°C in arsenic-rich conditions [53,54]. Relaxed $In_xGa_{1-x}As$ exhibits the (2x4) or (4x2) reconstruction, while for strained $In_xGa_{1-x}As$ films on GaAs the (4x3) reconstruction is observed [24, 55]. However, due to the lattice mismatch of 0% to 7% in the $In_xGa_{1-x}As$/GaAs system, the surface may becomes too rough to observe any surface reconstruction during growth.

Another useful RHEED-feature is monitoring the change in spot intensity during growth, to determine the growth rate. A closed smooth layer exhibits a higher intensity compared to a partially closed one. During layer-by-layer growth, material is deposited on the sample. This causes the formation of nuclei on the flat surface. The detected RHEED-intensity on this rougher surface drops. When growth is continuous, the layer coalescences again and the RHEED-intensity increases. Layer-by-layer growth results in an oscillating RHEED-intensity. One period corresponds to a monolayer. Thus the time interval between two maxima give the growth rate [51]. Here, the growth rates of GaAs on GaAs substrates and of InAs on InAs substrates were measured. The measurement uncertainty is approximately ±5%. However, to determine the indium to gallium ratio in the grown layer, the preciser HRXRD measurements were performed.

3.1.2 Growth preparation

Usually a growth run is divided into several steps. In the following section, the basic growth procedure is discussed. The growth parameters like temperature, arsenic pressure, nucleation layer thickness etc. were tuned and optimised to obtain smooth and defect-free $In_xGa_{1-x}As$ films. This is

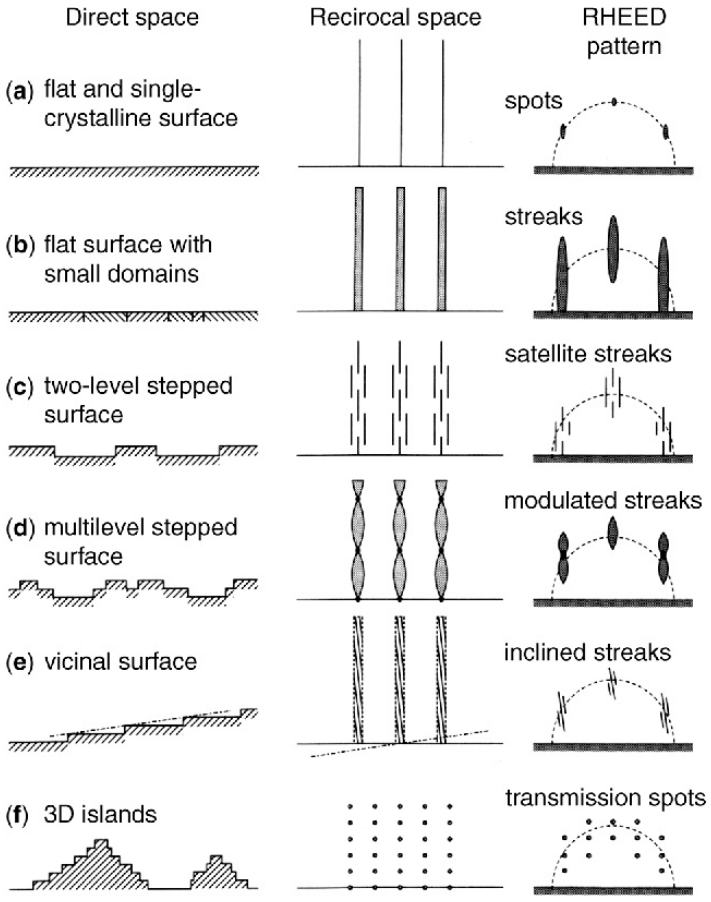

Figure 3.3: Different RHEED-pattern and the corresponding surfaces in real and reciprocal space [51]. A flat and single crystalline surface exhibits spot on the Laue-ring.

explained in more detail in chapter 5.

- First, a full 3" semi-insulating GaAs(001) wafer from *Wafer Technology Ltd.* is cleaved into 4 quarters.

- The surface oxide is removed by dipping the quarter wafer 1 min in 10% HCl, followed by DI-water rinse and immediate monolayer graphene transfer. Details on the graphene transfer are discussed in the next chapter 4.

- The 1/4 wafer is mounted on a molybdenum plate and loaded into the load lock. The load lock is baked for 8 h at 120°C.

- Platen and wafer are transferred onto the heating station in the preparation chamber and degassed again at 200°C until the chamber pressure drops below 5×10^{-9} mbar, but for at least 1 h.

- The sample is introduced into the main growth chamber, i.e. onto the sample manipulator. Its temperature is approximately 300°C.

- The temperature is increased in arsenic overpressure. The start of the sample de-oxidation is observed at approximately 590°C by an increase in the RHEED-spot intensity [47]. The sample temperature is increased to roughly 620° C and the sample is annealed for 5 min. The two main reasons for this step are: Residuals on the graphene are evaporated at high temperature and the bare GaAs wafer is de-oxidised and annealed. In this way, $In_xGa_{1-x}As$ films can be grown on a monolayer graphene and on the bare GaAs in parallel.

- The temperature is decreased to roughly 425°C, before the arsenic valve and shutter are closed. The temperature is low enough to keep the GaAs surface stable, but high enough to allow arsenic re-evaporation from the graphene surface.

- The temperature is ramped to the $In_xGa_{1-x}As$ "nucleation temperature", which usually is 300°C. After waiting a few minutes for temperature stabilisation, the indium shutter, the gallium shutter and the arsenic shutter and valve are opened simultaneously. The arsenic beam flux increases slower compared to the gallium and indium flux. There is a time delay, because the indium valve opens slower compared to the shutters of the gallium and indium cell. Due to this time delay, the remote epitaxial growth of small nuclei on the graphene covered GaAs is initialised by gallium and indium atoms. This is reported to be

indispensable due to the stronger binding of an arsenic-graphene-metal stack compared to an arsenic-graphene-arsenic stack [10].

- The metal shutters are closed and the substrate temperature is ramped to the selected overgrowth temperature in As_4 overpressure to keep the nucleation layer surface stable.

- Thicker $In_xGa_{1-x}As$ films are grown. The chosen As_4 flux depends on the indium fraction and substrate temperature. Details are provided in chapter 5. The film thickness uncertainty is $\pm 10\%$ and the As_4 flux uncertainty is $\pm 0.1 \times 10^{-5}$ mbar for all samples grown in this dissertation

- Finally, the substrate temperature is decreased to 300°C in As_4 overpressure and the sample is removed from the MBE.

3.2 Reactive Ion Etching

In semiconductor fabrication, RIE is a typical method to dry etch substrates or films to create tailored nano-structures and devices. The basic principle is the reaction of a sample with reactive ions and radicals generated in a plasma by high frequency electromagnetic fields [56–58]. In this thesis, an advanced dry etching method based on inductively coupled plasma (ICP) is used to clean Poly(methyl methacrylate) (PMMA) residuals from monolayer graphene surfaces [56,58,59]. A schematic set-up of a PlasmaLab 100 reaction chamber from *Oxford Instruments plc* used for ICP-RIE in this work is shown in figure 3.4. The sample is mounted on a host silicon wafer lying on a table. The chamber is pumped continuously to a background pressure of $< 5 \times 10^{-7}$ mbar to minimise the residual gas, to enable the plasma ignition and to remove the reaction products during an etching process. A gas inlet provides the reaction gases. A coil is mounted around the chamber. Both, the sample table and the coil may be biased individually by a radio frequency

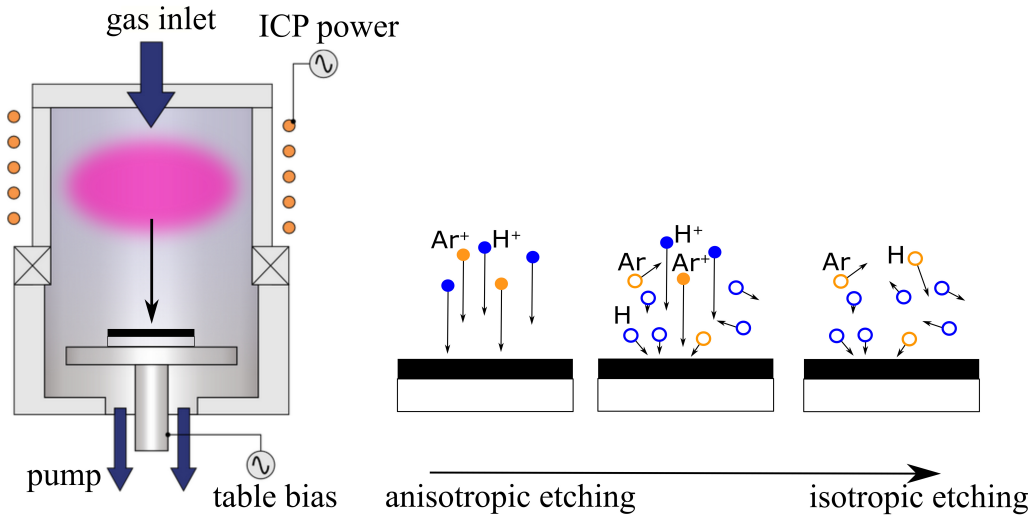

Figure 3.4: Schematic sketch of the used ICP-RIE machine [59] and visualisation of different etching techniques. The plasma is generated above the sample. The table bias is tunable and governs the etching type. A low applied bias causes mainly isotropic etching and a higher bias anisotropic etching, respectively.

(RF)-signal. Applied to the coil, the RF-signal creates an electromagnetic field in the chamber and accelerates the molecule's electrons from side to side during every oscillation period, while the heavier ions cannot follow the field. Above a certain threshold power, the electrons are ripped off the molecules and the plasma ignites spontaneously [57, 58, 60]. Note, in this set-up, the plasma is generated above the sample [59]. Mainly, thermal radicals escape the plasma and reach the sample surface, where they interact by isotropic chemical reaction with the sample surface. The radicals energy is too low to sputter the sample [56, 59].

A RF-signal applied to the sample platen may also generate a plasma. However, some accelerated electrons collide with the platen and charge it, so a potential between the slightly positively charged plasma and the slightly negatively charged platen builds up. The positive ions are accelerated toward the platen and collide with the sample. Apart from the chemical reaction of ions and sample, the ions also sputter the sample, as they exhibit a sufficient energy and momentum. This process is quite anisotropic. With this process,

sharp etch profiles may be achieved [57, 58]. A wide process window is found by managing the power applied to the coil and the platen, ranging from mainly isotropic and mild etching conditions to anisotropic/directional etching. This is schematically shown in figure 3.4. The coil is biased to create the plasma, while the platen is biased to control the ion energy [57–59]. The etching process may be tuned and tailored by several process parameters: the gas pressure and flux, the applied RF powers, the etching time, the sample temperature, the background pressure and of course the chamber itself. Tailoring the process parameters to clean graphene surfaces from polymer residuals is described in the next chapter 4 in more detail.

3.3 Atomic force microscopy

AFM is a technique to determine a sample's surface in detail. Deviation in a sample surface height are measured with sub-nanometre precision. AFM images reveal a sample's surface morphology and the surface roughness. Therefore, AFM is often conducted after graphene cleaning or after $In_xGa_{1-x}As$ film growth.

Here, a *Nanosurf Mobile S* atomic force microscope with *ppp-xycontr*-cantilevers from *NanoAndMore GmbH* is used. A sketch is presented in figure 3.5 [61]. A sharp tip with a diameter of roughly ≤ 7 nm on a cantilever interacts with the sample surface through a raster scanning motion [61, 62]. The up and down and side to side motion applied by piezo crystals is monitored by a laser beam reflected from the backside of the aluminium coated cantilever, as the tip scans along the surface. This reflected laser beam is traced by a position-sensitive photo-detector, that picks up the vertical and lateral motion of the tip [61, 62]. Measurements were performed in the so-called static or contact mode. The cantilever raster scans the surface, while the tip is in continuous close contact to the sample surface, where it is repulsed due to the Lennard-Jones-potential. The static mode is operated with constant force; the force applied to the tip/cantilever is kept constant at 18 nN during the scanning process. The output raw data consists of the height (z topography) and its deflection for each surface in-plane coordin-

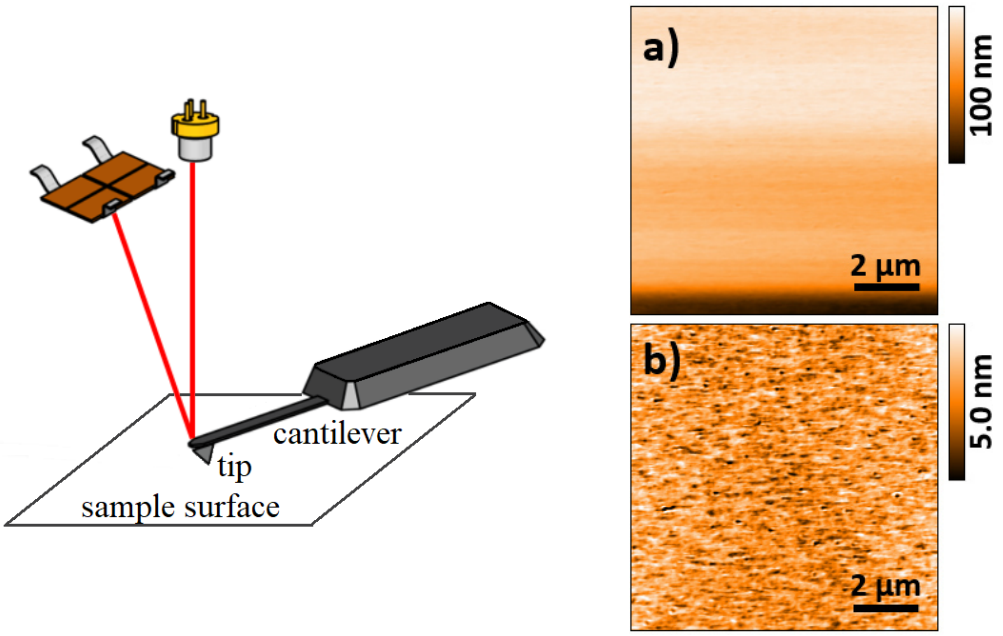

Figure 3.5: Schematic sketch of the AFM set-up. The laser diode beam is reflected by the tip's backside and detected during raster-scanning the sample surface [61]. a) shows an AFM image of the raw-data and b) shows the drift corrected AFM image.

ate. The measurement planar resolution is 256×256 pixels for image sizes between 1×1 μm^2 and 10×10 μm^2.

A typical raw data topography image exhibiting a considerable drift in the z-direction is shown in figure 3.5a). This drift makes it hard to analyses the sample surface. However, the Nanosurf software offers different kinds of fitting algorithms for data correction. Here, the *line fit* algorithm is used, which calculates the mean height and slope value for every line and subtracts it from the raw data. The so corrected image is exemplarily shown in figure 3.5b) [61].

A quantity to compare sample surfaces is the root-mean-square (RMS) roughness σ, which is calculated by equation (3.1); $z_i - \bar{z}$ is the height difference of each pixel i from the calculated mean height z and n is the total pixel number. The RMS roughness uncertainty is ± 0.1 nm.

$$\sigma = \sqrt{\frac{1}{n}\sum_{i}^{n}(z_i - \bar{z})^2} \tag{3.1}$$

3.4 High-resolution X-ray diffraction

While AFM is used to analyse the sample surface, HRXRD is a powerful non-invasive method commonly used to analyse the crystallographic structure of an epitaxial layer [21, 41]. Here, a *Malvern Panalytical X'Pert MRD* triple-axis diffractometer is used to perform HRXRD measurements. A schematic sketch is presented in figure 3.6. A copper cathode operated at 45 kV and 40 mA generates an X-ray beam. The beam is parallelized by a parabolic mirror and monochromised by (220)-channel-cut germanium crystals. X-rays with a wavelength of $\lambda = 1.54056$ Å ($Cu_{K\alpha 1}$ line) pass through the monochromator, while the broad Bremsstrahlung background and other emission lines, e.g. the $Cu_{K\alpha 2}$ line, are filtered [63]. The filtered X-ray beam size is defined by an incident slit, before the beam hits the sample at an angle ω. The diffracted beam is then detected at an angle 2θ by an *Analytical X'Celerator* detector [63]. The angular resolution of the reflected beam is tuned by a programmable receiving slit. Note, the inevitable trade-off between resolution and intensity; a narrow incident or receiving slit only lets X-rays with a

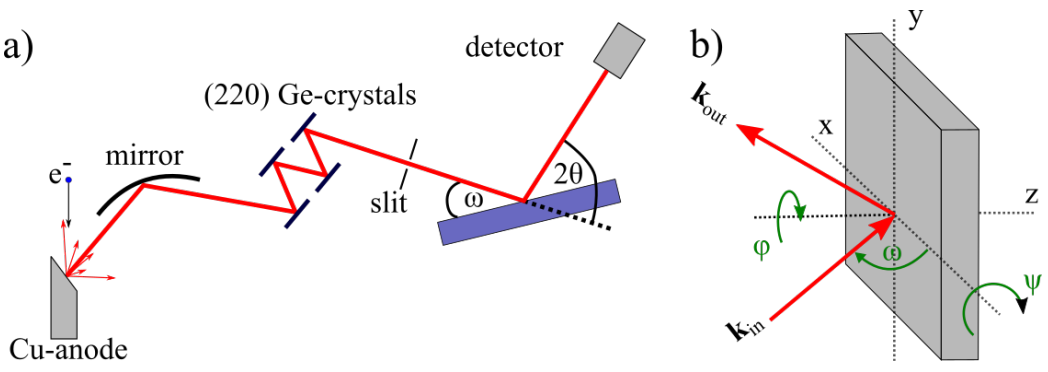

Figure 3.6: a) Schematic sketch of the high-resolution X-ray diffractometer. b) Sketch of a mounted sample and the corresponding symmetry axes. The samples can be moved in x-, y-, z-direction and rotated by ϕ,ψ, ω.

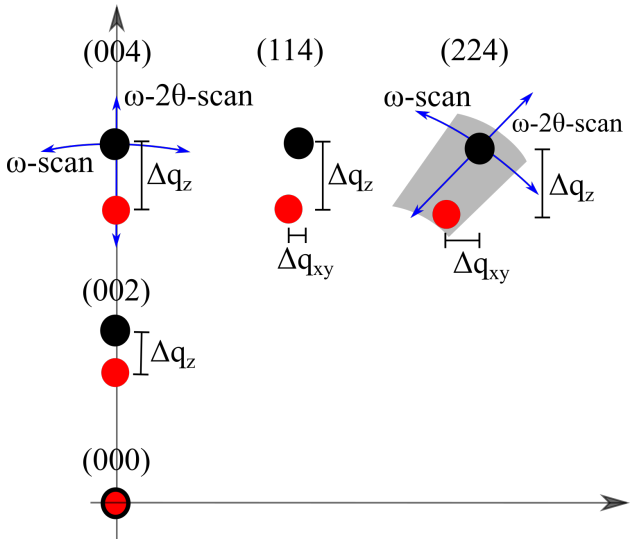

Figure 3.7: RSM showing the important (004)- and (224)-reciprocal-lattice reflex of an $In_xGa_{1-x}As$ layer (red dots) grown on a GaAs substrate (black dots). The scan direction of ω-scans and ω-2θ-scans are depicted. A map around the (224-reciprocal lattice reflex is indicated by the grey area. Higher indexed reflexes exhibit a large separation $\Delta_{q_{xy}}$ an Δ_{q_z} between layer and substrate peak.

small angle distribution pass, so a high angular resolution is achieved, resulting in a rather low intensity, as most of the beam is blocked, leading to a low signal-to-noise ratio [63]. A sample is mounted on a sample holder, which is fixed at an Euler-cradle allowing motion and rotation on 6 axes independently. The sample may be moved in x-,y-,z-direction and rotated by ψ, ϕ and ω. See figure 3.6 for a schematic sketch.

The analysed samples analysed in this work have a size of $\approx 5 \times 5$ mm. To avoid a parasitic scattered signal from the cradle and sample holder, the samples are fixed on a silicon wafer with double-sided tape before mounting them onto the Euler-cradle. Mounting a sample always applies a twist and tilt of the sample with respect to the incident plane, thus reducing the detected intensity. Therefore, prior to every measurement, the sample position is calibrated by individually measuring each parameter. The best value is obtained for the maximum GaAs substrate intensities reached within a scan. This value is used as the new calibrated value. Of course, changing one

parameter will affect the other ones, so an iterative optimisation procedure is carried out. Once calibrated, the measurement is started.

As already described in chapter 2, perfect crystals exhibit intense reflection for incident X-rays fulfilling the Bragg-equation. However, in real crystals, deviation from the perfect conditions appears and this deviation is observed in HRXRD measurements. Commonly used scans are the ω-2θ-scan and the ω-scan visualised in the reciprocal space map given in figure 3.7. Black and red dots represent the reciprocal lattice points of GaAs and $In_xGa_{1-x}As$, respectively.

In an ω-2θ-scan, both ω and θ are moved simultaneously. In this mode, $\omega = 2\theta$. These measurements are performed for symmetric reflexes, because then, only the q_z coordinate is probed, while $q_{xy} = 0$. This scan probes the single crystalline phase of a film as the appearance of non-(00l)-peaks in the measured spectrum would indicate structural disorder and polymorphism [41]. In an ω-scan, also called rocking curve, only ω is moved. As depicted in figure 3.7, an ω-scan entails a variation of the scattering vector on a circular path in the reciprocal space [41]. Regarding the Bragg-equation, a perfect crystal exhibits reflections only for a certain angle. However, real crystals may consists of slightly tilted or twisted mosaic blocks or contain dislocations and thus exhibit reflection of a broader angle range. For fcc-lattice crystals, the full width at half maximum (FWHM) of an ω-scan of the (004)-reciprocal lattice reflex is related to a layer's dislocation density n_{dis} by equation (3.2); $b \approx 4$Å is the dislocations burger vector [64].

$$n_{dis} = \frac{FWHM^2}{9b^2} \tag{3.2}$$

A powerful method to investigate layers, is to map the area around certain reciprocal lattice reflexes. This is done by performing several ω-scans for certain values of 2θ around a reflex as schematically depicted by the grey area in figure 3.7. Figure 3.8 shows a typical ω-2θ map measured of an $In_{0.15}Ga_{0.85}As$ layer grown on GaAs. To analyse the data, this map is converted into the reciprocal space by equation (3.3) and (3.4). Plus and minus represent positive

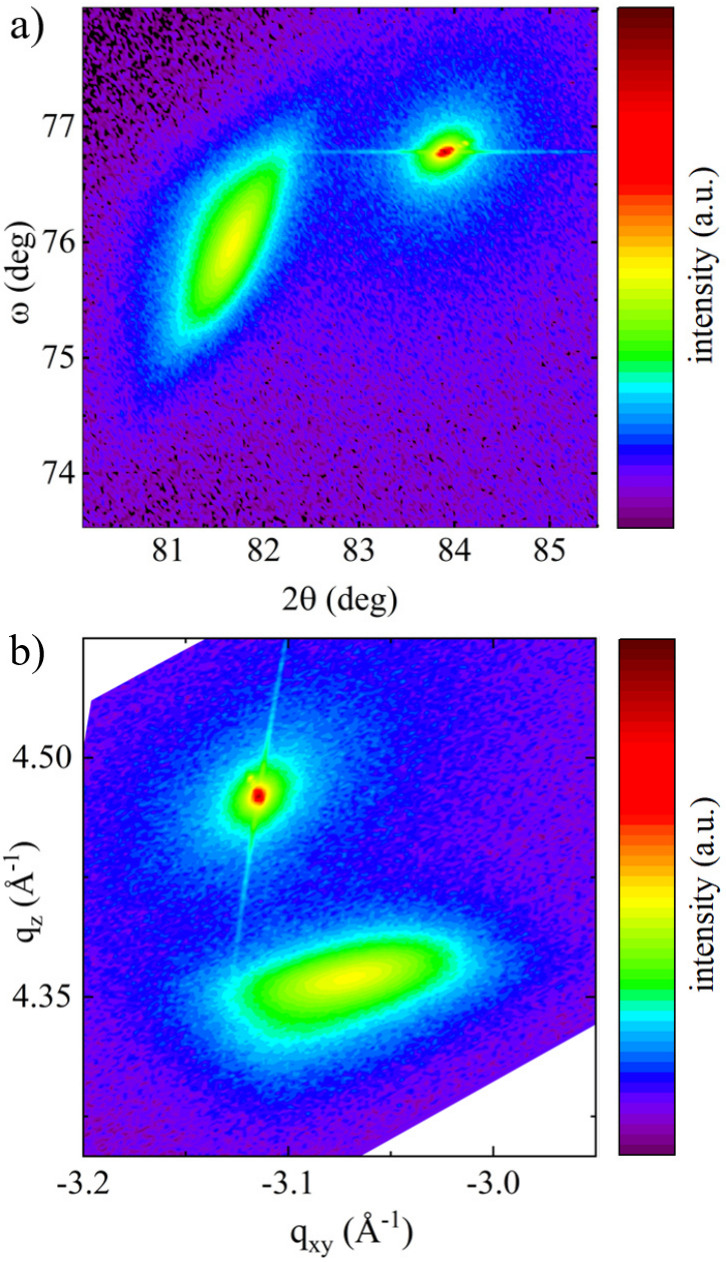

Figure 3.8: a) A typical ω-2θ map of the (-2-24)-reciprocal lattice reflex of an $In_{0.30}Ga_{0.70}As$ film grown on a GaAs substrate and b) the corresponding RSM calculated by equation (3.3) and (3.3).

values (hkl) and negative values (-h-kl), respectively. The in-plane reciprocal coordinate q_{xy} lies in the plane parallel to the sample surface, while q_z is orthogonal to the sample surface.

$$q_{xy} = \pm\frac{2\pi}{\lambda}(\cos(2\theta - \omega) - \cos(\omega)) \tag{3.3}$$

$$q_z = \frac{2\pi}{\lambda}(\sin(2\theta - \omega) - \sin(\omega)) \tag{3.4}$$

The GaAs substrate reciprocal lattice reflex is clearly observed. It exhibits the strongest intensity. However, its coordinates differ from the theoretically calculated ones, as only the relative angles within a measurement are precise but not the absolute angles [63]. The theoretical reciprocal lattice coordinates of the GaAs substrate and of pseudomorphic and relaxed InAs are calculated by equations (3.5) and (3.6).

$$q_{xy} = \frac{2\pi}{a}\sqrt{h^2 + k^2} \tag{3.5}$$

$$q_z = \frac{2\pi}{a}\sqrt{l^2} \tag{3.6}$$

The values are plotted in figure 3.9 as grey squares. They are used to figure out the layer's strain and indium composition. All values are then shifted by the vector $\Delta\vec{q} = \vec{q}_{theo} - \vec{q}_{exp}$, calculated by the reciprocal lattice difference of the measured GaAs substrate peak $\vec{q}_{exp}$ and the theoretically calculated one $\vec{q}_{theo}$. An example is shown in figure 3.9. The red arrow visualises $\Delta\vec{q}$.

An $In_xGa_{1-x}As$ film grown on GaAs exhibits a peak somewhere in this triangle and the relative distance to the GaAs peak and the strained and relaxed InAs peaks is used to calculate the degree of relaxation and the indium concentration. Therefore, equation (3.7) and (3.8) are used. The values a_1, a_2, b_1 and b_2 are shown in figure 3.9. The measurement error of the relaxation degree and the indium concentration is approximately $\pm 2\%$ and $\pm 1.5\%$ for all samples analysed in the following, respectively.

$$\text{indium concentration} = \frac{a_1}{a_2 + a_1} \tag{3.7}$$

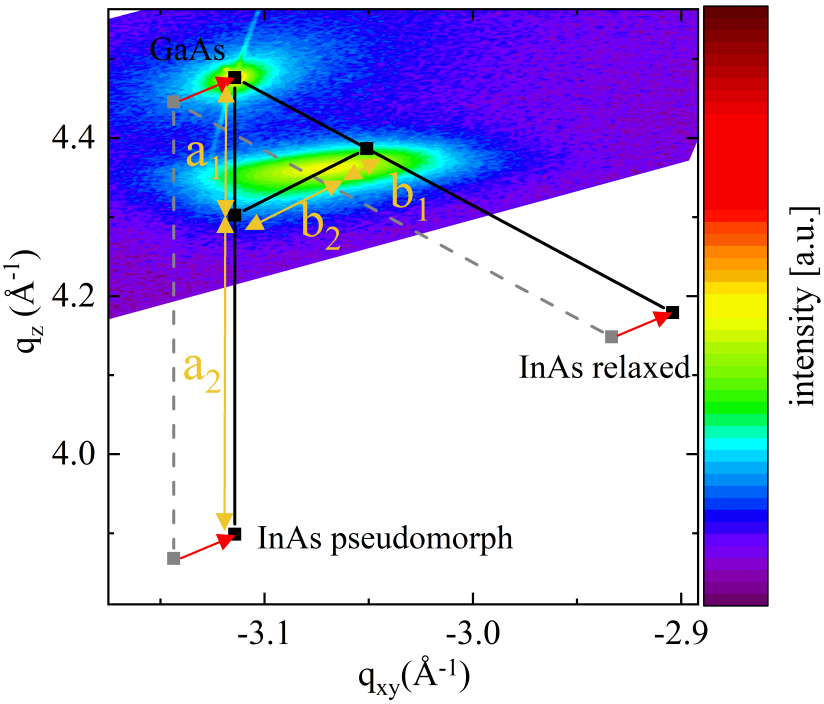

Figure 3.9: RSM of an $In_{0.30}Ga_{0.70}As$ film on a GaAs substrate. The offset correction between measured and calculated reciprocal lattice points is indicated by the red arrows. The indium concentration and the film relaxation degree are derived from the proportion of a_1, a_2 and of b_1 and b_2, respectively.

$$\text{relaxation degree} = \frac{b_2}{b_2 + b_1} \tag{3.8}$$

To obtain precise values, a reflex with a high resolution in q_{xy} and q_z, but also with a high reflected intensity should be chosen. Typically the (004)- and the (224)- or (-2-24)-reciprocal lattice reflexes are used for symmetric and asymmetric measurements within the $In_xGa_{1-x}As$/GaAs system, respectively. On one hand, these reflexes exhibit a large fine structure constant and thus reflection on these lattice planes results in bright spots, on the other hand, the resolution (Δ_{q_z} and $\Delta_{q_{xy}}$) of the (224)- and (-2-24)-reciprocal lattice reflex is high. Figure 3.7 shows this. The best trade-off in resolution and intensity is observed for the (-2-24)- and (224)-reciprocal lattice reflex [41,63]. Another factor is the measurement geometry. While the (224)-reciprocal lattice reflex is analysed under a shallow beam incident, the so-called grazing

incident geometry, the (-2-24)-reciprocal lattice reflex is analysed under a shallow diffracted beam, so-called grazing exit geometry. A higher intensity is detected in the first configuration, as the beam penetrates a rather large crystal volume, but the lateral resolution is smaller. In the latter configuration, the beam hits the sample under nearly 90°, hence the diffracted beam contains signal from a significant smaller sample volume. The resolution is better. The indium concentration and the degree of film relaxation is determined more accurate. However, the diffracted beam intensity and therefore the signal-to-noise ratio is smaller. The (-2-24)-reciprocal lattice reflex was measured for 200 nm thick $In_xGa_{1-x}As$ films. Thinner $In_xGa_{1-x}As$ films were measured in the (224) geometry.

3.5 Scanning electron microscopy

In this section, SEM is described. This technique is based on the electron deflection on a sample surface [65]. The used system here is a *RAITH150-TWO* from *RAITH GmbH* able to perform both, electron beam lithography and scanning electron microscopy. Here SEM is used as a competitive method to AFM. All measurements were performed with the help of Dennis Deutsch. Wet transferred graphene on GaAs and $In_xGa_{1-x}As$ nuclei on graphene covered GaAs were imaged. The resolution was up to 100k.

When operating in the imaging mode, an electron beam is generated by an electron gun and shaped by electromagnetic lenses [65, 66]. For enhanced resolution, an accelerator voltage of 15 kV was used. The focused beam hits the sample surface, where the electrons interact with the sample. Backscattered electrons, secondary electrons and X-ray photons are re-emitted. The backscattered electrons origin lies deeper within the sample. They are emitted by elastic scattering of the impinging electrons, thus giving material information up to a certain thickness. The secondary electrons are ejected from the samples conduction or valence band by inelastic electron-sample-scattering interactions [65]. Due to their low energy, these electrons originate within a few nanometres below the sample surface and reveal topological information only from the topmost layers [65, 66]. The latter method is mainly

used in this thesis. Secondary electrons are detected by an in-lens detector, that images lateral differences in the material work function [66]. The actual resolution observed in the images not only depends on the SEM-system, but also on the operator and their ability to focus the electron beam precisely. Here, a lateral resolution of roughly 10 nm was achieved. The in-lens detector enables the distinction amongst different materials, like GaAs and $In_xGa_{1-x}As$. It can be distinguished amongst multi- and monolayer graphene.

3.6 TEM, XPS, Raman

In this last section, the characterisation methods performed by the collaboration partners are briefly presented.

Raman-spectroscopy was performed by AG Goldhahn of the Otto-von-Guericke University in Magdeburg. It relies upon inelastic photon scattering in a material. Detailed overviews may be found in [67–69]. Raman-spectra were recorded by using a TriVista777 (S&I GmbH) equipped with a 532 nm laser source within a Raman microscope. The laser beam was focused on the sample by a microscope objective where the photons interact with the crystal [70, 71]. The resolution is 0.2 cm^{-1}. Apart from the typical elastic Rayleigh-scattering, inelastic scattering of photons with low energy excitations in the crystal occurs as well, for example, defect or vibrational states. The re-emitted photon energy is slightly shifted. A shift to lower photon energies occurs if the photon transfers energy by creating a vibration or phonon in the crystal (Stokes scattering), whereas a shift to higher energies occurs if a vibration or phonon in an excited state (called Anti-Stokes scattering) is relaxed and energy is transferred to the photon [67–69]. These energy-shifts are rather small and weak in comparison to the intense laser beam, so the laser light is filtered, before the spectrum is resolved by a spectrometer and detected [70, 71]. In the used set-up, the resolution is ± 0.2 cm^{-1} [70, 71]. The Raman-shift is specific to a material and allows detailed material analysis [67]. The hexagonal grid of monolayer graphene exhibits characteristic peaks, the so-called (2D and G peaks). Defects and impurities are easily determined by analysing the spectrum [68]. In crystalline $In_xGa_{1-x}As$ films,

dislocations will activate phonon features [70, 71]. The indium fraction can be derived from the phonon's wave number shift [70, 71].

XPS measurements were performed by the AG Grundmeier from Paderborn University. An Omicron ESCA+ system at a base pressure of $< 1 \times 10^{-8}$ Pa and a XM1000 source with monochromatic Al K_α-radiation (1486.7 eV) is used. The angle between source and analyser is 102°. The take-off angle with respect to the surface plane was 60°. Measurements were performed without neutralisation at a constant pass energy of 100 eV for a survey and 20 eV for element spectra. The resolution is 0.07 eV. Data evaluation was performed using CasaXPS Version 2.3.23PR1.0. A proper overview of the basic principles and the measurement technique is presented in [72,73]. XPS is used to investigate the surface properties. Transferred graphene was analysed before and after cleaning. The basic XPS-principle is the photoelectric effect. The technique can be described by a three-step process: In the first step, the photo-ionisation takes place, then the excited electron travels through the crystal to the surface and escapes the crystal into the vacuum where it is detected [72]. The kinetic energy of the emitted electrons is measured and passes information of the analysed material, as it is directly related to the characteristic electron binding energy. The chemical state of a sample is analysed by the photo-ionisation energy fo the material core levels. Usually, XPS is a quite surface sensitive technology, as the mean free path of the emitted electrons within a material is quite low [72, 73].

TEM measurements were performed by the Prof. Sanchez group from Warwick University and by Thomas Riedl from AG Lindner from Paderborn University. A detailed survey on TEM is presented in [74]. In TEM, a high energy beam of electrons is shone through a very thin sample [74, 75]. The electrons interact with the atoms when the beam passes through the sample. The detected electrons reveal characteristic sample features like the crystal structure, chemical composition, crystal defects or grain boundaries on an atomic scale. Prior to measurement, the sample is thinned to a few nanometres to allow electron transmission [76]. The electrons are emitted from a hairpin or single-crystal filament [74,75]. Then, the electrons are focused into a small, thin, coherent beam by condenser lenses. The beam hits the sample

and electrons are scattered by the samples electrostatic potential [74,75]. The transmitted electrons are then detected and the intensity distribution reveals the atomic arrangement. By scanning the electron beam above the sample, high resolution images are taken [75]. Further, the chemical composition on the atomic scale is resolved by measuring the electron energy loss during the electron-sample-interaction [75].

Chapter 4

Graphene transfer and sample preparation

In this chapter, the graphene transfer onto oxide stripped GaAs substrates is explained. The PMMA handling stack removal from the graphene is discussed. Wet chemical cleaning and plasma treatment of the GaAs-graphene surface is described. The corresponding process parameters are given. Remote epitaxy of $In_xGa_{1-x}As$ on graphene covered GaAs is only possible for a single monolayer graphene on the GaAs substrate as elaborated in chapter 2. Therefore, the GaAs surface must be oxide-free and there must not be any residuals on the graphene surface. Here, GaAs wafers from *Wafer Technology Ltd.* and transfer graphene from *ACS materials* are used. In general, there are several methods to fabricate monolayer graphene, i.e. the Nobelprized scotch-tape method, graphene grown by CVD growth on copper foil or by graphitisation of SiC. The scotch-tape method is often used to obtain monolayer graphene flakes with a high structural quality for research applications. The experimental procedure is rather simple. However, the output is low and the flake size is limited a few μm^2. Larger graphene pieces are required to analyse the grown films employing HRXRD. SiC wafers form a monolayer graphene on the wafer surface, when exposed to high temperatures in an inert atmosphere. This method is scalable to entire wafers and a high quality graphene layer is achieved, but the graphene has to be peeled-off the SiC wafer. Although

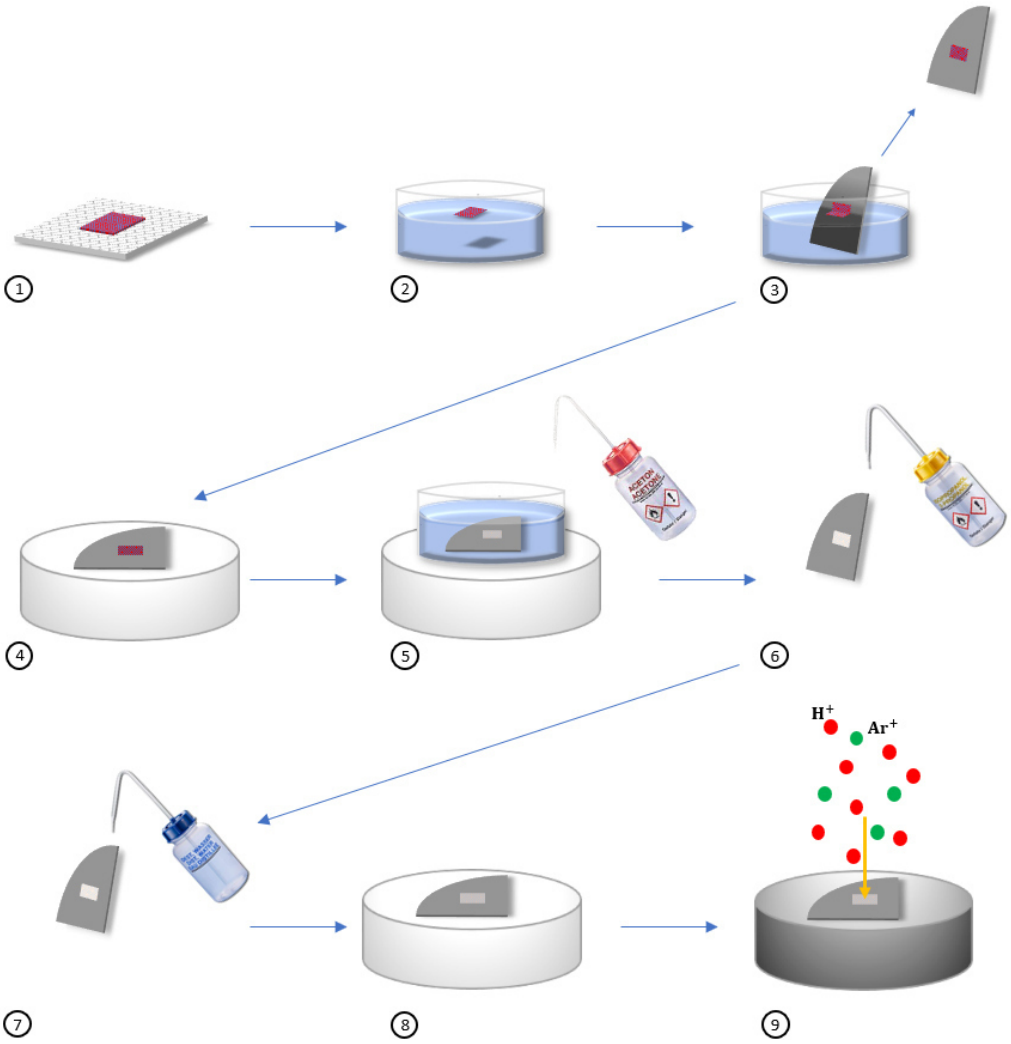

Figure 4.1: Process-flow scheme of the graphene transfer to the GaAs substrate and the further treatments to clean the graphene from polymere residuals.

this process might supply graphene with low defect densities, the fabrication and transfer process requires significant experimental know-how [10, 11, 17]. Monolayer transfer graphene is grown on copper foil by a CVD process and is commercially available on a wafer scale [77]. The graphene layer is covered by a 500 nm thick PMMA layer to stabilise the graphene during transport and transfer [77]. The copper is removed by etching. The graphene-PMMA stack can be transferred to any substrate and allows a high sample output. However, the PMMA film has to be removed prior to $In_xGa_{1-x}As$ overgrowth, but PMMA removal is reported to be rather difficult. Strongly adhering carbon chains, the so-called PMMA-G, sticks to the graphene layer [78, 79]. It was proposed to remove these PMMA residuals by thermal annealing at elevated temperatures from 300°C to 900°C in UHV, or inert gas [80–85], or by mild plasma cleaning [78, 79, 86–93]. Certain care has to be taken during sample cleaning, as a too harsh treatment damages the graphene layer.

The graphene transfer process to the GaAs substrates and the graphene treatment prior to overgrowth is shown schematically in figure 4.1. The graphene is wet transferred to the GaAs wafer, then the PMMA polymer is removed by acetone, IPA and DI-water rinse and finally, an in-depth plasma cleaning is done. A detailed description of each step follows:

(1-3) The as-delivered graphene is covered by PMMA. The graphene-PMMA stack lies on a sponge. Once placed in water, the sponge is soaked with water and the graphene is released. The graphene-PMMA stack floats on the water, due to the water's surface tension. The graphene-PMMA stack is picked up by a common filter-paper and a 4×4 mm piece is cut from the stack. The remaining graphene-PMMA stack is transferred back onto the sponged and stored in a fridge. The 4×4 mm piece floats roughly 20 min on the water. Within this period, graphene wrinkles and bulbs are relaxed [77]. During relaxation, a 10% HCl solution is mixed in a Petri dish. A GaAs quarter wafer is etched by the 10% HCl solution for 1 min under slight agitation, to remove the surface oxide, followed by DI-water rinse for a few seconds [94–96]. Then, the quarter is immersed into the water-filled beaker with the floating

graphene-PMMA stack. The graphene-PMMA stack is scooped by the GaAs substrate. The graphene-PMMA transfer should be done as fast as possible to avoid any GaAs wafer contamination. A GaAs oxide layer forms immediately in air [94, 96]. An oxide layer between graphene and GaAs substrate reduces the substrate-layer-interaction and might deny successful remote epitaxy.

(4) After graphene transfer, the GaAs wafer is held upright for 1 min to let excess water flow of the wafer. The sample is dried for 10 min at ambient conditions and then baked on a hot plate for 20 min at 100° C to increase the adhesion of the graphene to the GaAs wafer and to flatten the graphene [77].

(5-8) The next step is the PMMA removal. The sample is immersed in 50°C pre-heated acetone for 20 min [77]. Then, the sample is rinsed with IPA and DI-water and finally re-baked for 20 min at 100° C to remove any trapped water on the graphene and between graphene and GaAs substrate.

(9) The final step is an in-depth cleaning. Several methods were investigated. Their ability to prepare a proper GaAs-graphene surface for remote epitaxy is discussed in the next chapter 5 in further detail. As it turned out, a H-Ar-plasma cleaning step, performed in an ICP-RIE chamber suits best. The H-Ar-plasma removes PMMA polymer residuals adhering on a graphene surface and also any GaAs surface oxides. The process is divided into three steps with the detailed process parameters given in table 4.1. Firstly, the sample is treated with a hydrogen plasma. The RF-power applied to the platen is low, so that mainly hydrogen radicals interact with the sample surface. Secondly, the sample is treated by a H-Ar-plasma operated at low RF-powers and for short times referred to as mild plasma conditions. Thirdly, step one is repeated. The first and the third step are not required to efficiently remove the PMMA-residuals on the graphene, but they help

to achieve a clean graphene surface with fewer particles. The reason for this is unclear. Maybe, the first step removes contaminations in the chamber prior to sample etching and thus suppresses contaminants (re-)deposition. The last step may achieve a hydrogen saturated sample surface. A similar effect was reported in [86].

	P_{RF} (W)	P_{ICP} (W)	time (s)	H-flux (sccm)	Ar-flux (sccm)	pressure (Torr)
1^{st}	-	100	300	10	-	42.5
2^{nd}	3 - 5	100	15 - 30	10	5	42.5
3^{rd}	-	100	300	10	-	42.5

Table 4.1: Process parameters of the plasma cleaning process.

Chapter 5

Results

In the following chapter, the results of the sample preparation, the sample cleaning, the remote heteroepitaxial $In_xGa_{1-x}As$ growth and the ex-situ characterisation are discussed. The chapter is divided into three parts. Firstly, the results of different sample cleaning procedures are presented. A way to prepare commercially available transfer graphene for remote epitaxy is shown. Then, the initial stage of $In_xGa_{1-x}As$ film growth, the $In_xGa_{1-x}As$ nucleation on graphene covered GaAs substrates, is discussed. Various indium concentrations and substrate temperatures were tested. Lastly, remote heteroepitaxy of thicker $In_xGa_{1-x}As$ films with indium concentrations up to $x = 0.70$ is presented. The strain relaxation mechanism, the degree of strain relaxation and the dislocation density is analysed by HRXRD-, TEM- and Raman-spectroscopy-measurements.

5.1 Sample preparation towards remote epitaxy

In this section, several cleaning procedures and their ability to prepare the GaAs-graphene sample surface for remote epitaxy are investigated. The key for remote epitaxy is to ensure, there is exactly one monolayer graphene on the substrate. Any additional atoms or molecules, for example, PMMA-polymer residuals adhering to the graphene or a GaAs oxide layer between

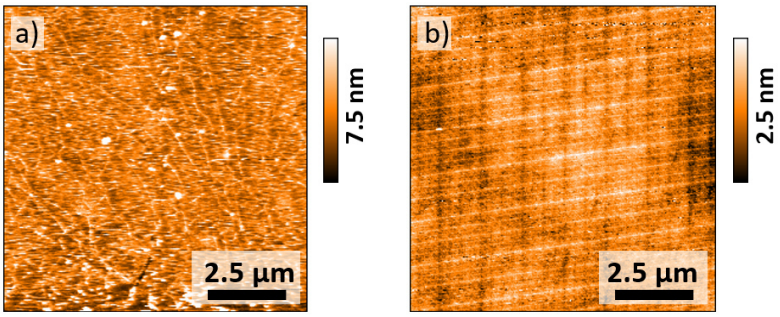

Figure 5.1: a) AFM image of the transferred graphene layer after cleaning with solvents. The surface roughness is $\sigma = (1.6 \pm 0.1)$ nm. b) AFM image of a 1 min etched GaAs substrate in 10%-HCl. The roughness is around $\sigma = (0.3 \pm 0.1)$ nm.

graphene and GaAs substrate, increase the substrate-layer interaction gap and prevent remote epitaxy on the graphene layer. In the following section, thermal annealing in inert gas, in UHV and plasma cleaning are discussed as potential preparation methods. It is shown, that a mild plasma process followed by UHV thermal annealing properly prepares the sample surface for remote epitaxy.

First, the GaAs-graphene sample surface is analysed after the graphene wet transfer and wet chemical PMMA removal described in the last chapter 4. An exemplary AFM image is shown in figure 5.1a). For comparison, also the oxide stripped GaAs substrate is depicted in figure 5.1b). These images provide a reference data set used to compare different cleaning schemes. While the bare GaAs substrate exhibits a rather smooth surface with a RMS-roughness of $\sigma = (0.3 \pm 0.1)$ nm, the substrate covered with a graphene layer exhibit a roughness of $\sigma = (1.6 \pm 0.1)$ nm. A structure is observed on the sample surface resulting from graphene wrinkles and bulbs [97]. Some elevated islands indicate Cu or SiO_x nanoparticles incorporated during the graphene fabrication process [81, 97]. This image clearly shows the existence of remaining polymer residuals on the graphene surface and agrees with other reports [80, 81, 83, 84, 97]. $In_xGa_{1-x}As$ remote epitaxy is not possible on such samples. A monolayer graphene mounted properly on an oxide stripped GaAs substrate, should exhibit a similar surface roughness as the bare substrate

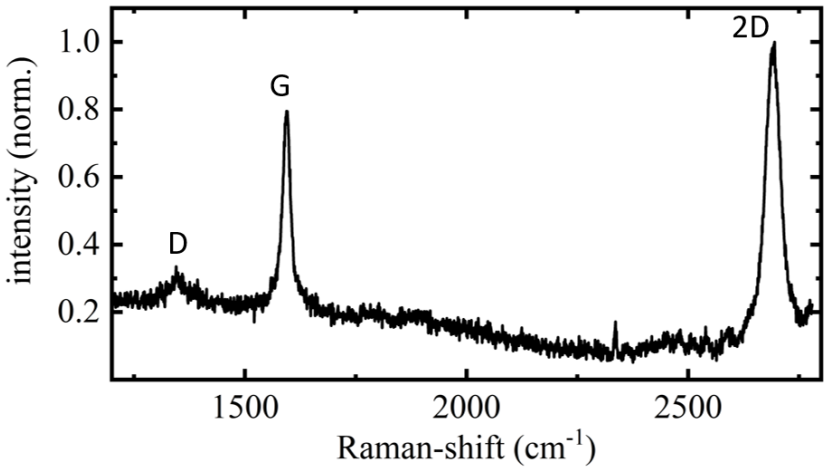

Figure 5.2: Raman-spectra of a graphene monolayer after wet transfer to the GaAs substrate and wet chemical cleaning.

in figure 5.1b), because in principle there is just one atom more in height on the substrate. The Raman-spectrum of the GaAs-graphene sample measured by the collaboration partners from the AG Goldhahn from the Otto-von-Guericke University Magdeburg is shown in figure 5.2. It reveals an intact graphene monolayer similar to other monolayer transfer graphene spectra reported in literature [13, 86]. The intensity of the defect related D-peak at (1354 ± 1) cm^{-1} is weak compared to the characteristic 2D- and G-graphene-peak at (1593 ± 1) cm^{-1} and (2694 ± 1) cm^{-1}, respectively. The Lorentzian shaped 2D-peak with a FWHM of 21 ± 1 cm^{-1} reveals monolayer graphene [71]. The graphene is intact after the transfer to the GaAs substrates.

Further analysis of the GaAs-graphene interface was performed by XPS-measurements done by AG Grundmeier from the Paderborn University. Figure 5.3a) shows the carbon related binding energy spectrum, which is quite similar to other XPS-spectra of intact graphene or to highly ordered pyrolytic graphene spectra [73]. The binding energy spectra of the in GaAs bound As and Ga atoms are presented in figure 5.3b) and c), respectively. The As and Ga related spectra clearly show a peak attributed to the presence of As_2O_3 and Ga_2O_3 [18, 73]. This verifies a surface oxide in-between the GaAs substrate and the monolayer graphene [73]. The oxide layer forms after the

oxide stripe, during wet graphene transfer, when the GaAs is in contact with water and thus corrodes, until the water is evaporated [18].

To sum up, three key points can be addressed by an in-depth cleaning method to ensure a substrate-graphene surface is suitable for remote epitaxy:

1. The graphene layer surface must be free of any residuals
2. The GaAs surface underneath the graphene needs to be oxide free to minimise the substrate-layer-interaction gap.
3. The graphene must not be damaged during cleaning. The graphene monolayer should exhibit a similar Raman- and XPS-spectrum as after transfer and wet chemical cleaning.

The first point is addressed by a suitable graphene cleaning technique with a high selectivity. PMMA residuals need to be removed from the surface while keeping the graphene intact. There are several reports on cleaning graphene from polymer residuals, some focusing on the wet chemical cleaning and baking in UHV or inert gas, while others employ plasma etching. A comprehensive overview of a variety of cleaning approaches is presented in [85]. Although the cleaning approaches were mainly tested for transfer monolayer graphene on Si or SiO_2, they should be adaptable to monolayer graphene on GaAs.

Tackling the second point is rather difficult; removing any oxide in-between graphene and GaAs once the graphene is placed onto the GaAs substrate is challenging. However, heating the sample above the GaAs deoxidation point at roughly 590°C in the MBE system possibly deoxidates the GaAs substrate, even with a graphene layer on top. The sample annealing in hydrogen gas or sample treatment by hydrogen plasma may be another promising approach as hydrogen atoms exhibiting a sufficient energy can tunnel through a monolayer graphene layer, and then react with the substrate oxide [78, 98, 99]. The etch products, i.e. the oxygen atoms, may also tunnel through the graphene, or escape the interface by pinholes in the graphene layer.

The comparison of different cleaning approaches is difficult, because of

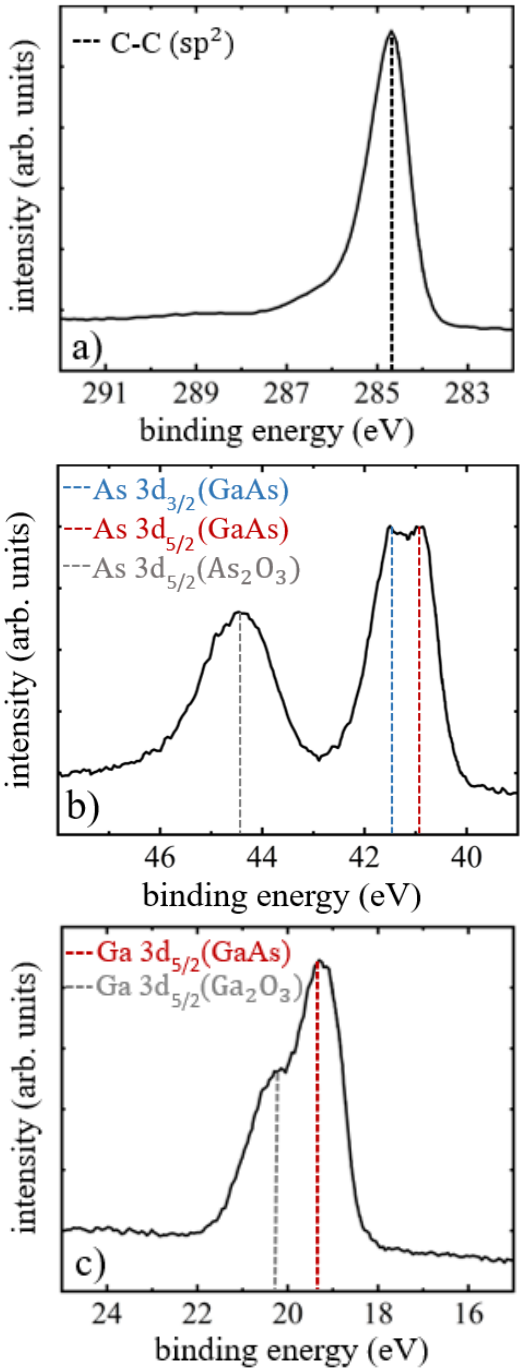

Figure 5.3: XPS-spectra of the GaAs-graphene sample surface after wet graphene transfer and wet chemical cleaning. The a) carbon, b) gallium and c) arsenic related binding energies are shown. A peak attributed to the presence of As_2O_3 and Ga_2O_3 is observed. This verifies a surface oxide in-between the GaAs substrate and the monolayer graphene [73].

researcher's definition of the term clean. A clean graphene surface is often associated with a smoother surface after treatment, or no degradation in Raman- or XPS-spectra, sometimes even with an enhancement of carrier mobility in transport measurements. So far, there is no report on "clean" transfer graphene suitable for remote epitaxy. In [18] it is proposed, that transfer graphene is not suitable for remote epitaxy. In contrast, in [10, 13] annealing in UHV and inert gas was performed before successful remote homoepitaxy on transfer graphene.

In this work, several promising cleaning processes, related to those mentioned in literature were tested. A suitable process, which removes residuals is preselected by AFM measurements of the sample surface. Analysing the surface properties in more detail, i.e. the graphene quality in terms of defects and the presence of surface oxide, is done by Raman- and XPS-measurements. Finally, remote epitaxial growth of single crystalline $In_xGa_{1-x}As$ films verifies a proper surface preparation.

5.1.1 Thermal annealing of graphene covered GaAs

There are several approaches in literature on cleaning graphene from polymer residuals by thermal annealing in air, inert atmosphere or UHV. Thermal annealing is rather simple and is reported to remove most polymer residuals from the graphene surface [80–83, 85]. Following these approaches, annealing in inert gas, in air or in UHV was tested at temperatures $\geq 300°C$. Figure 5.4 shows the AFM image of the sample surface after 1 h long treatments in inert H_2-gas, in air and in UHV. The surface morphology changed compared to the only wet chemically cleaned sample shown in figure 5.1a). But, the surface morphology is still significantly rougher compared to the smooth surface depicted in figure 5.1b). The surface roughness of all three samples is $\sigma = (2.0 \pm 0.5)$ nm and varies for different measured surface areas. Thermal annealing removes only some part of the PMMA residuals. Wrinkles, bulbs and Cu or SiO_x nanoparticles become more prominent. This is in agreement with other reports [81,85,97]. Several black or white lines appear in the AFM images arising from the cantilever dragging over nanoparticles and graphene

wrinkles. However, in-between the wrinkled graphene, the graphene surface seems to become cleaner. Neither an increase of the annealing time of up to 5 h and temperatures of up to 620°C nor combining different thermal annealing steps, for example, 1 h annealing in air plus 1 h annealing in UHV, did improve the surface quality. In [78, 79] it is reported, that thick PMMA handling stacks mounted on graphene are composed of several phases. While most of the PMMA is PMMA-B and PMMA-A with randomly ordered hydrocarbon chains, a thinner PMMA-G layer exists on top of the graphene. In the PMMA-G, the hydrocarbon chains are aligned and strongly adhere to the graphene [78, 79]. PMMA-B is simply removed by an acetone bath and PMMA-A by thermal annealing. In contrast, TEM investigation on a mono-

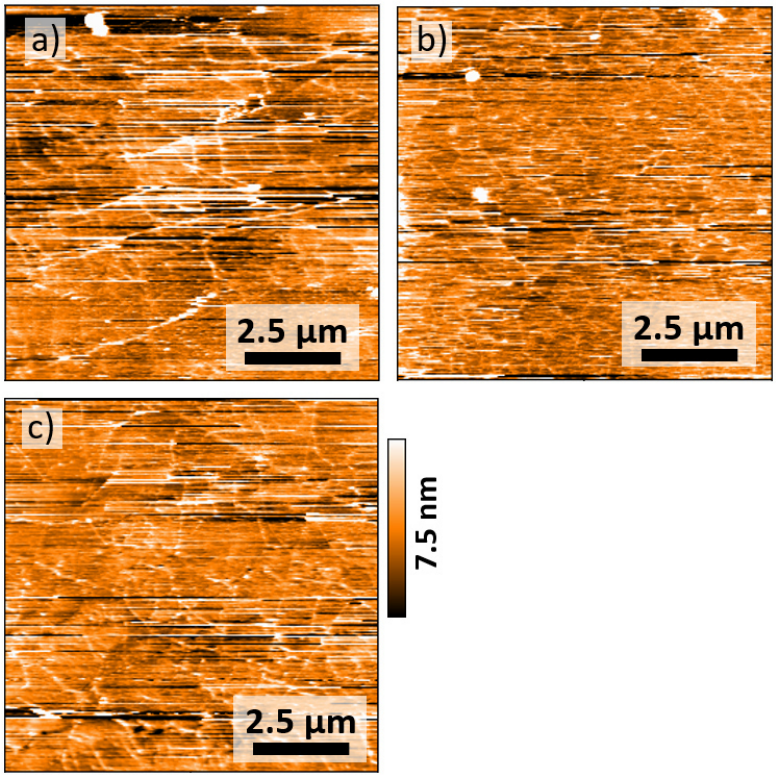

Figure 5.4: AFM images of transferred graphene layers after wet chemical cleaning and thermal annealing above 300°C following the approaches proposed in [80–83, 85]. a) 1 h in H_2, b) 1 h in air, c) 1 h in H_2 followed by 1 h in UHV. Some black and white lines are caused by the cantilever drag above nanoparticles and wrinkles.

layer CVD-graphene cleaned in air/H_2/Ar at up to 300° C show remaining PMMA-G residuals, Cu and SiO_x nanoparticles adhering on the sample surface [80, 81, 85, 97]. Probably, most of the residuals observed on the sample surface in figure 5.4 are PMMA-G and nanoparticles. Higher annealing temperatures of up to 900°C in UHV [84, 85] are reported to clean the graphene surface with higher efficiency, but also damage the graphene lattice, as at some point the carbon bonds in the graphene layer are also cracked. This approach lacks also from a non-stable GaAs surfaces without the supply of excess As at such high temperatures. Cleaning would only be possible in the MBE growth chamber in an As flux. The MBE system is usually only operated up to roughly 620°C. The background pressure increases exponentially with temperature, so the risk of contamination of the growth chamber becomes larger. The maximum annealing temperature tested here, was roughly 620°C. This temperature is above the GaAs thermal deoxidation temperature of 590°C, so in principle the thermal annealing can also remove the oxide in-between the GaAs substrate and the graphene. The sample morphology looks similar to the AFM images shown in figure 5.4.

Without any further in-depth analysis, $In_xGa_{1-x}As$ MBE was performed at low temperatures of 300°C on all samples as described above. Details on the growth procedure were already reported in chapter 3. A 200 nm thick film was grown. The growth rate was 1 $Å s^{-1}$ and the As_4 pressure was 0.9×10^{-5} mbar. Unfortunately, the $In_xGa_{1-x}As$ film grown on graphene exhibits an extremely large surface roughness with individual large polycrystalline islands. In contrast, the $In_xGa_{1-x}As$ film grown on the bare GaAs substrate simultaneously was rather smooth with a 10×10 μm surface roughness of $\sigma = (0.6 \pm 0.1)$ nm. In conclusion, $In_xGa_{1-x}As$ remote heteroepitaxy on thermal annealed GaAs-graphene samples is not possible. Probably, thermal annealing whether performed in inert H_2-gas, in air or in UHV is not suitable to clean the GaAs-graphene surface. There are still residuals remaining on the surface and probably the oxide layer in-between the GaAs substrate and the graphene layer is also not removed.

5.1.2 Plasma etching of graphene covered GaAs

As an alternative approach, plasma etching was tested to clean graphene from polymer residuals and GaAs oxides. Plasma etching is a well-known process in semiconductor research and is accessible for mainly every device fabrication lab, so graphene cleaning benefits from the high quality standards and reproducibility. Several publications claim clean graphene surfaces after plasma exposure by Ar [90], O [91, 92], H [79, 86–89], H+CH_4 [93] or H+CF_4 [78]. The basic principle is always the same: The plasma conditions are tailored, so only the polymer residuals on the graphene surface are removed, while ensuring graphene monolayer integrity. In Ar-ICP, the polymer residuals on the graphene surface are affected by the ion bombardment energy. The ion-electron-recombination causes an excitation of the polymer oxygen atoms. The residuals are oxidised [85, 90]. In a two-step process, oxygen and hydrogen remote plasmas are used. The polymer residuals are directly bombarded by the oxygen atoms and although the cleaning is effective, a degradation of the graphene layer is observed in Raman-spectra [91,92]. In H-, H+CH_4- and H+CF_4-plasma operated at high densities in the isotropic/remote etching regime, the sample surface reacts mainly with thermal radicals. However, the H-atoms and -ions can tunnel through the graphene at sufficient energy. This may offers an elegant way, to remove the GaAs oxide layer in-between GaAs and graphene by H-atoms or -ions [98, 99]. In advanced etching processes, small amounts of CH_4 and CF_4 are used to etch Si-nanoparticles or to heal defects in the graphene layer [78, 93].

In this thesis, the focused is on mild H-plasma and mild H+Ar-plasma etching of the GaAs-graphene surface related to the approaches reported in [79,86–89]. First, the effect of a pure inductive-coupled-hydrogen-plasma was tested. The plasma is generated above the sample as described in chapter 3, so the sample surface interacts mainly with H-radials. The process parameters were tuned to achieve a high density plasma. The maximum pressure for a stable H-plasma is 42.5 mTorr at a H_2-flux of 10 sccm and an ICP-power of 100 W. Figure 5.5a) shows an AFM images of a 1 min long cleaned GaAs-graphene sample surface. The overall roughness of $\sigma = (0.7 \pm 0.1)$ nm is

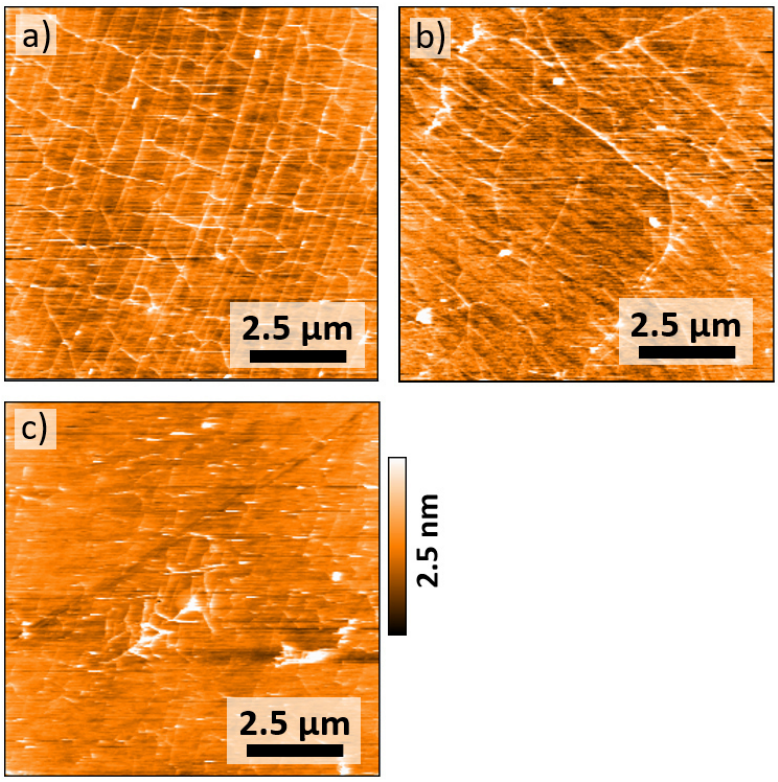

Figure 5.5: AFM images of transferred graphene layers after cleaning with solvents and plasma treatment. a) only ICP, b) ICP plus $P_{RF} = 5$ W for 20s, c) ICP plus $P_{RF} = 5$ W for 60s

lower, in comparison to any thermal annealing process. A distinct pattern of wrinkles is visible and amongst the wrinkles, the surface is rather smooth. Increasing the etching time to several minutes did not change the surface morphology. This agrees with theoretical molecular dynamics simulations which predict a process frame (H-atom's energies up to < 10 eV) where most of the H-atoms are reflected or adsorbed on the graphene lattice. The graphene lattice remains protected from any chemical attack, due to the delocalized π-electrons in the sp^2-hybridised state [98, 99]. In these conditions, the penetration probability of H-atoms through the graphene lattice is low and a rather high etch selectivity is obtained. The drawback is, that the oxide layer underneath the graphene is neither attacked. $In_{0.15}Ga_{0.85}As$ MBE growth results in polycrystalline film growth.

In consequence, a RF-signal is added to the sample platen in a second etching step, leading to the bombardment of the sample by H^+-ions, which exhibit a higher kinetic energy. The H^+-ion probability to penetrate and to adsorb on the graphene lattice increases [98, 99]. The ion-dose and of course the ion-energy is tuned by the applied RF-platen-signal. Within this process frame the oxide layer on the GaAs substrate is exposed to penetrating H-ions, while the graphene lattice itself is hydrogenated. Hydrogenated graphene is protected from the adsorption of residuals during sample transport in air and Dehydrogenation is achieved by thermal annealing in UHV [78]. Certain care has to be taken by adjusting the RF-power and etching time, as too harsh conditions cause a reaction of the H^+-ion and the C-atoms of the graphene lattice. A low RF-power of $3-5$ W applied to the platen for $15-30$ s suits best. Note, due to heavy machine usage, a slight drift of the process parameters was observed. Typically, the H-plasma needs a few seconds to ignite and become stable. This strongly impacts the etch process reproducibility as it only takes a few seconds duration. Adding 5 sscm Ar-gas during this etching step, stabilises the plasma generation and increases process reproducible.

The GaAs-graphene surface of a sample cleaned by both steps, an inductive-coupled-H-plasma step (P_{ICP} = 100 W, 1 min) followed by an H+Ar-plasma with an added RF signal to the platen (P_{ICP} = 100 W, P_{platen} = 5 W, 20 s), is depicted in the AFM image in figure 5.5b). The overall surface roughness is $\sigma = (0.8 \pm 0.1)$ nm. There is barely any difference in the surface morphology and roughness compared to the sample only treated 1 min by the inductive-coupled-H-plasma. Both AFM images display some graphene wrinkles and an otherwise smooth surface.

Too long exposure during the second step, causes graphene etching. Figure 5.5c) shows a GaAs-graphene sample surface after 60 s H+Ar-plasma treatment with an applied RF-power to the platen of 5 W. Obviously, the wrinkled graphene is etched.

The necessity of the second plasma step is revealed by XPS-measurement of the plasma treated GaAs-graphene interface. Figure 5.6 shows the XPS-spectrum of the Ga, As and C related binding energies after plasma cleaning, and after additional thermal annealing in UHV for 5 min at 620°C. The As_2O_3

and the Ga_2O_3 peak successively decease after H+Ar-plasma treatment and after additional UHV thermal annealing in comparison to the only transferred and wet chemical cleaned GaAs-graphene surface shown already in figure 5.3. Note, that the spectra in figure 5.6 also reveal, that the GaAs does not re-oxidate during sample transfer from the RIE-chamber or MBE-chamber to the XPS-set-up in air. This proves, that the monolayer graphene protects the GaAs surface. The graphene remains on the sample surface and withstands the plasma treatment and UHV thermal annealing. The XPS-spectra of the graphene related carbon peak in figure 5.6a) and d) reveals an intact graphene film [73]. The FWHM of the sp^2-hybridised carbon peak after thermal annealing is 0.9 ± 0.1 eV and in the same order of magnitude as values reported in literature for highly oriented pyrolytic graphite and monolayer transfer graphene [73, 79]. A slight C-related binding energy shift of (0.3 ± 0.1) eV towards lower binding energies indicates hydrogenation of the graphene layer, and the shift back of (0.6 ± 0.1) eV towards larger bindings energies after UHV thermal annealing, indicates graphene dehydrogenation [73].

Figure 5.7 shows the Raman-spectrum of a monolayer graphene after plasma cleaning and UHV thermal annealing. The Lorentzian shaped 2D-peak intensity decreases and the FWHM= 26 ± 1 cm^{-1} slightly increases compared to the peak intensity of the only wet chemically cleaned graphene. The intensity of the defect related D-peak is still low. However, there appears the disorder related D'-peak [71]. In [78] a similar behaviour was observed. Most of the graphene layer is probably intact, but contaminated by adatoms during transfer or cleaning suppressing the sp^2-hybridisation.

After thermal annealing in UHV for 5 min at 620° the H+Ar-plasma treated sample $In_{0.15}Ga_{0.85}As$ MBE growth was performed at 300°. A 200 nm thick film was grown at a growth rate 1 $Å s^{-1}$ and an As_4 pressure of 0.9×10^{-5} mbar. Indeed, single crystalline growth was revealed by HRXRD measurements. Details are described in the following section.

To summarise this section, several cleaning approaches to remove PMMA residuals from the graphene surface and native GaAs oxides between the GaAs substrate and the graphene monolayer were discussed. It was shown, that thermal annealing in air, in inert H_2-gas and in UHV up to 620°C is

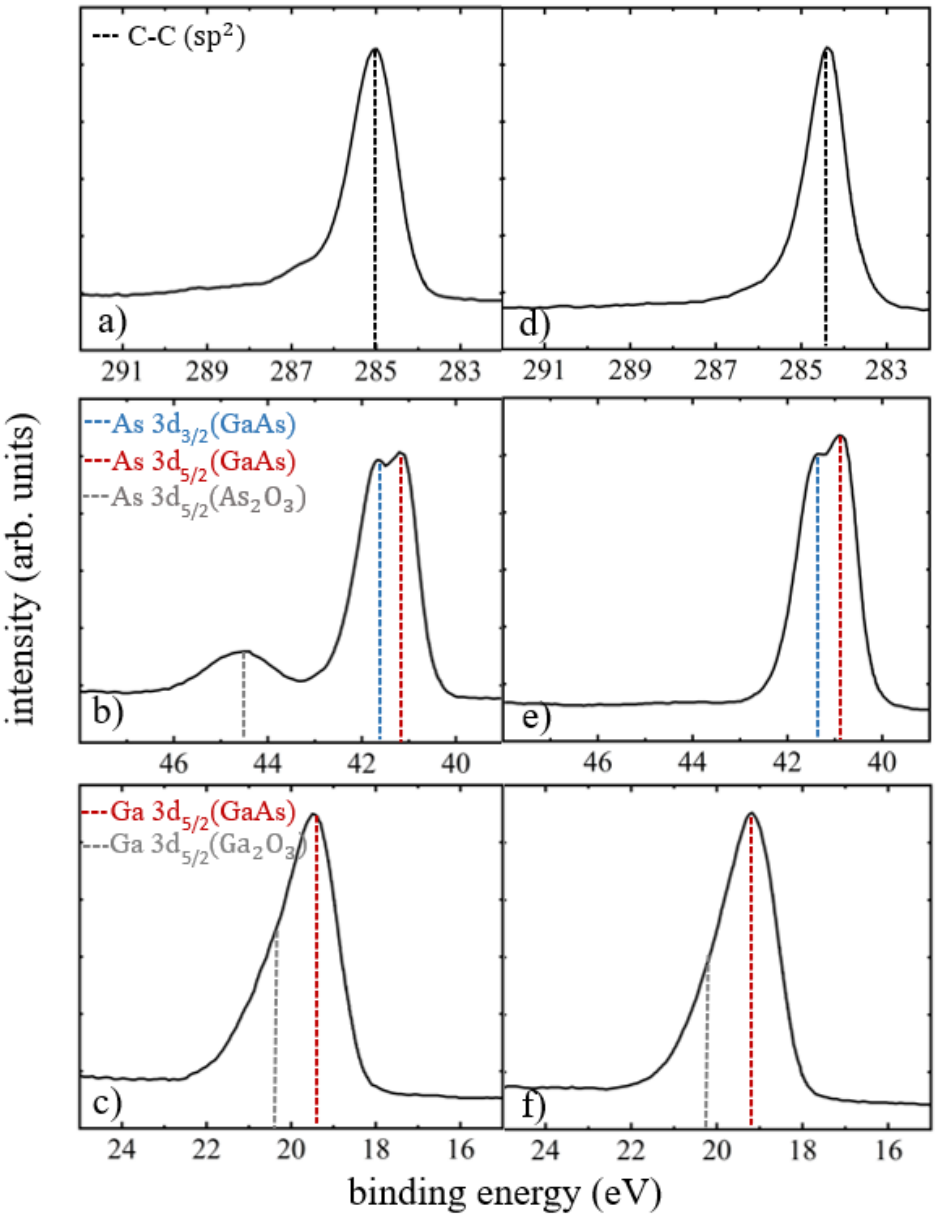

Figure 5.6: XPS-spectra of the GaAs-graphene sample surface after a)-c) H+Ar-plasma treatment and d)-f) after additional UHV thermal annealing. The carbon, gallium and arsenic related binding energies are shown. The peaks attributed to the presence of As_2O_3 and Ga_2O_3 vanish after complete cleaning. The graphene peak indicates an intact graphene layer.

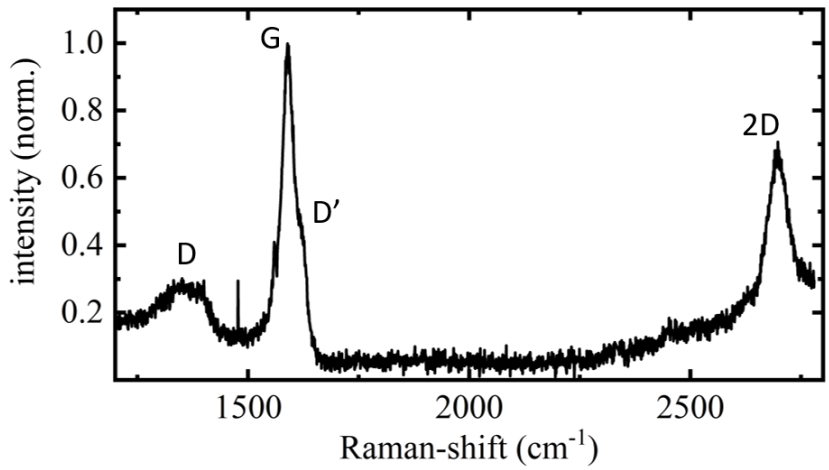

Figure 5.7: Raman-spectra of a monolayer graphene after carefully optimised H+Ar-plasma treatment followed by UHV thermal annealing.

not sufficient to remove all polymer residuals and GaAs oxides from the graphene surface and from the GaAs surface, respectively. A suitable plasma process was developed to prepare wet transferred monolayer graphene on GaAs substrates for $In_xGa_{1-x}As$ remote heteroepitaxy. XPS- and Raman-spectra reveal the PMMA polymer and GaAs oxide removal, with almost intact graphene.

5.2 $In_xGa_{1-x}As$ nucleation on graphene covered GaAs

After successful sample cleaning, $In_xGa_{1-x}As$ nucleation layers were grown on the graphene covered GaAs substrates. Only small material amounts were deposited to investigate the initial nuclei formation on the graphene covered GaAs. The bare GaAs was investigated for comparison. Growth was performed as described in chapter 3.

For a first test, $In_{0.15}Ga_{0.85}As$ was deposited on the graphene covered GaAs for 5 s at a growth rate of 1 $Å s^{-1}$, an As_4 pressure of 0.9×10^{-5} mbar and a temperature of 300°C. This equals a nominal coverage of $n.c. = 0.5$ nm. Figure 5.8 shows an SEM image of the sample surface after deposition. The graphene covered sample area (1) is on the left side of the image. Randomly distributed small islands on the surface can be identified. In contrast, on the bare GaAs on the right side (3), typical GaAs deoxidation pits, resulting from the sample thermal annealing at 620°C above the GaAs deoxida-

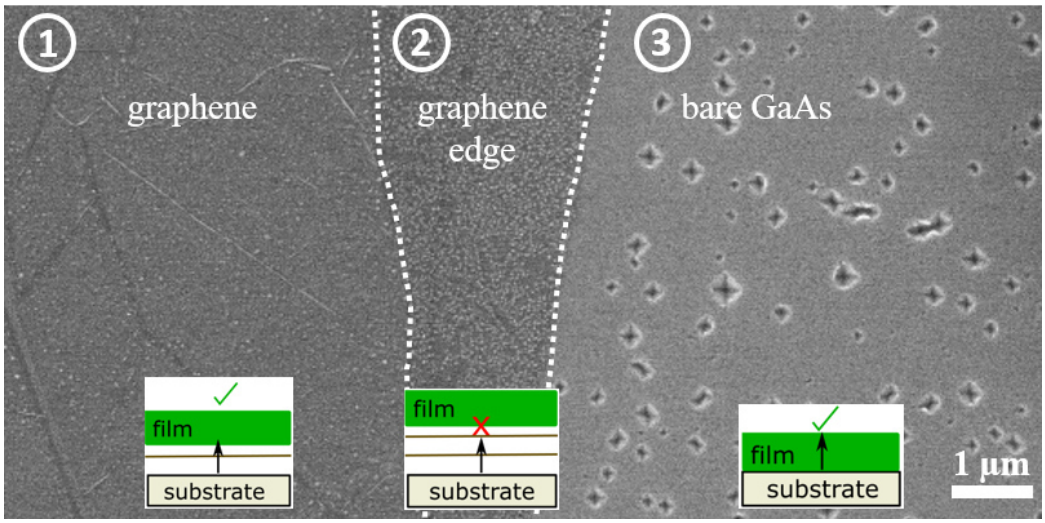

Figure 5.8: SEM image of the edge of a graphene piece covering the GaAs substrate. The image was taken after plasma cleaning, UHV thermal annealing and deposition of 0.5 nm $In_{0.15}Ga_{0.85}As$. Small nucleation islands on the graphene indicate a reduced substrate influence. Typical deoxidation pits are observed on the bare GaAs surface.

tion temperature, are observed. Amongst these pits, the surface seems to be smooth and the $In_{0.15}Ga_{0.85}As$ growth started in layer-by-layer growth mode, as commonly observed. The H+Ar-plasma treated sample is transferred in ambient air to the MBE set-up. During transfer, the bare GaAs re-oxidises, whereas the monolayer graphene protects the GaAs surface from re-oxidation. Thermal deoxidation in UHV removes the oxide of the bare GaAs sample area and creates the typical deoxidation pits. The graphene covered substrate area does not display any visible pits. Re-oxidation is prevented, even if the sample is transferred within air. This agrees with the measured XPS-spectra of a plasma treated and UHV thermal annealed sample shown in figure 5.6b), so in conclusion, there is an intact graphene surface on the GaAs substrate.

Another aspect is the size of the nuclei. The graphene edge area (area 2) exhibits elevated $In_{0.15}Ga_{0.85}As$ islands (brighter spots) and a darker background, compared to area 1. Here, the graphene layer is maybe folded. This possibly happens during wet graphene transfer, so there is a bilayer graphene observed in area 2 rather than a monolayer. It is reported, that the leaking GaAs substrate potential nearly vanishes for more than a monolayer graphene and growth happens in elevated, randomly oriented islands [10, 11], so the SEM image shown in figure 5.8 reveals: $In_{0.15}Ga_{0.85}As$ is grown on the bare GaAs (area 3) by a strong substrate-layer interaction. Large $In_{0.15}Ga_{0.85}As$ islands are grown on the edge area (area 2), due to barely any layer-substrate interaction. Smaller $In_{0.15}Ga_{0.85}As$ islands are grown on the graphene covered GaAs substrate (area 1). This is a clear indication, that the islands on the monolayer graphene covered GaAs substrate are grown under the influence of the leaking GaAs substrate potential.

5.2.1 Dependence of nuclei distribution and size on temperature and indium concentration

After the first trial, the nucleation process was investigated more quantitatively. Figure 5.9a)-c) shows three different samples with different amounts of $In_{0.15}Ga_{0.85}As$ deposited on the graphene surface. The nominal coverages are $n.c. = 0.5$ nm, $n.c. = 2$ nm and $n.c. = 5$ nm. All samples

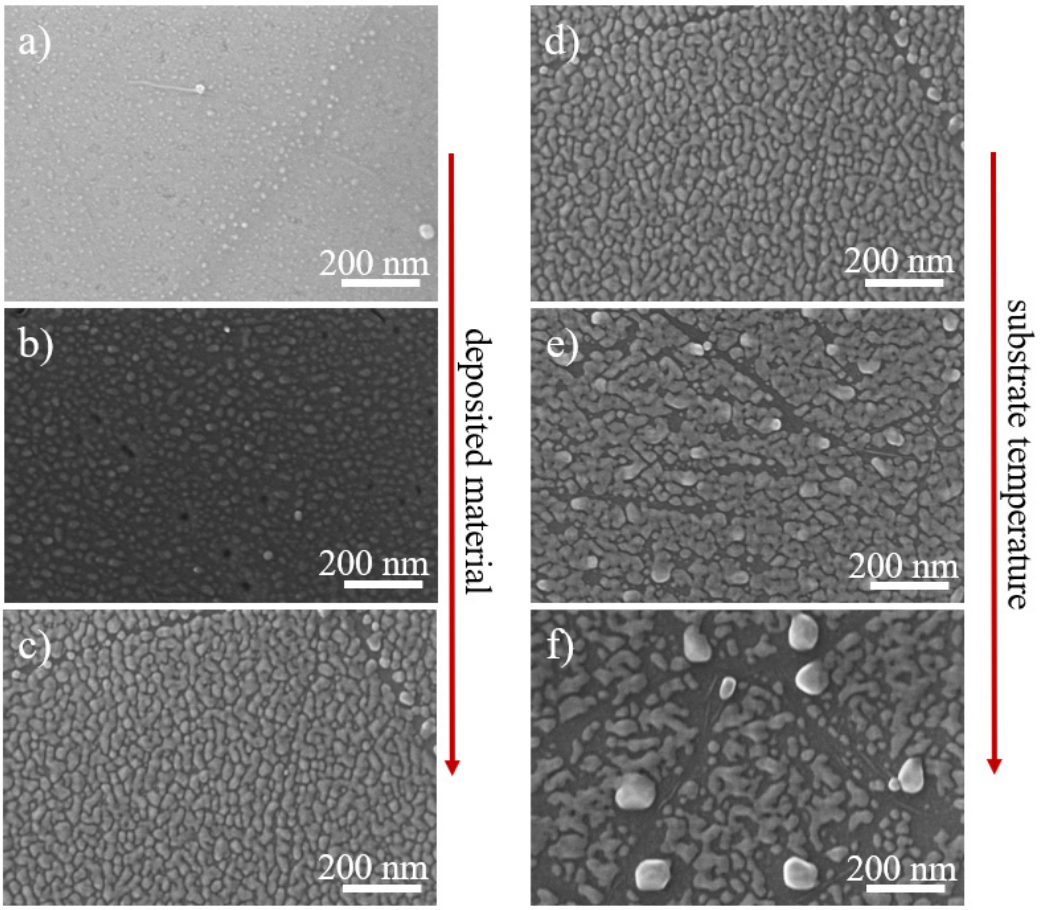

Figure 5.9: SEM images of several $In_{0.15}Ga_{0.85}As$ nucleation layers grown on graphene covered GaAs: a) 0.5 nm, b) 2 nm and c) 5 nm deposited at $T = 300°C$ and 5 nm deposited at d) $T = 300°C$, e) $T = 385°C$, f) $T = 485°C$.

were overgrown at 300°C at a growth rate of 1 $Å s^{-1}$ and As_4 pressure of $(0.9 \times 10^{-5} - 1.2 \times 10^{-5})$ mbar, see chapter A for the individual As_4 pressures. In figure 5.9a), small randomly distributed nuclei are observed on the graphene surface. Increasing the deposited material amount to 2 nm and 5 nm, first leads to growing nuclei and then to their coalescence. The wettability of the $In_{0.15}Ga_{0.85}As$ on the graphene covered GaAs is low and there is no wetting layer observed on the graphene, so the growth happens in the Volmer-Weber growth mode.

Next, the nucleation temperature influence on the nuclei size and distribution is investigated. Figure 5.9d)-f) shows $In_{0.15}Ga_{0.85}As$ layers grown on

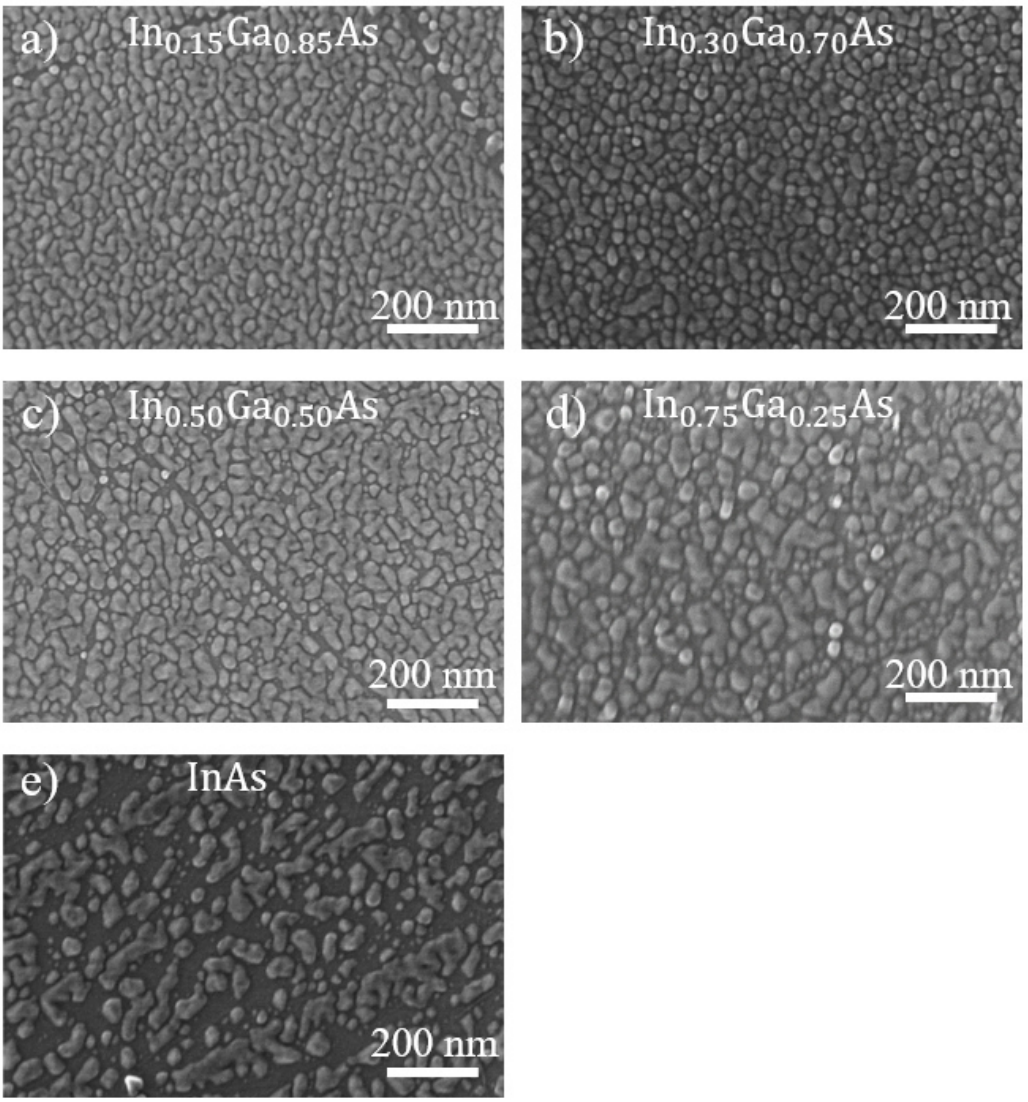

Figure 5.10: SEM images of several $In_xGa_{1-x}As$ nucleation layers with a nominal coverage of 5 nm grown at $T = 300$°C: a) $x = 0.15$, b) $x = 0.30$, c) $x = 0.50$, d) $x = 0.75$, e) $x = 1.0$.

a graphene covered GaAs substrate with a nominal coverage of $n.c. = 5$ nm. The substrate temperature is 300°C, 385°C and 485°C. A clear trend is revealed: Higher substrate temperatures lead to larger islands and incomplete surface coverage. A few large islands are observed in figure 5.9e) and f) and probably they are formed due to a ripening process. The larger island size may be related to a higher adatom mobility at higher temperatures, due to

an Arrhenius-like temperature dependence of the adatom mobility. At higher temperatures, the adatoms exhibit a longer diffusion length, so they migrate longer on the surface before incorporation. Thus larger islands are formed. Adsorbed adatoms are incorporated in larger nuclei rather than forming new nuclei on the graphene. Similar behaviour is observed at high indium concentrations. Figure 5.10 shows several $In_xGa_{1-x}As$ samples with a nominal coverage of $n.c. = 5$ nm grown at 300°C. The individual island size increases and becomes more inhomogeneous at higher indium contents. At $x \geq 0.75$ the graphene surface is only partially covered. Probably the more mobile In atoms exhibit a larger diffusion length on the graphene compared to the Ga atoms, and thus favour the growth of larger nuclei. In summary, nucleation layer growth is most successful at low temperatures up to indium concentrations of $x < 0.75$.

$In_xGa_{1-x}As$ growth below 300°C was not tested, because the growth mechanism changes: The As sticking coefficient becomes non-zero and growth in As overpressure leads to the deposition of amorphous As on the surface; below 300°C only stoichiometric growth is possible.

The $In_xGa_{1-x}As$ nuclei temperature stability is checked by ramping the substrate temperature in constant As_4 overpressure up to 485°C after nucleation. Once 485°C is reached, the temperature is ramped back to 300°C. Then, the sample surface is analysed in SEM. Neither a change in the nuclei size nor in surface coverage was observed. Ripening can be neglected. At high temperature the nuclei are stable. This is an important result considering the fabrication of thicker layers or heterostructures grown a elevated temperatures. The substrate-graphene-layer interaction stabilises them. In contrast, in [8] it is reported, that without any layer-substrate interaction, a thin GaAs film deposited on graphene covered Si becomes rough and forms a polycrystalline film at elevated temperatures.

5.2.2 TEM investigation of individual nuclei

To gain further insight into the nucleation process, cross section TEM measurements were performed by the collaboration partners of AG Lindner from

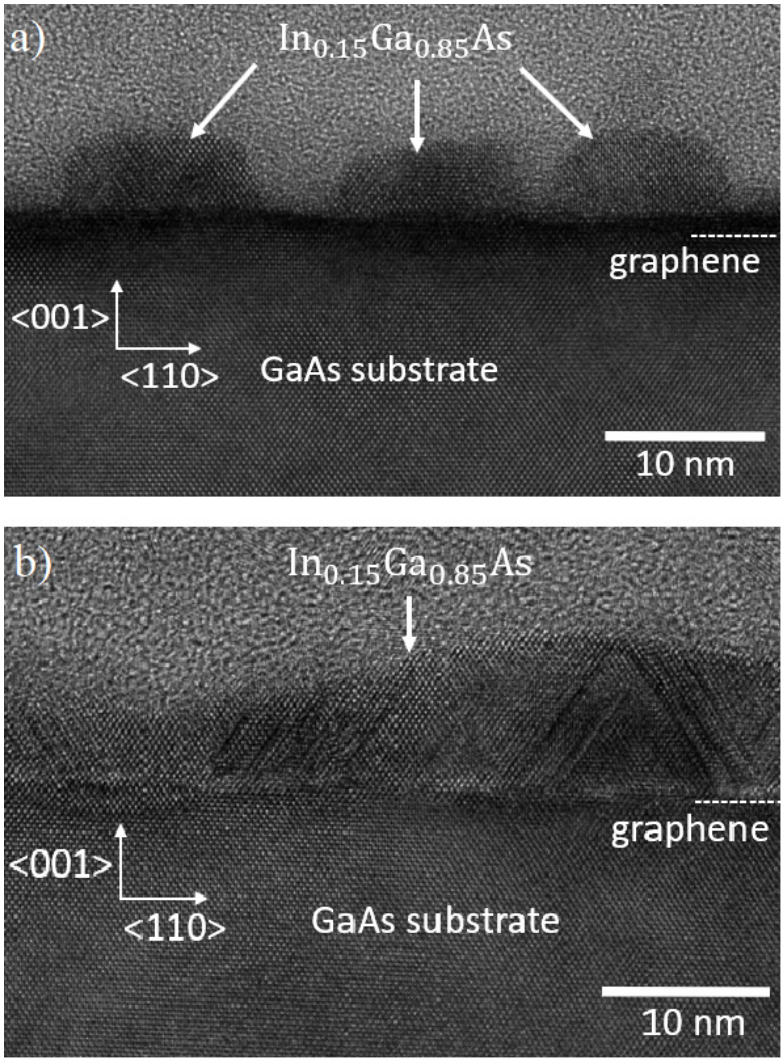

Figure 5.11: TEM image of an $In_{0.15}Ga_{0.85}As$ nucleation layer grown on graphene covered GaAs substrate: a) nominal coverage = 2 nm, b) nominal coverage = 5 nm.

Paderborn University. Figure 5.11a) and figure 5.11b) show the cross section TEM image of two samples with a nominal $In_{0.15}Ga_{0.85}As$ coverage of $n.c.$ = 2 nm and $n.c.$ = 5 nm, grown at 300°C. The SEM image (fig.:5.9b)-c)) of both samples was already discussed above. In figure 5.11a), three separated nuclei are observed. The height is (6 ± 1) nm and the width (13 ± 2) nm. A high magnification image of a single nucleus is shown in figure 5.12a). The $In_{0.15}Ga_{0.85}As$ nucleus and the GaAs substrate exhibit the same crystal

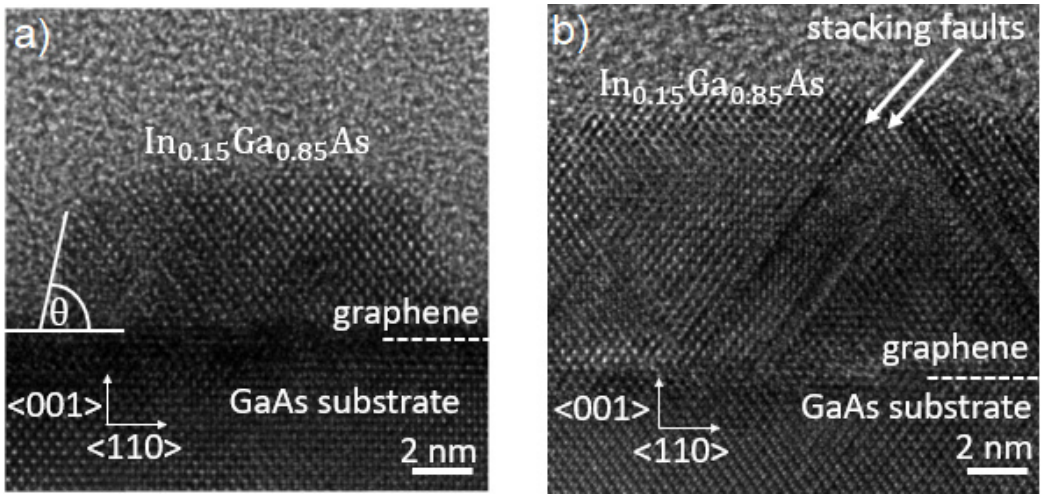

Figure 5.12: High magnification TEM image of a single island of an $In_{0.15}Ga_{0.85}As$ nucleation layer grown on graphene covered GaAs: a) nominal coverage = 2 nm, b) nominal coverage = 5 nm.

structure and orientation. No crystal defects are observed in this nucleus [76]. Other investigated nuclei confirm this result. In contrast, in figure 5.11b) a coalescent film is observed. The height is in a range between 5 nm to 9 nm. Stacking fault defects are observed at higher magnification; see figure 5.11b). Unfortunately, the graphene layer cannot be observed here. The cross-section interface is contaminated by the deposition of residuals during sample preparation, thus limiting the maximum resolution at the interface [76].

The defect formation mechanism in these nuclei grown on the graphene surface in not clear. Commonly, crystal defects are introduced to relax the build-up compressive strain in an $In_{0.15}Ga_{0.85}As$ film grown on GaAs above a critical thickness. However, the critical $In_{0.15}Ga_{0.85}As$ film thickness on GaAs is roughly 100 nm.

The stacking fault defects may originate from islands nucleation at or in graphene layer pinholes [12,100]. A small pinhole in the graphene layer introduces a small step, sketched in figure 5.13. The crystal lattice is slightly distorted around the step and stacking fault defects may be generated. However, this would not explain the absence of stacking fault defects in the nucleation layer before coalescence and their introduction immediately after coalescence.

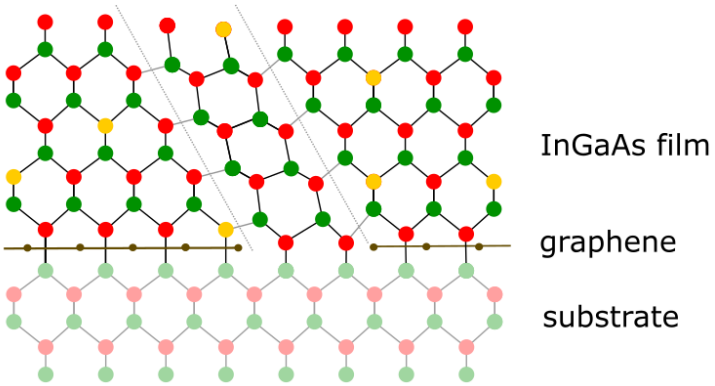

Figure 5.13: Schematic sketch of an $In_xGa_{1-x}As$ film grown on a defective graphene layer. The graphene pinhole introduces a step, where stacking fault defects may be generated.

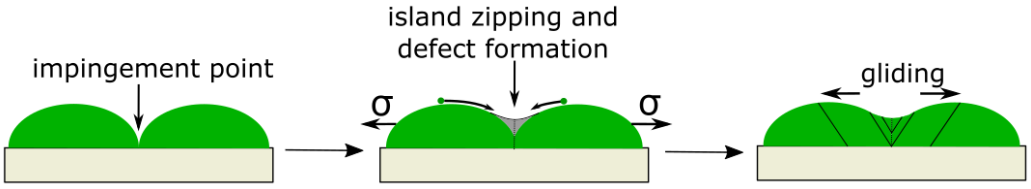

Figure 5.14: Schematic model of island zipping. First, the islands coalescent at the impingement points. Then, they zip together. The new formed island is strained. The strain is relaxed by the introduction of defects.

Defects may be also introduced at the nuclei impingement points when nuclei exhibiting slightly different fronts match [12].

Another possible mechanism is the nuclei zipping [101–103]). The two nuclei in close contact can reduce the surface energy by zipping and forming one nuclei [101–103]. Zipping is driven by the reduction in the overall surface energy and is accomplished by elastic deformation of the nuclei, thereby imposing a cost of increased strain energy [100–102]. It is commonly discussed for polycrystalline film growth [101, 102], but was also observed for AlN islands deposited on Si [103]. The stacking faults in the coalescent $In_xGa_{1-x}As$ films may be introduced by island zipping, refer to figure 5.14 for a zipping mechanism scheme. After zipping, the newly formed $In_xGa_{1-x}As$ island is strained. The strain may not be relaxed by a film slip over the graphene surface due to the island's surface tension, but by introducing crystal de-

fects [101,102]. The defect formation energy is smaller than the surface energy gained by island zipping. A more detailed analysis of the grown nuclei may be possible with STEM measurements and subsequent strain investigations in the future.

To sum up, the $In_xGa_{1-x}As$ nucleation on graphene covered GaAs was discussed in this section. An intact graphene layer after sample cleaning is confirmed by the nucleation of small $In_xGa_{1-x}As$ islands on the graphene surface. No re-oxidation of the underlying GaAs substrate is observed, in accordance with the results presented in the last section. The influence of the temperature and the indium concentration on the nucleation behaviour, i.e. nuclei size and surface coverage, was discussed. Homogeneous surface coverage was observed at 300°C and low indium concentrations. TEM investigations were performed on selected $In_{0.15}Ga_{0.85}As$ nuclei. The nuclei are defect free before coalescence, but afterwards, defects are observed.

5.3 $In_xGa_{1-x}As$ film growth on graphene covered GaAs

In this section, the overgrowth of the $In_xGa_{1-x}As$ nucleation layer is discussed. Thicker $In_xGa_{1-x}As$ films ($0 < x \leq 0.7$) of up to 200 nm suitable for heterostructure fabrication, were grown at different temperatures and on different nucleation layers to find an optimal growth parameter window for smooth $In_xGa_{1-x}As$ film growth on graphene covered GaAs with low defect densities. In the first subsection, growth of $In_xGa_{1-x}As$ films by a one-step process is discussed, and the surface morphology and crystallographic properties are investigated by AFM, HRXRD and Raman-spectroscopy. In the second section, growth by a two-step approach is employed and the samples are again characterised by AFM, HRXRD and Raman-spectroscopy. Lastly, growth and characterisation of thinner $In_xGa_{1-x}As$ films is performed, so the thin film relaxation behaviour immediately after island coalescence is analysed.

5.3.1 One-step $In_xGa_{1-x}As$ film growth

After $In_xGa_{1-x}As$ layer nucleation, it is tested, if remote heteroepitaxy also works for entire films grown on graphene covered GaAs. Although the TEM measurements show individual well oriented nucleation islands in respect to the substrate crystal orientation, only rather small sample cross-sections were analysed. A more general investigation of the crystalline properties is possible by HRXRD measurements averaging over a large $In_xGa_{1-x}As$ film volume. HRXRD measurements performed on the $In_xGa_{1-x}As$ nucleation layer exhibit a too low diffracted beam intensity of the $In_xGa_{1-x}As$ reciprocal lattice reflex, due to the small probed $In_xGa_{1-x}As$ volume. Therefore, thicker $In_xGa_{1-x}As$ films were grown and investigated. Similar growth parameters were used for layer nucleation. The growth rate was 1 $Å s^{-1}$, the substrate temperature was 300°C and the As_4 beam-equivalent pressure was adjusted from 0.9×10^{-5} mbar for $In_{0.13}Ga_{0.87}As$ films to 2.2×10^{-5} mbar for $In_{0.70}Ga_{0.30}As$ films. For individual detailed growth parameters, please refer

to the growth sheets in the appendix.

Figure 5.15 shows the 1×1 μm^2 surface morphology of 5 nm, 25 nm and 200 nm thick $In_{0.13}Ga_{0.87}As$ films grown on graphene covered GaAs. A rough surface morphology with many islands and a surface roughness of $\sigma = (1.1 \pm 0.1)$ nm confirms the island growth mode on the graphene. The film roughness after deposition of 25 nm $In_{0.13}Ga_{0.87}As$ results in an even rougher film with a roughness of $\sigma = (2.0 \pm 0.1)$ nm, see 5.15b). Hills and valleys become even larger and some islands are merged together. In contrast, the sample surface of a 200 nm thick $In_{0.13}Ga_{0.87}As$ film shown in figure 5.15c) is smoother. The films roughness decreases to $\sigma = (0.9 \pm 0.1)$ nm. Increasing the amount of deposited material leads to the coalescence of the islands. The smoothest film is observed for the 200 nm thick $In_{0.13}Ga_{0.87}As$ film. The surface quality seems to improve for thick layers. This promising result indicate suitable growth conditions for thick $In_{0.13}Ga_{0.87}As$ films on wet transferred, plasma cleaned and UHV annealed transfer graphene on a GaAs substrate.

In the next step, the film's indium concentration is increased. Figure 5.15d)-f) shows the surface morphology of 200 nm thick $In_xGa_{1-x}As$ films with different indium concentrations. The indium concentrations and the corresponding surface roughnesses are shown in table 5.1.

indium concentration	surface roughness
$x = 0.13$	(0.9 ± 0.1) nm
$x = 0.25$	(0.8 ± 0.1) nm
$x = 0.50$	(1.9 ± 0.1) nm

Table 5.1: Surface roughness obtained from the evaluation of the AFM measurements of 200 nm thick $In_xGa_{1-x}As$ films grown at 300°C.

The surface is smooth for the samples with indium concentrations of $x \leq 0.25$. Figure 5.15c) reveals, there are large islands on the $In_{0.50}Ga_{0.50}As$ film surface, indicating distinct island growth. The surface smootheness may be tailored by enhanced growth parameter optimisation. For example, in [10, 13] a two step growth process is suggested. The layer nucleation is performed at low temperature and overgrowth is done at elevated temperature.

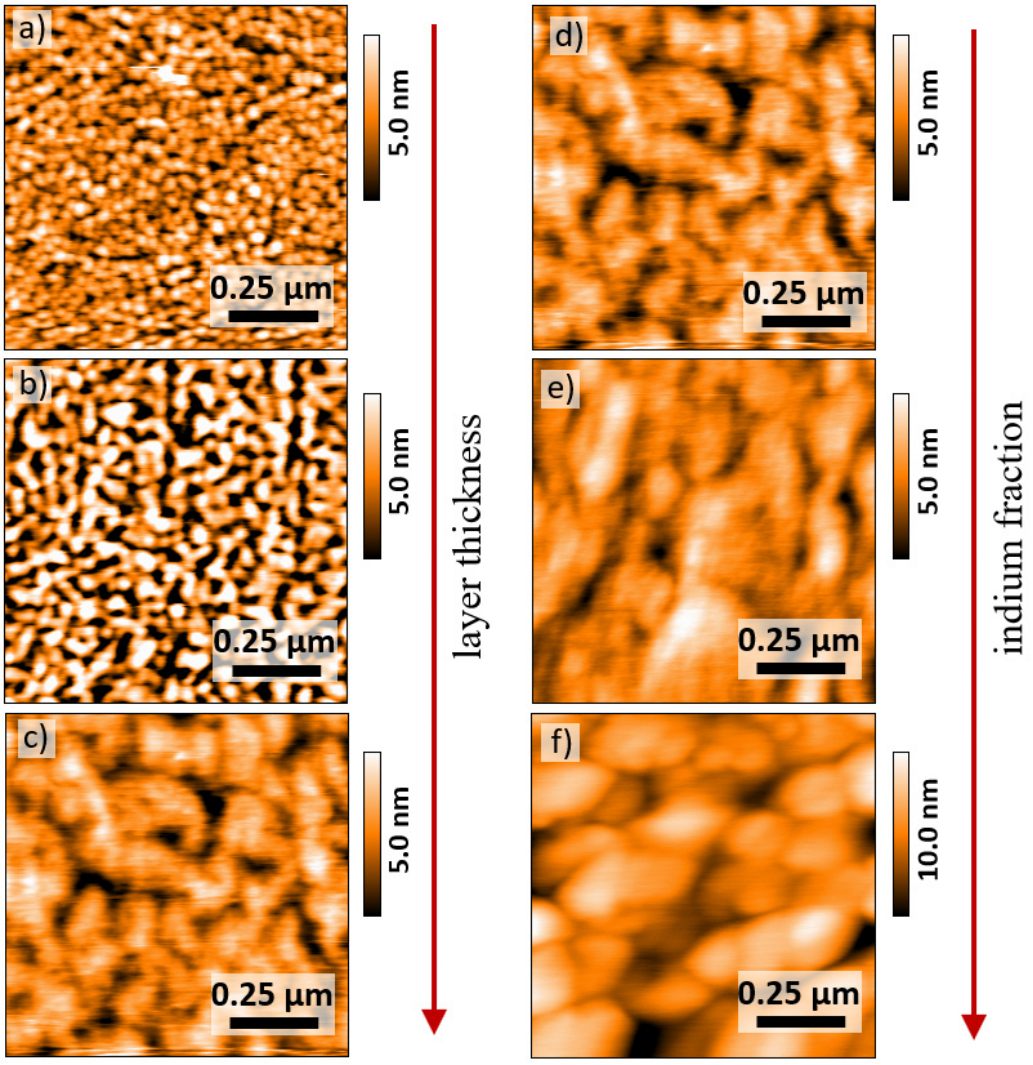

Figure 5.15: a)-c) $In_{0.13}Ga_{0.87}As$ films of various thickness grown on graphene covered GaAs at 300°C: a) 5 nm, b) 25 nm, c) 200 nm. d)-f) 200 nm thick $In_xGa_{1-x}As$ films with different indium concentrations: d) $x = 0.13$ e) $x = 0.25$, f) $x = 0.50$.

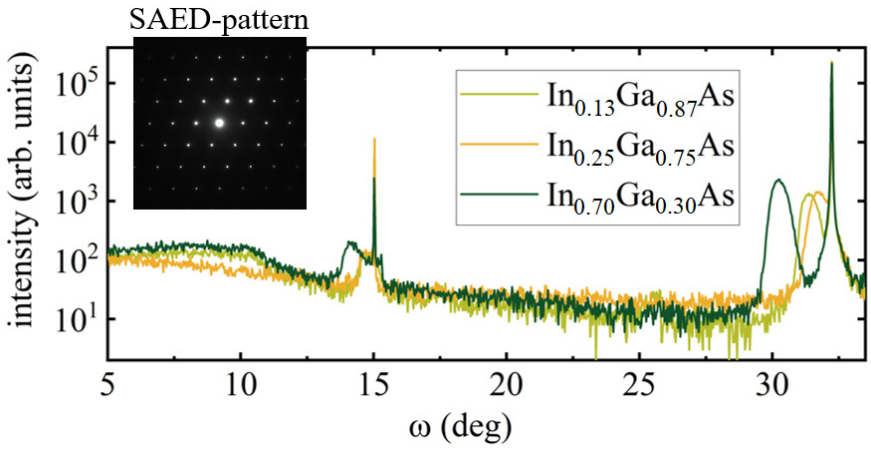

Figure 5.16: ω-2θ-scans of 200 nm thick $In_{0.13}Ga_{0.87}As$ grown at 300°C and a SAED image of the film, revealing single crystalline phase.

A similar approach was also tested here and is discussed in the next subsection. $In_xGa_{1-x}As$ film growth was also done with larger indium concentration of $x \leq 0.70$. The surface was dull and partially milky after growth. Large hills of up to a hundred nanometres in height were observed, confirming that more indium causes growth of samples with a rougher surface. Probably the formation of larger islands is due a higher fraction of indium atoms exhibiting a larger mobility. Similar behaviour was already discussed for the $In_{0.15}Ga_{0.85}As$ film nucleation, see section 5.2.

The $In_xGa_{1-x}As$ film crystal structure is analysed by HRXRD measurements. Figure 5.16 shows ω-2θ-scans along the (00l) direction. These were acquired in a wide angular range to determine the $In_xGa_{1-x}As$ ($x \leq 0.70 \pm 0.02$) film orientation. Following the Bragg equation (2.17), individual intense reflexes only occur for certain crystal planes within the $In_xGa_{1-x}As$ film and GaAs substrate. The (004)- and (002)-GaAs-reciprocal lattice reflex is observed for $\omega \approx 32°$ and $\omega \approx 16°$, respectively. These values belong to the intense reflexes in the spectrum depicted in figure 5.16 and serve as reference values. There is a slight angular shift of the GaAs substrate peak positions in comparison to the theoretical values, which is due to the apparatus uncertainty in the measurement of absolute angles, as described in chapter 3. Next to the GaAs substrate peaks, a second peak at smaller angles is visible

in each scan. These two peaks correspond to the $In_xGa_{1-x}As$ film. Their angular shift with respect to the GaAs peak, indicates a larger lattice constant orthogonal to the surface. Larger indium concentrations cause larger separation to the GaAs substrate peak. The $In_xGa_{1-x}As$ film peaks are less intense, which is due to the limited $In_xGa_{1-x}As$ film thickness and due to inhomogeneous broadening by crystal defects within the film. The most important observation here is, there are no other peaks in the ω-2θ-spectra revealing the single crystalline film phase and (001)-film orientation. No polycrystalline grains with different crystalline orientations are present in the film. This result is confirmed by the selected area electron diffraction (SAED) pattern of the 200 nm thick $In_{0.13}Ga_{0.87}As$ film, shown in figure 5.16. The diffraction pattern of a single crystalline film is clearly shown. [8, 9] report on GaAs-(111) films grown on graphene covered Si, due to the low Si-graphene-GaAs interaction. In contrast, the samples grown here exhibit a sufficient GaAs-graphene-$In_xGa_{1-x}As$ interaction so the substrate's (001)-orientations governs the $In_xGa_{1-x}As$-(001) film orientation. One the one hand, film and substrate orientation equals, on the other hand the substrate potential is so weak, that the $In_xGa_{1-x}As$ nucleates in islands as revealed in the last section 5.2. This proofs remote heteroepitaxial $In_xGa_{1-x}As$ growth of a single crystalline film. Note, the vicinity around the GaAs (111)-reciprocal lattice reflex was separately checked for the appearance of any peak, to neglect any $In_xGa_{1-x}As$-(111) film growth.

RSMs of the GaAs and $In_xGa_{1-x}As$ (004)- and (-2-24)-reciprocal lattice reflex were measured, to gain more detailed information on the $In_xGa_{1-x}As$ film crystalline structure, on the strain relaxation behaviour and on the dislocation density in the film grown on the graphene covered GaAs. For comparison, $In_xGa_{1-x}As$ growth is also investigated on bare GaAs. RSMs are examplarily shown and discussed for a 200 nm thick $In_{0.13}Ga_{0.87}As$ film. The RSMs of films with larger indium concentration were analysed in the same way and the results are presented later.

Figure 5.17 shows the (004)-RSMs of an $In_{0.13}Ga_{0.87}As$ film grown on graphene covered GaAs and figure 5.18 for comparison on bare GaAs. The RSMs were taken at four different azimuth angles ϕ rotated by 90°. Thus,

the measurements were performed along the [110]- ($\phi = 0°, 180°$) and [-110]-direction ($\phi = 90°, 270°$). For $\phi = 0°, 180°$ the incident plane includes the [110]-direction and for $\phi = 90°, 270°$ the incident plane includes the [-110]-direction. The intense GaAs substrate peaks in figure 5.17 and 5.18 are labelled by S and the $In_{0.13}Ga_{0.87}As$ film peaks by F. Figure 5.17b) and 5.18b) show a close-up image, to highlight the substrate and film reflex and the most interesting features. An intensity distribution similar to an ellipse is observed in both figures, but with different width in q_{xy} direction.

The $In_{0.13}Ga_{0.87}As$ films grown on graphene covered GaAs exhibit a broader ellipse intensity distribution compared to films grown on bare GaAs, indicating a higher film defect density as slightly tilted or twisted crystallites exhibit diffraction for slightly different incident beam angles. As shown in chapter 3, the dislocation density in cubic crystals is related to the (004)-reciprocal lattice rocking curve FWHM described by equation (3.2). Rocking curve scans of the $In_{0.13}Ga_{0.87}As$ film peak were measured, the FWHM was derived and the dislocation density was calculated, see table 5.2 for an overview.

	on graphene		on bare GaAs	
	[110]	[-110]	[110]	[-110]
(004)-rock. curve FWHM (°)	0.30 ±0.02	0.25 ±0.02	0.16 ±0.02	0.27 ±0.02
dis.-density (10^8 cm^{-2})	21 ±3	15 ±1	6 ±1	17 ±2
In fraction (%)	13.0 ± 1.5			

Table 5.2: Values obtained from the evaluation of the (004)- and (-2-24)-RSM of a 200 nm thick $In_{0.13}Ga_{0.87}As$ film grown at 300°C.

Both FWHM-values obtained for measurements along the [110]- ($\phi = 0°, 180°$) and along the [-110]-direction ($\phi = 90°, 270°$) were averaged. The $In_{0.13}Ga_{0.87}As$ films grown on graphene covered GaAs exhibit larger FWHM-values and thus larger dislocation densities, however, the difference between the values obtained in the [110]- and [-110]-directions is smaller compared to $In_{0.13}Ga_{0.87}As$ films grown on bare GaAs. Their FWHM is larger in the [110]-direction while films grown on bare GaAs exhibit a larger FWHM in the [-110]

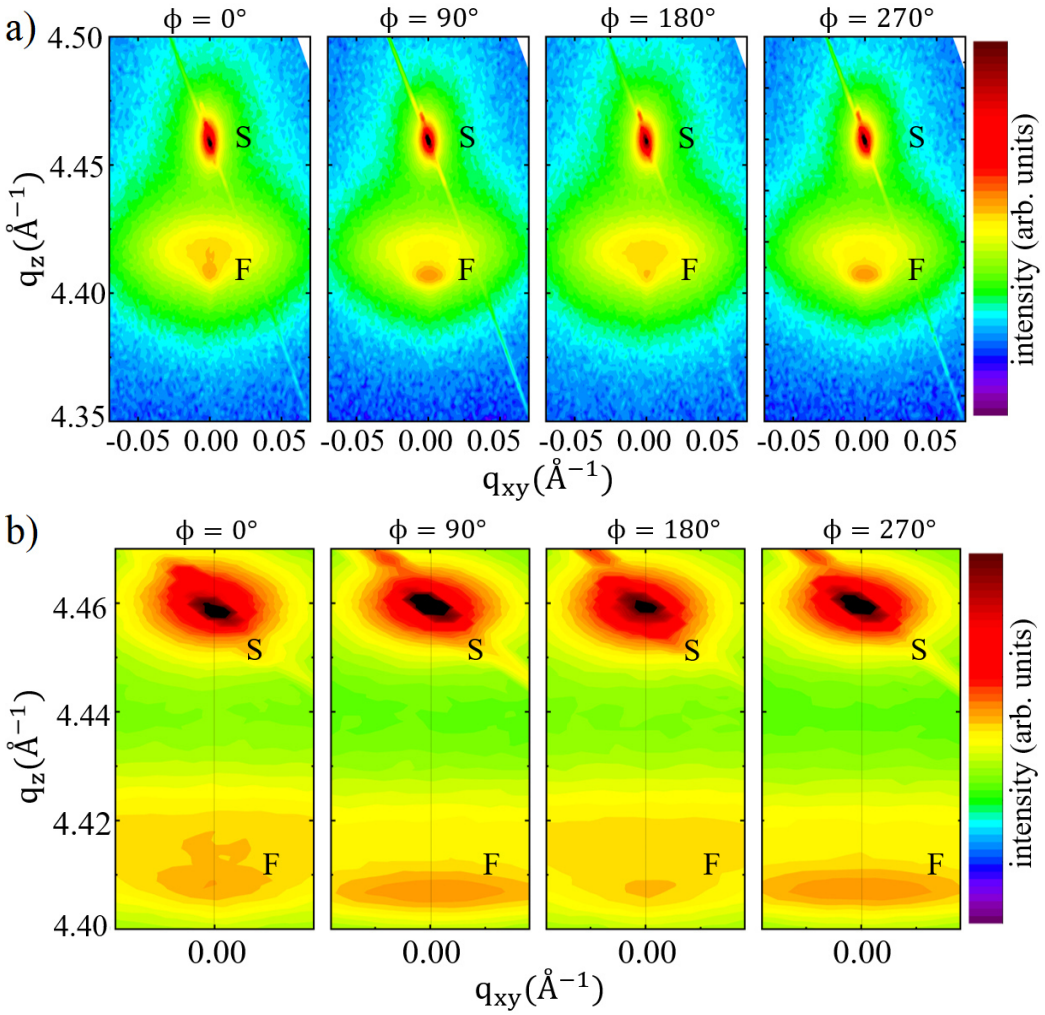

Figure 5.17: (004)-RSMs of a $In_{0.13}Ga_{0.87}As$ films grown on graphene covered GaAs at 300°C. A larger scanned area is shown in a) and a close-up in b).

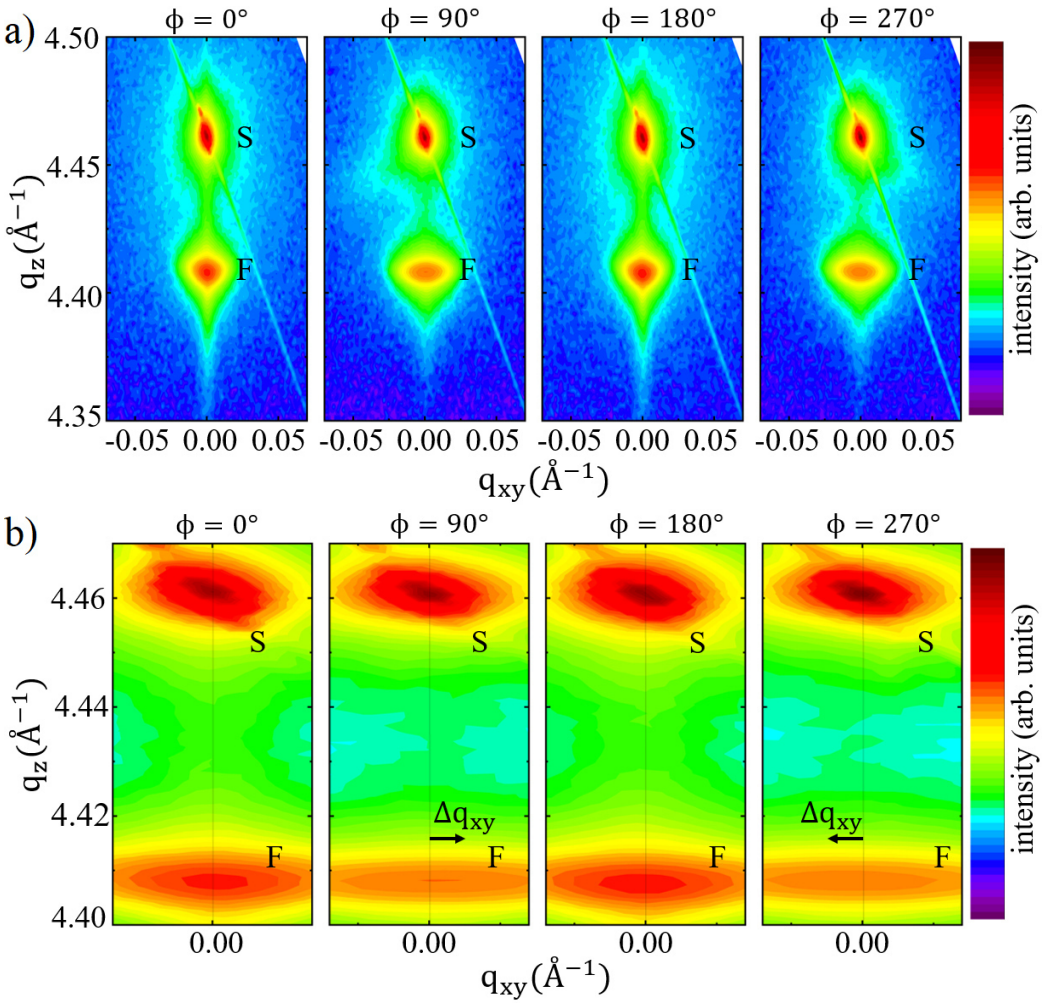

Figure 5.18: (004)-RSMs of a $In_{0.13}Ga_{0.87}As$ films grown on bare GaAs at 300°C. A larger scanned area is shown in a) and a close-up in b).

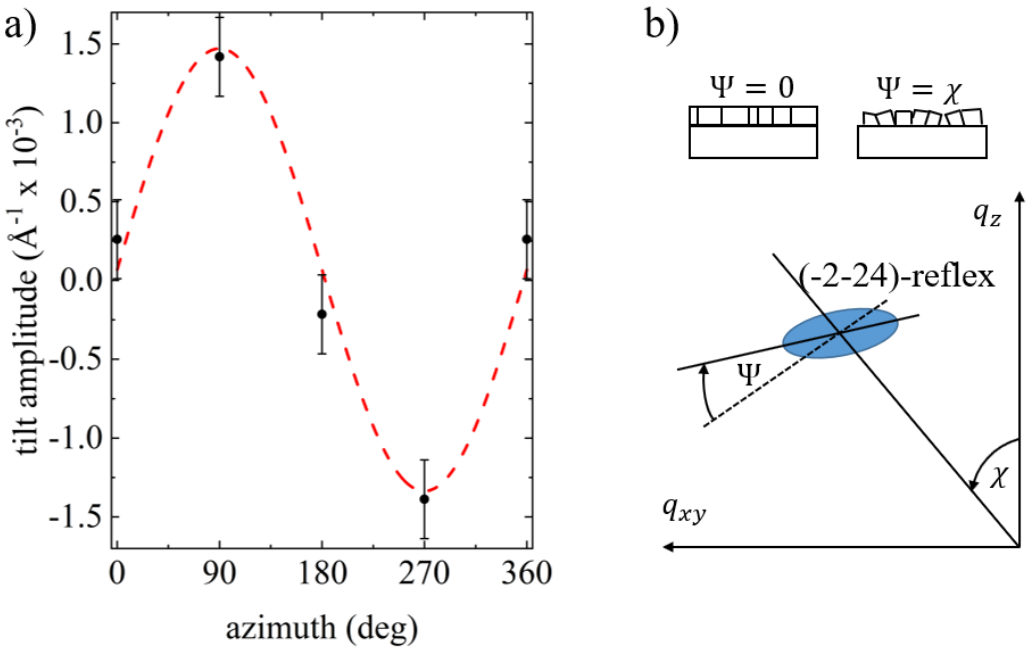

Figure 5.19: a) Film tilt derived from the (004)-RSMs of an $In_{0.13}Ga_{0.87}As$ film. b) Schematic sketch of the (-2-24)-$In_xGa_{1-x}As$ reflex ellipse rotation Ψ with respect to angle χ inclining the relaxation line towards the origin and the q_z direction. Evaluating Ψ serves to distinguish between ellipse broadening by finite crystallite size or crystallite tilt.

direction, which is in accordance with [36]. A variation of the rocking curve FWHM with azimuth indicates an imbalance in the dislocation populations on the type α and type β dislocation slip system (see chapter 2; in zincblende crystals, there are α and β {111} slip planes) [36]. The more homogeneous FWHM values of films grown on graphene covered GaAs indicate a more homogeneous relaxation pathway.

Additionally, the $In_{0.13}Ga_{0.87}As$ film grown on bare GaAs shown in figure 5.17b) and 5.18b), exhibits a considerable layer tilt Δq_{xy}, while no tilt is observed for films grown on graphene. Epitaxial tilt is well known in the GaAs system and is also attributed to the existence of different slip systems [1,3]. It is distinctive for mismatched material systems and has been observed in a more prominent fashion in $In_xGa_{1-x}As$ metamorphic buffer films grown on GaAs [1,3]. Tilt is caused by strain relieving dislocations, having a component

of their Burger's vectors normal to the growth plane [3]. Evaluating the tilt quantitatively, an oscillation tilt-azimuth angle behaviour is observed, as shown in figure 5.19a). In contrast, no tilt is observed for $In_{0.13}Ga_{0.87}As$ films grown on graphene covered GaAs, so there is no preferred slip system activation for film growth on graphene. The strain might be relaxed more homogeneously in a different way.

To gain further insight into the strain relaxation process, asymmetric RSMs were measured. Figure 5.20 and 5.21 shows the RSMs of the (-2-24)-reciprocal lattice reflex of an $In_{0.13}Ga_{0.87}As$ film grown on graphene covered GaAs and for comparison on bare GaAs for 0° and 90° azimuth rotation (this corresponds to measurements along the [110]- and [-110]-direction). The maximum film intensity is labelled by an arrow and is used to calculate the degree of film relaxation and indium concentration, see chapter 3. Note, the $In_{0.13}Ga_{0.87}As$ film peak position has been corrected by the layer tilt. In table 5.3, the values obtained by evaluating the (-2-24)-RSMs are summarised.

	on graphene		on bare GaAs	
	[110]	[-110]	[110]	[-110]
Ψ (°)	2 ± 1	3 ± 1	2 ± 1	2 ± 1
deg. of relaxation (%)	54 ± 2	45 ± 2	41 ± 2	10 ± 2

Table 5.3: Values obtained from the evaluation of the (004) and (-2-24)-RSMs of an 200 nm thick $In_{0.15}Ga_{0.85}As$ grown at 300°C.

The degree of film relaxation is considerably larger and more homogeneous for $In_{0.13}Ga_{0.87}As$ films grown on graphene compared to the values obtained for growth on bare GaAs. Probably, a strain relaxation mechanism with a lower activation threshold compared to the formation of defect is present, which results in a more enhanced relaxation on graphene. In [12] a film slip on the graphene surface relaxes the strain rather than introducing dislocations. Maybe, such a film slip is also observed for the growth of $In_xGa_{1-x}As$ films on graphene, especially for low indium concentrations. The energy required for a film slip on a featureless, i.e. defect free graphene surface is favourable compared to the introduction of dislocations [12], however, as shown in the last section, a considerable amount of defects is already

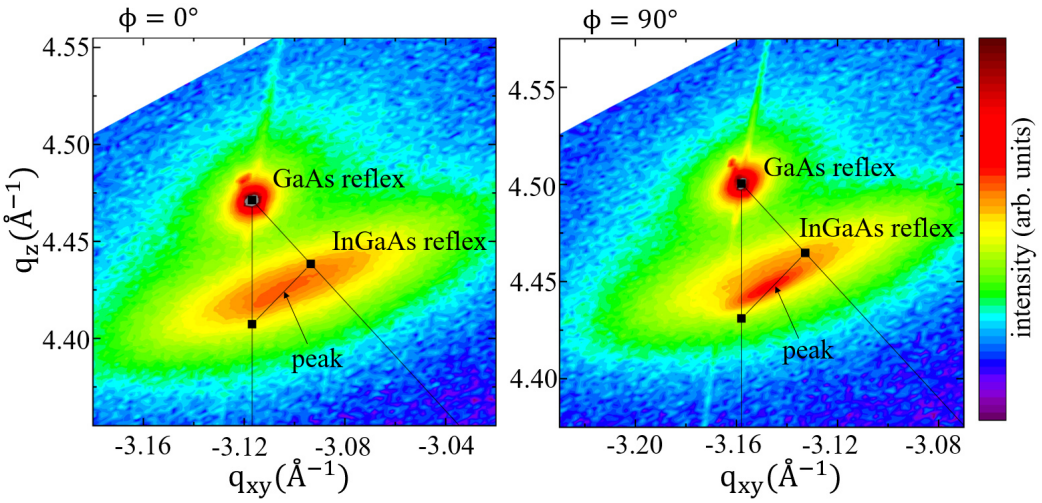

Figure 5.20: (-2-24)-RSMs of a $In_{0.13}Ga_{0.87}As$ films grown on graphene covered GaAs at 300°C for two different azimuth rotations.

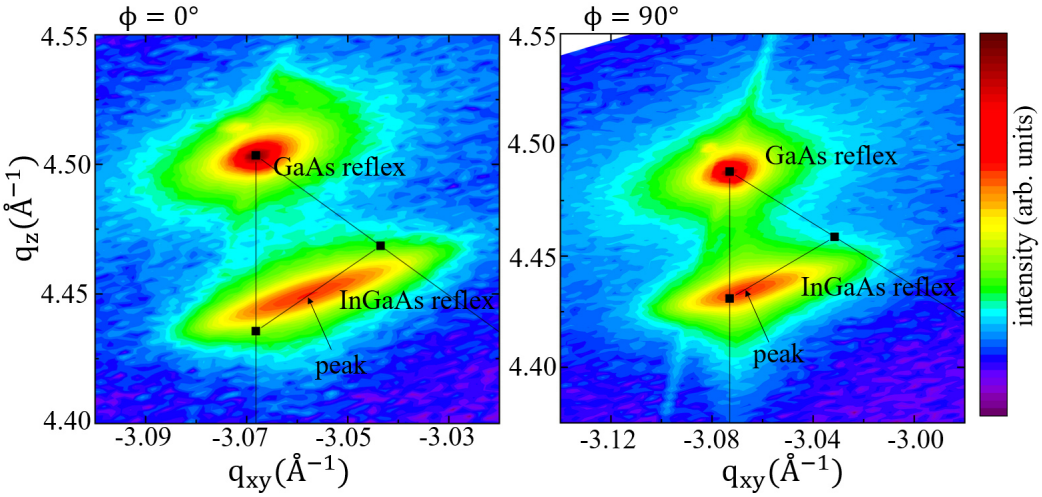

Figure 5.21: (-2-24)-RSMs of a $In_{0.13}Ga_{0.87}As$ films grown on bare GaAs at 300°C for two different azimuth rotations.

present in the film immediately after layer nucleation, far away from the critical thickness. Probably, the $In_xGa_{1-x}As$ films relax on the graphene surface in a mixed way: Partially by a film slip and partially by the introduction of defects or dislocations during film growth but also immediately after nucleation.

In agreement with the RSMs of the (004)-reciprocal lattice reflex, the intensity distribution of the (-2-24)-reciprocal lattice reflex is broader for film growth on graphene. Broadening of a reciprocal lattice point might originate from two different mechanisms. Firstly, a limited lateral coherence length of $In_xGa_{1-x}As$ crystallites also referred to as finite crystallite size broadening. Dislocations or stacking faults break the coherence within a single crystal layer and thus reduce the lateral correlation length. Secondly, the $In_xGa_{1-x}As$ film broadening due to crystal mosaicity. Slightly tilted or twisted individual crystallites break the coherence [64, 104]. Ellipse broadening by finite crystallite size or crystallite tilt is distinguished by the $In_xGa_{1-x}As$ reciprocal lattice reflex ellipse rotation Ψ, as sketched in figure 5.19b). Ψ is related to the angle χ, which inclines the relaxation line towards the origin and the q_z direction. $\Psi = 0°$ indicates dominant finite crystallite size broadening and $\Psi = \chi \approx 35°$ dominant tilt broadening. As reported in table 5.2, the $In_xGa_{1-x}As$ layers grown on graphene and on bare GaAs exhibit a similar value of $\Psi \approx (2 \pm 1)°$. Broadening of a reciprocal $In_{0.13}Ga_{0.87}As$ lattice point happens mainly due to a finite crystallite size corresponding to the presence of dislocations or stacking fault defects.

In the next step, the $In_xGa_{1-x}As$ films with larger indium concentration $x \leq 0.50$ already shown in figure 5.15d)-f) are analysed in the same way as the just presented of $In_{0.13}Ga_{0.87}As$ film. HRXRD measurements were performed and the degree of strain relaxation, the (004)-$In_xGa_{1-x}As$ reflex rocking-curve FWHM and the corresponding dislocation density were derived. Figure 5.22 depicts the plotted values as a function of the film's indium concentration. A reference GaAs film was grown on graphene covered GaAs and also analysed by HRXRD measurements. A FWHM of 0.16° was derived and added to figure 5.22a). This is probably the minimum FWHM/dislocation density obtained for film growth on the used graphene, as there is no perturbing strain

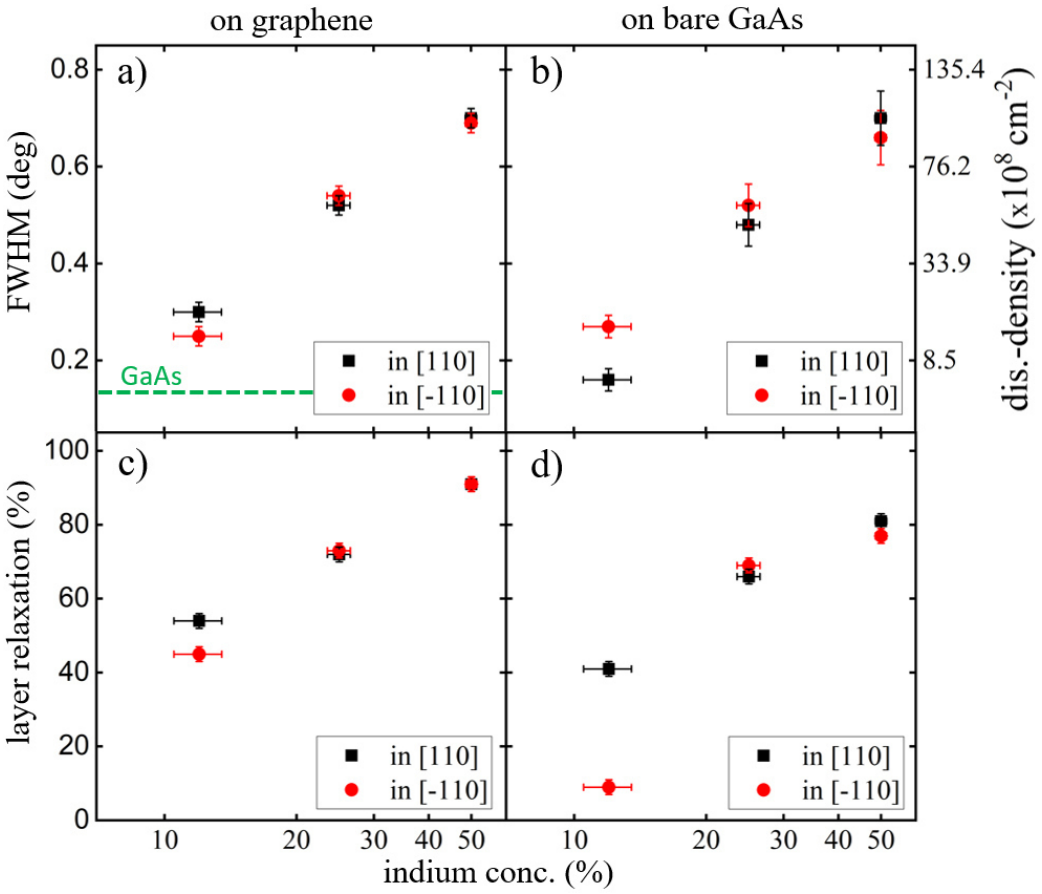

Figure 5.22: a)-b) (004)-$In_xGa_{1-x}As$ rocking curve FWHM with the corresponding dislocation density and c)-d) $In_xGa_{1-x}As$ film relaxation against the indium concentration for films grown on graphene covered GaAs and on bare GaAs at 300°C.

relaxation mechanism causing the formation of defects. The $In_xGa_{1-x}As$ film relaxation degree and the dislocation density increase for larger indium concentrations for both, films grown on bare GaAs and on graphene covered GaAs. The $In_xGa_{1-x}As$ films grown on graphene covered GaAs exhibit a larger degree of strain relaxation and a higher dislocation density in comparison to layers grown on bare GaAs. Films with larger indium concentrations exhibit larger mismatch to the GaAs substrate and thus a higher strain energy is built up during growth and the films relax stronger. The difference of the relaxation degree between films grown on graphene and on bare GaAs decreases

for larger indium concentrations. This is probably due to the enhanced relaxation of highly mismatched films. However, the $In_{0.50}Ga_{0.50}As$ film grown on graphene exhibit a larger degree of strain relaxation, but nearly the same dislocation density compared to the same film grown on bare GaAs. This indicates a stronger relaxation initialised by the graphene layer.

The largest difference in the degree of relaxation of roughly up to 44% (in the [-110]-direction) is observed for the $In_{0.13}Ga_{0.87}As$ film grown on bare GaAs and on graphene covered GaAs. Although there is no clear relation between the dislocation density and the degree of layer relaxation, the rather large difference in the degree of strain relaxation compared to a small change in the dislocation density may be related to a film slip on the graphene.

The results are confirmed by Raman-measurements reported in figure 5.23, performed by collaboration partner from the Otto-von-Guericke University in Magdeburg. The LO-wavenumber-shift ν of the GaAs related signal is plotted as a function of the indium concentration in figure 5.23a). For the $In_xGa_{1-x}As$ films grown on bare GaAs, ν is larger; this indicates less film relaxation [71, 105]. The LO-wavenumber-shift ν is converted into the de-

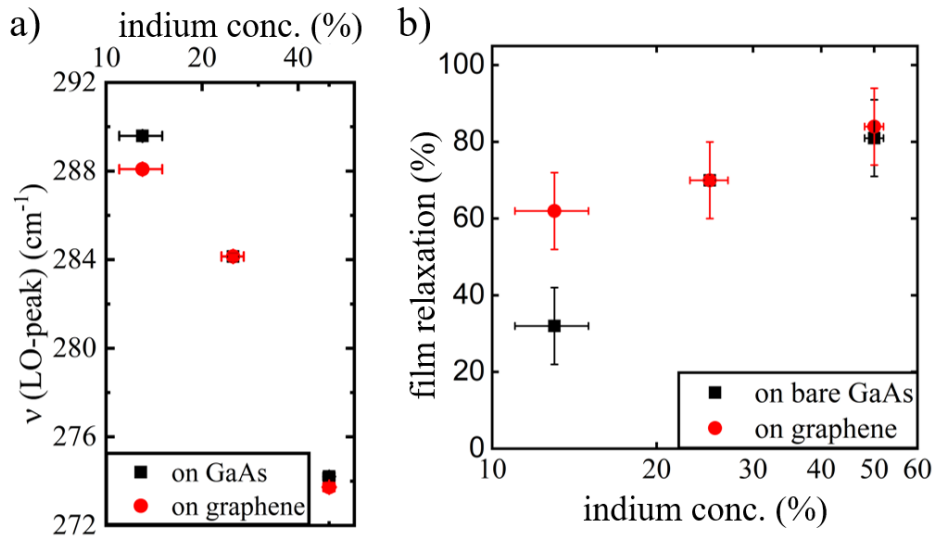

Figure 5.23: a) Measured GaAs related LO-phonon-shift of $In_xGa_{1-x}As$ films grown on graphene covered GaAs and bare GaAs at 300°C and b) the film's relaxation degree derived from the LO-phonon-shift.

gree of layer relaxation [71, 105]. The values are plotted against the indium concentration as shown in figure 5.23b) [71]). Similar relaxation degrees are obtained compared to the values derived from the HRXRD measurements. Note, that the values obtained by Raman-spectroscopy are not perceptive to the ⟨110⟩-directions, in contrast to the azimuth depended HRXRD measurements [71].

In summary, growth of $In_xGa_{1-x}As$ films ($0.13 \leq x \leq 0.70$) on graphene covered GaAs at a low temperature of 300° was performed. Single crystalline film growth was revealed. The $In_xGa_{1-x}As$ films grown on graphene are stronger relaxed in comparison to the films grown on bare GaAs for all investigated indium concentrations ($x \leq 0.50$). The strain relaxation difference between films grown on graphene and films grown on bare GaAs is largest for low indium concentrations of $x = (0.13 \pm 0.02)$. The absence of layer tilt, a more homogeneous but increased dislocation density and a larger degree of film relaxation points to a different strain relaxation mechanism for films grown on graphene covered GaAs compared to growth on bare GaAs.

5.3.2 Two-step $In_xGa_{1-x}As$ film growth

In this subsection, $In_xGa_{1-x}As$ film growth by a two-step growth approach is investigated. A two-step film growth has often been employed in literature for the growth on graphene and was motivated by the low deposited materials wettability on the graphene layer [4, 8, 10, 13]. Nucleation is initialised at low temperatures and then the sample is overgrown at growth temperatures usually employed for growth in the material system to enhance the crystal quality and to achieve a smooth surface. The nucleation layer provides incorporation sites for the material deposited at higher temperatures. The nuclei density should be large to provide sufficient incorporation sites and the nuclei should be defect free. Overgrowth is usually performed at elevated temperatures as a higher adatom mobility and therefore a higher mean-free-path is favourable for high quality material growth.

A two-step growth process applied to the growth of $In_xGa_{1-x}As$ films on graphene covered GaAs is described in the following. Several growth schemes

were tested. The goal of the two-step growth process on the one hand is to enhance the $In_xGa_{1-x}As$ film strain relaxation, while on the other hand to reduce the dislocation density within the film. The growth of thick $In_xGa_{1-x}As$ films was optimised by varying the nucleation layer thickness and the substrate temperature. The surface morphology is investigated by AFM measurements and the crystallographic structure is analysed by HRXRD measurements and Raman spectroscopy analogues to the previously presented characterisation of $In_xGa_{1-x}As$ films grown by the one-step growth process at 300°C.

First, the influence of the $In_xGa_{1-x}As$ nucleation layer thickness on the surface morphology and the crystallographic properties of thicker $In_xGa_{1-x}As$ films was investigated. In principle, two cases can be distinguished: The nuclei cover the graphene surface completely, as it was exemplary shown in the SEM image in figure 5.9c) for nominal coverages of $\geq$ 5 nm, and second, the nuclei cover only a part of the graphene surface, which was exemplary shown in the SEM image in figure 5.9a) for nominal coverages of $\leq$ 2 nm. In the first case, a defective nucleation layer was revealed by TEM images (see figure 5.12) after nuclei coalescence, while in the second case, a higher growth temperature could lead to a smoother film with fewer crystal defects, because of a higher adatom's mean-free-path and thud preferentially incorporation at existing nuclei before nuclei coalescence.

Growth of $In_{0.12}Ga_{0.88}As$ nucleation layers with different thickness and subsequent overgrowth at 385°C was tested. The total $In_{0.12}Ga_{0.88}As$ film thickness was constantly kept at 200 nm. Growth was performed at 1 $Å s^{-1}$ and an As_4 pressure of 0.9×10^{-5} mbar for nucleation and up to 2.2×10^{-5} mbar for overgrowth at 385°C. For individual detailed growth parameters, please refer to the growth sheets in the appendix.

Figure 5.24 shows the AFM images of three 200 nm thick $In_{0.12}Ga_{0.88}As$ films with 0.5 nm, 15 nm and 100 nm thick nucleation layer grown at 300°C and subsequent overgrowth at 385°C. The corresponding surface roughnesses are listed in table 5.4.

The surface roughness slightly increases for thinner nucleation layers. However, growth of a 100 nm thick nucleation layer and subsequent over-

nucleation layer thickness	surface roughness
0.5 nm	(1.0 ± 0.1) nm
5 nm	(0.8 ± 0.1) nm
100 nm	(0.7 ± 0.1) nm

Table 5.4: Surface roughness obtained from the evaluation of the AFM measurements of 200 nm thick $In_{0.12}Ga_{0.88}As$ films grown by a two-step growth approach with different nucleation layer thicknesses.

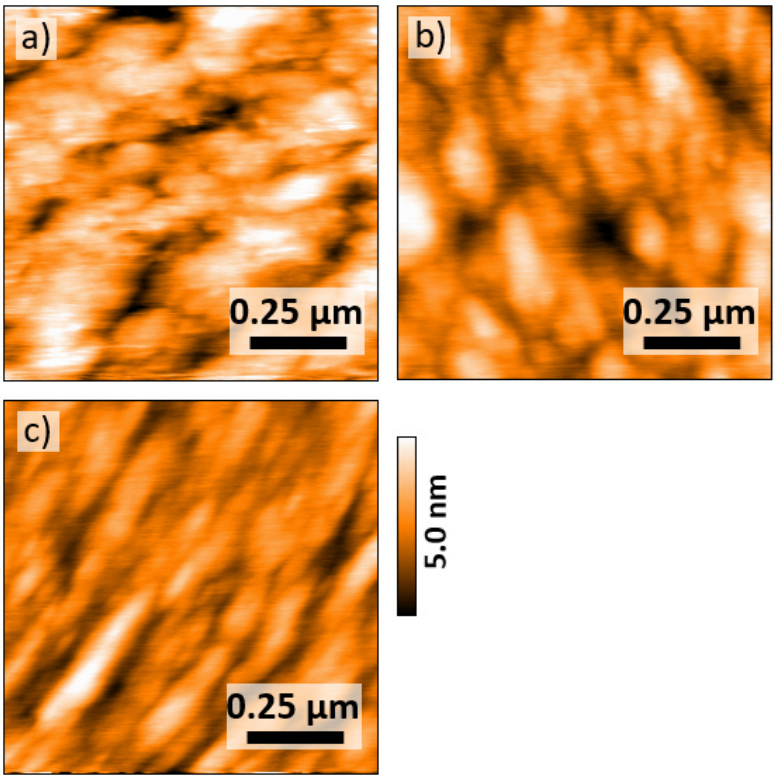

Figure 5.24: 200 nm thick $In_{0.12}Ga_{0.88}As$ film grown with different nucleation layer thicknesses: (a) 0.5 nm at 300°C plus 199.5 nm at 385°C, b) 15 nm at 300°C plus 185 nm at 385°C, c) 100 nm at 300°C plus 100 nm at 385°C.

growth causes a surface structure of elongated islands along the ⟨110⟩ directions; see figure 5.24c). Such a pattern is neither observed in a) nor in b) nor for the 200 nm thick $In_{0.13}Ga_{0.87}As$ film grown by the one-step growth at 300°C. Such elongated islands may indicate anisotropic Ga or In diffusion on the surface [106]. It is unclear, why this effect is most prominent for the

films with 100 nm thick nucleation layer.

Another interesting result is, that the 200 nm $In_{0.12}Ga_{0.88}As$ film surface is rather flat for nucleation layers with a nominal coverage of 0.5 nm. Although it was shown in the SEM image in figure 5.9a), that with nominal coverage, only some small widely spread nuclei are distributed over the wafer, a smooth film is formed after overgrowth. In contrast, growing the same film immediately at elevated temperatures, i.e. without the low temperature nucleation layer, results in an extremely rough and polycrystalline $In_{0.12}Ga_{0.88}As$ film. The small nuclei stabilise the film growth as they provide incorporation sites for the deposited atoms at elevated temperature. Small nuclei already grown at low temperature are also stable at elevated temperature, as already discussed in section 5.2. The substrate-graphene-nuclei interaction stabilises the nuclei and barely any ripening occurs. The results clearly show the necessity of a low temperature nucleation step for the remote heteroepitaxial growth of $In_xGa_{1-x}As$ films on graphene covered GaAs, similar to [10, 13].

Overgrowth of small $In_xGa_{1-x}As$ nuclei is further investigated for higher indium concentrations. Layers with $x = (0.30 \pm 0.02)$ and $x = (0.41 \pm 0.02)$ indium fraction were grown. Related to the prior presented results, the following growth scheme was selected: 0.5 nm $In_xGa_{1-x}As$ was deposited at 300°C and overgrown by 199.5 nm at 385°C. The corresponding AFM measurements of the sample surface are shown in figure 5.25 and the surface roughness is given in table 5.5.

indium concentration	surface roughness
$x = 0.12$	(1.0 ± 0.1) nm
$x = 0.30$	(1.4 ± 0.1) nm
$x = 0.41$	(1.9 ± 0.1) nm

Table 5.5: Surface roughness obtained from the evaluation of the AFM measurements of 200 nm thick $In_xGa_{1-x}As$ films grown by a two-step growth approach with 0.5 nm nucleation layer thickness.

A larger indium concentration leads to a rougher surface. Above $x > 0.12$, some deep valleys are observed on the $In_xGa_{1-x}As$ film surface. A higher indium concentration leads to more mobile adatoms and may causes the growth

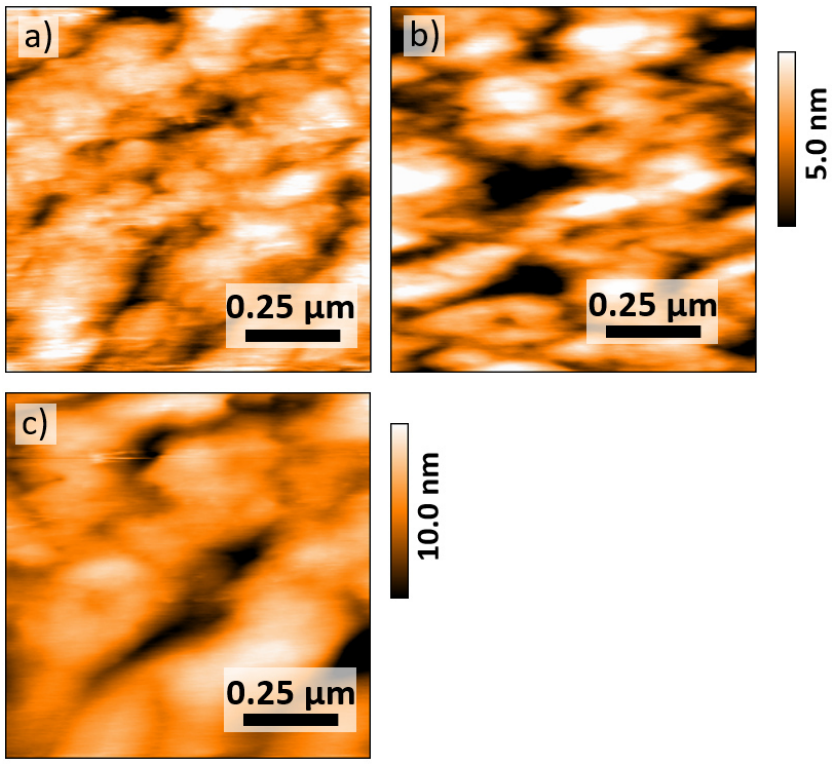

Figure 5.25: 200 nm thick $In_xGa_{1-x}As$ films grown by a two-step approach: a) $x = 0.12 \pm 0.02$, b) $x = 0.30 \pm 0.02$ and c) $x = 0.41 \pm 0.02$.

of larger islands instead of a smooth film surface. The sample roughness is comparable to the samples grown by the one-step approach at 300°C, although the smoothest surfaces are observed for samples grown by the one-step growth approach.

HRXRD measurements and Raman-spectroscopy were performed on these samples to investigate the strain relaxation mechanism and derive the defect densities, in the same way as in the last subsection. (004)- and (-2-24)-RSMs of the GaAs and $In_xGa_{1-x}As$ reciprocal lattice reflex were measured for differing azimuth rotations. The derived (004)-rocking curve FWHM, the corresponding dislocation density and the degree of strain relaxation calculated from the asymmetric (-2-24)-reciprocal lattice reflex are shown in figure 5.26.

$In_xGa_{1-x}As$ films grown on graphene covered GaAs exhibit larger degree of strain relaxation compared to films grown on bare GaAs. The relaxation is

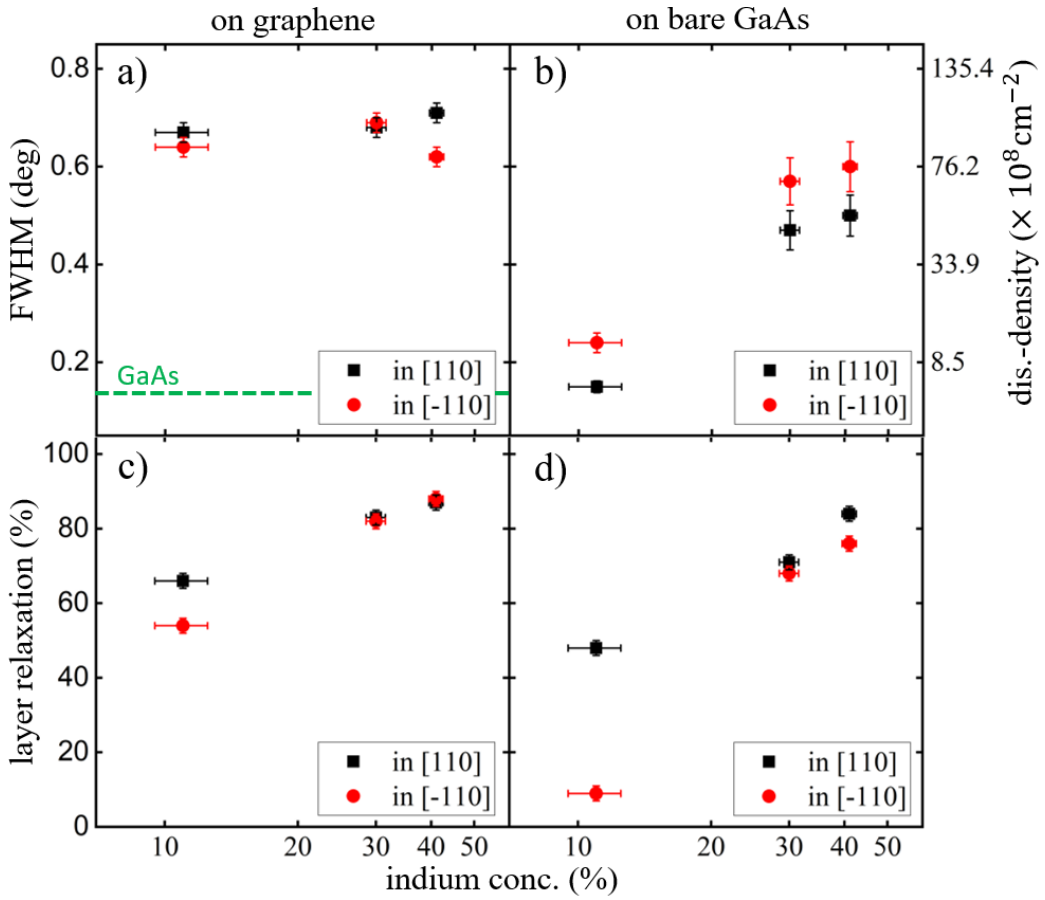

Figure 5.26: a)-b) (004)-$In_xGa_{1-x}As$ rocking curve FWHM with the corresponding dislocation density and c)-d) $In_xGa_{1-x}As$ film relaxation against the indium concentration for films grown on graphene covered GaAs and on bare GaAs by a two step growth process. 300°C.

more homogeneous on the graphene layer, especially for low indium concentration. The relaxation degrees are also larger compared to the films grown by the one-step approach. For example, the $In_{0.12}Ga_{0.88}As$ film grown by the one-step approach is relaxed to $\approx 55\%$ (measured along the [110]-direction, see figure 5.22), while the $In_{0.13}Ga_{0.87}As$ film grown by the two-step approach is relaxed to $\approx 65\%$. Higher temperature overgrowth leads to larger degree of strain relaxation. In contrast, the $In_xGa_{1-x}As$ films grown on bare GaAs for both growth approaches exhibit nearly the same relaxation degree and they are stronger relaxed in the [110] direction.

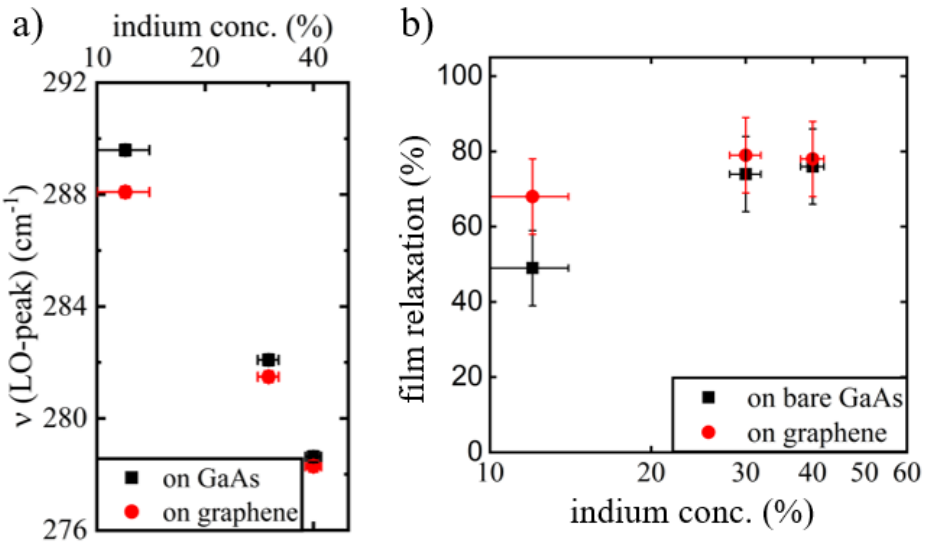

Figure 5.27: a) Measured GaAs related LO-phonon-shift of the InGaAs layers. b) derived degree of relaxation derived from the LO-phonon-shift.

The results are confirmed by Raman-measurements reported in figure 5.27a). The LO-wavenumber-shift ν of the GaAs related signal is plotted as a function of the indium concentration. For the $In_xGa_{1-x}As$ films grown on bare GaAs, ν is larger, indicating a less relaxed film [71, 105]. The degree of film relaxation is extracted from the LO-wavenumber-shift ν and plotted in figure 5.23b) [71]. Similar relaxation degrees are obtained by this method, comparable to values derived from the HRXRD measurements.

The HRXRD (004)-rocking curve FWHM of the $In_xGa_{1-x}As$ film was derived and the corresponding dislocation density was calculated, see figure 5.26a). A mostly constant trend and no relation to the indium concentration is observed for films grown on graphene. This is a surprising result and contrasts the behaviour observed for the one-step growth.

Broadening of the (004)-rocking curve is related to crystallites mosaicity and a limited lateral crystallite correlation length, as already discussed in the last section. While both broadening mechanism overlap for the (004)-reciprocal lattice reflex, the can be distinguished for the (-2-24)-reciprocal lattice reflex by quantitative investigation of the ellipse rotation Ψ. A schematic sketch has already been presented in figure 5.19. It is focused on the

$In_{0.12}Ga_{0.88}As$ film in the following. Films grown by the two-step approach on bare GaAs exhibit $\Psi \approx (2 \pm 1)^\circ$ and equal values are obtained for measurements along the [110]- and [-110]-direction. Similar values were also obtained for $In_{0.13}Ga_{0.87}As$ films grown by the one-step approach at 300°C on bare GaAs and also on graphene covered GaAs. Such Ψ values are related to broadening by dislocations introduced to relax the strain. In contrast, $In_{0.12}Ga_{0.88}As$ films grown by the two-step approach on graphene covered GaAs exhibit a value of $\Psi \approx (13 \pm 1)^\circ$ for measurements in both directions, indicating FWHM broadening due to a partially mosaic film. The crystallite mosaicity is probably not related to the lattice mismatch and thus to the indium concentration, but rather to the growth mechanism. The nucleation film overgrowth at elevated temperature probably favours the formation of slightly twisted or tilted crystallites. After low temperature nucleation, the nuclei may grow larger at elevated temperatures rather than quickly coalescent. Further investigations on the initial growth stage are necessary. The larger defect density and film mosaicity observed for films grown by a two-step approach are in contrast to results reported in literature. Often a two-step growth results in smooth films. However, a larger $In_xGa_{1-x}As$ film relaxation degree is observed for growth on graphene covered GaAs.

Cross-section TEM images of a GaAs-graphene-$In_{0.17}Ga_{0.83}As$ stack, provided by collaboration partners from the University of Warwick, are depicted in figure 5.28. The Dark-field image in figure 5.28a) reveals a defective $In_{0.17}Ga_{0.83}As$ film with several dislocation lines in the GaAs film. A close-up image in figure 5.28b) indicates the crystalline film growth. The $In_{0.17}Ga_{0.83}As$ film exhibits the same crystallographic orientation as the substrate. A wavy GaAs-graphene-$In_{0.17}Ga_{0.83}As$ interface is depicted, confirming that the GaAs-graphene surface is non-flat as it is always assumed in a simple figure of merit. A non-flat surface modulates the leaking substrate potential and lead to varying surface conditions on the graphene layer. This probably has large influence on the growth microscopic growth conditions. A SiO_x particle located on the graphene surface and overgrown by $In_{0.17}Ga_{0.83}As$ is depicted in figure 5.28b). [78,79,81] report on the deposition of SiO_x nanoparticles on graphene during the graphene CVD-growth process,

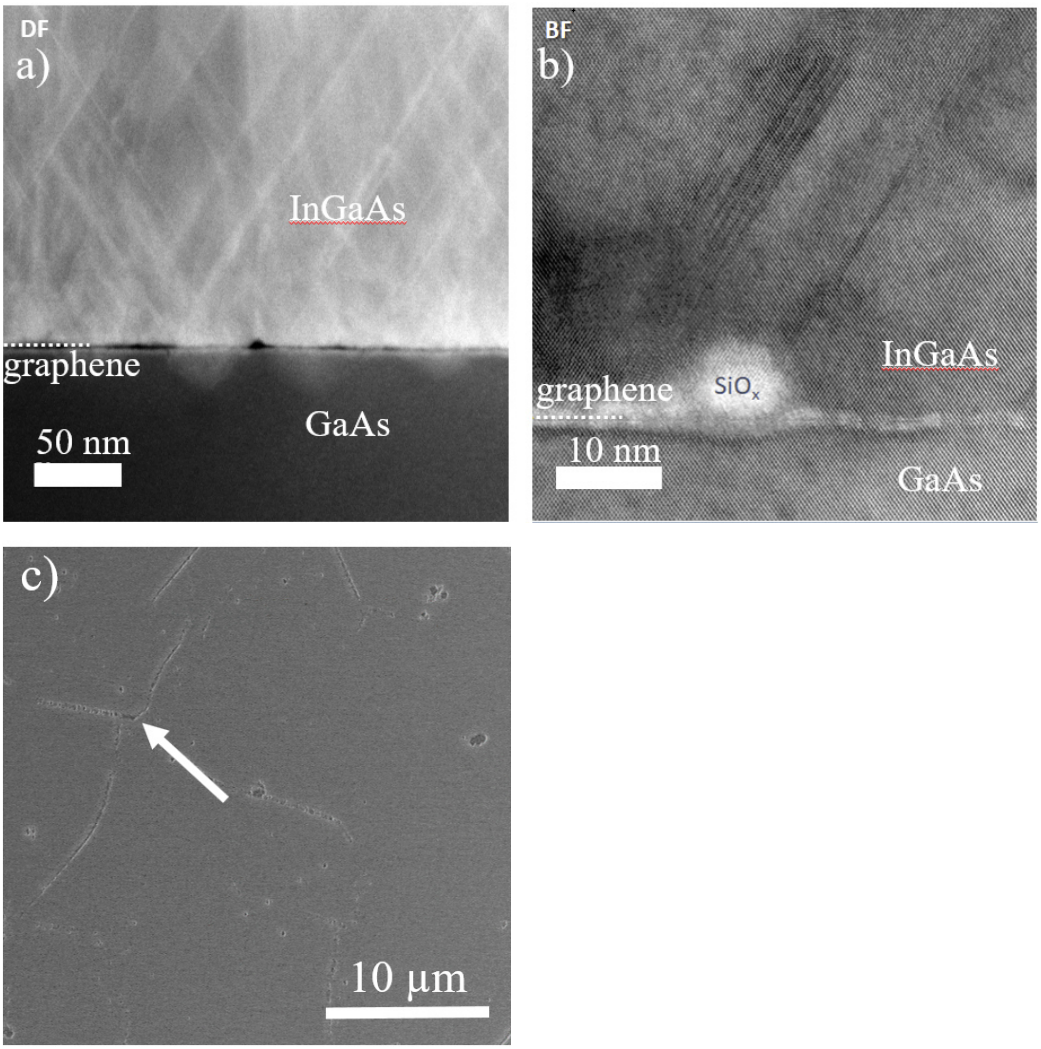

Figure 5.28: a) Dark-field cross section TEM image of an GaAs-graphene-$In_{0.17}Ga_{0.83}As$ stack. Bright lines along the {111} planes reveal a high dislocation density in the film. b) Bright-field cross section STEM image of an GaAs-graphene-$In_{0.17}Ga_{0.83}As$ stack showing a SiO_x particle on the surface. The fine contrast difference within the wavy bright interface might indicate the graphene layer. c) Large area SEM image of an $In_{0.17}Ga_{0.83}As$ layer grown on graphene. Surface features marked by an arrow reveal defective graphene.

but also during plasma cleaning. The particles may introduce stacking fault defects in the layer. Enhanced plasma cleaning could be tested in further experiment [78]. Figure 5.28c) shows the SEM image of the $In_{0.17}Ga_{0.83}As$ film surface after growth. Some cracks pertubate the film's surface, indicating

growth on folded, wrinkled or otherwise defective graphene.

In summary, in this section, the growth of 200 nm thick $In_xGa_{1-x}As$ films by a two-step approach was discussed. The sample surface is slightly rougher compared to $In_xGa_{1-x}As$ films grown on graphene by a one-step growth approach at 300°C. The film's degree of relaxation is slightly larger compared to those obtained from films grown by the one-step process. Surprisingly, the $In_xGa_{1-x}As$ films exhibit a constant dislocation/defect density independent on the indium concentration. The films exhibit larger crystalline mosaicity which is probably caused by the nucleation layer overgrowth a elevated temperature.

5.3.3 $In_xGa_{1-x}As$ thickness variation

So far, the growth and characterisation of 200 nm thick $In_xGa_{1-x}As$ film was discussed. In this section, the $In_xGa_{1-x}As$ film thickness is varied to gain more insight into the strain relaxation mechanism during the initial stage of film growth. $In_xGa_{1-x}As$ films grown on bare GaAs relax the strain by forming dislocations, when the built-up strain energy exceeds a critical film thickness. There are several models, mentioned in chapter 2, which describe the critical thickness, for example, the model from People and Bean [107]. Figure 5.29 shows the calculated critical film thickness as a function of the indium concentration for an $In_xGa_{1-x}As$ layer grown on a GaAs substrate. Larger indium fractions and therefore larger lattice mismatch lead to a smaller critical thickness. Dislocations are introduced into the film, above the critical thickness, as already discussed in the last two subsections. A deviation from a fixed critical thickness is often observed when growth is far from equilibrium [32–34]. For growth on graphene, a different strain relaxation model was proposed in [12]. Films grown on graphene by the influence of the substrate can slip over the graphene surface to relax the built-up strain energy. The energy of such a film slip on graphene covered GaAs was calculated by [12] to around 37 mJm^{-2}. Putting this energy into equation (2.10) results in the critical thickness for a film slip on the graphene surface, see equation (2.9). Figure 5.29 shows the calculated critical $In_xGa_{1-x}As$ film

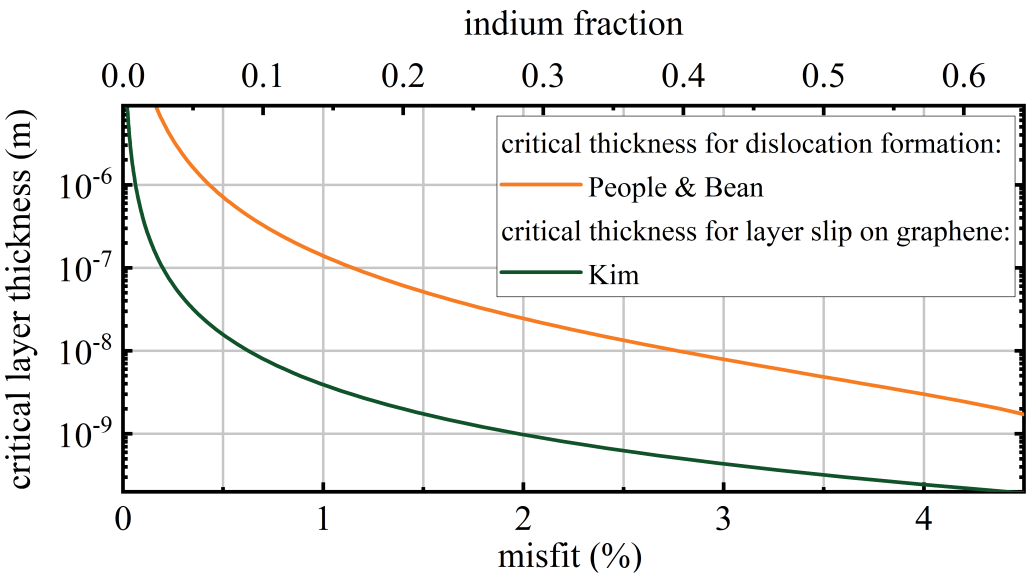

Figure 5.29: Critical $In_xGa_{1-x}As$ film thickness for the introduction of dislocations and for a film slip on GaAs. Relaxation models from [107] and [12].

thickness for a film slip on the graphene as a function of the indium fraction. This critical thickness is significantly smaller compared to the critical thickness before introducing dislocation.

The 200 nm thick $In_xGa_{1-x}As$ films ($0.15 < x \leq 0.50$) grown on graphene exceed both critical thicknesses, so the up-build strain energy relaxes either by the introduction of dislocations or by film slip over the graphene as discussed in the last two subsections. To distinguish between both relaxation behaviours, thinner $In_xGa_{1-x}As$ films were grown, i.e. a 30 nm thick $In_{0.15}Ga_{0.85}As$ film and a 15 nm thick $In_{0.30}Ga_{0.70}As$ film. The film thickness is between the critical thickness of dislocation formation and the critical thickness of film slip on graphene. The signal-to-noise ratio of our measurement techniques, i.e. Raman-spectroscopy and HRXRD, is not sufficient to analyse films < 15 nm. To achieve a stronger signal in the used HRXRD-set-up, the geometry was changed. Instead of measuring the (-2-24)-reciprocal lattice reflex, the (224)-reciprocal-lattice reflex is investigated. As described in chapter 3, the measured intensity is larger in this configuration, but also the resolution decreases. Figure 5.30 shows an exemplary measured (224)-RSM of a 30 nm thick $In_{0.15}Ga_{0.85}As$ film grown on graphene. Contour lines were

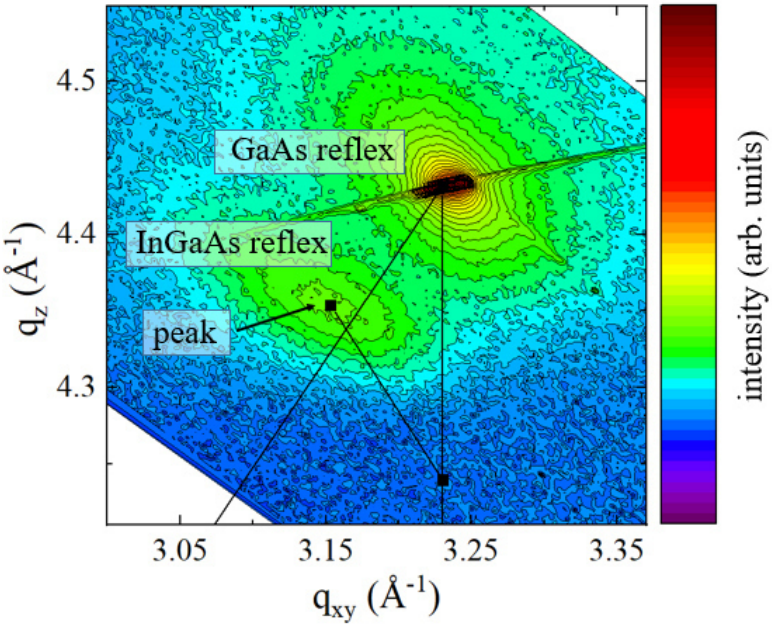

Figure 5.30: (224)-RSM of a 30 nm thick $In_{0.15}Ga_{0.85}As$ film grown on graphene covered GaAs.

added to identify the maximum film peak intensity. The $In_{0.15}Ga_{0.85}As$ reflex peak is outside of the relaxation triangle leading to the conclusion, that the film relaxation is 110%. This contradicts the physically possible maximum relaxation of 100%, as then the film lattice entirely matches the substrate lattice. A possible explanation is a tensile strained layer, which exhibits a larger lattice constant with respect to the substrate lattice constant.

A similar behaviour was observed for island zipping in literature [101–103] as already discussed above. Maybe the tensile strain in the thin $In_xGa_{1-x}As$ films results from zipped island during nucleation. A more quantitative investigation of the thin film relaxation degree was performed. An overview is given in table 5.6 and 5.7. The sample set was split, due to the long measurement integration times. In table 5.6, samples grown by the one-step approach at 300°C and investigated by Raman-spectroscopy are shown. In table 5.7, samples grown by the two-step approach (layer nucleation at 300° and overgrowth at 385°) and investigated by HRXRD measurements are shown. Although both measurement techniques are different, it was already shown

in figure 5.22,5.23 and 5.26,5.27, that they supply similar film relaxation degrees.

		degree of relaxation	
indium conc.	film thick.	on bare GaAs	on graphene
$\approx 15\%$	30 nm:	0 ± 10	110 ± 10
	200 nm:	32 ± 2	62 ± 2
$\approx 30\%$	15 nm:	27 ± 10	120 ± 10
	200 nm:	70 ± 2	70 ± 2

Table 5.6: Relaxation degree derived from Raman-spectroscopy of different $In_xGa_{1-x}As$ films with different film thickness grown at 300°C.

		degree of relaxation			
		on bare GaAs		on graphene	
indium conc.	film thick.	[110]	[-110]	[110]	[-110]
$\approx 15\%$	30 nm:	0 ± 2	0 ± 2	80 ± 5	80 ± 5
	200 nm:	48 ± 2	9 ± 2	66 ± 2	54 ± 2
$\approx 30\%$	15 nm:	49 ± 5	0 ± 2	69 ± 5	66 ± 5
	200 nm:	71 ± 2	68 ± 2	83 ± 2	82 ± 2

Table 5.7: Relaxation degree derived from HRXRD measurements of different $In_xGa_{1-x}As$ films with different film thickness grown by the two-step approach. Layer nucleation was performed at 300°C and overgrowth at 385°C.

First, the $In_xGa_{1-x}As$ films grown by the one-step approach are considered. The $In_xGa_{1-x}As$ films grown on the graphene covered GaAs exhibit a degree of relaxation of $(110 \pm 10)\%$ for $x = 0.15 \pm 0.05$ and of $(120 \pm 10)\%$ for $x = 0.30 \pm 0.05$. These large values can be attributed to a partially tensile strained $In_xGa_{1-x}As$ film, rather than to a real relaxation degree. In contrast, for both $In_xGa_{1-x}As$ films grown on bare GaAs, the degree of film relaxation is considerably smaller. The $In_{0.15}Ga_{0.85}As$ film is completely pseudomorphic and the $In_{0.30}Ga_{0.70}As$ film is relaxed to $(27 \pm 10)\%$. This behaviour is expected with respect to the critical layer thickness shown in figure 5.29. The degree of film relaxation of similarly grown 200 nm thick $In_xGa_{1-x}As$ films is *as expected*.

Next, $In_xGa_{1-x}As$ films grown by the two-step approach are considered. Related to the growth of the 200 nm thick $In_xGa_{1-x}As$ films, the growth of

thinner samples was performed by depositing a 0.5 nm thin $In_xGa_{1-x}As$ nucleation layer at 300°C and subsequent overgrowth at 385°C. The relaxation degree was determined from RSMs of the (224)-reciprocal-lattice reflex. The values are shown in table 5.7. Distinguishing between relaxation in [110]- and [-110]-direction is possible. Thin $In_xGa_{1-x}As$ films grown on bare GaAs exhibit similar values compared to films grown by the one-step approach. Both are only relaxed to a small degree. The 30 nm thick $In_{0.15}Ga_{0.85}As$ film is completely pseudomorphic. The 15 nm thick $In_{0.30}Ga_{0.70}As$ film is pseudomorpic in the [-110]-direction and $(49 \pm 5)\%$ partially relaxed in the [110]-direction. In contrast, thin $In_xGa_{1-x}As$ films grown on graphene covered GaAs are relaxed to a larger degree in agreement with values obtained for the one-step approach. Obviously, the relaxation degree is different for both growth mechanism for films grown on graphene covered GaAs, so the relaxation degree depends on the growth temperature.

As discussed in chapter 2 strain usually builds-up successively during film growth and starts at some point to relax. The strain relaxation degree increases monotone with the film thickness. This behaviour was is not observed for films grown on graphene covered GaAs. In the following paragraph possible reasons for the large relaxation degree of thin films are discussed; the film slip on the graphene surface, and the introduction of tensile strain during the initial stage of growth.

As shown above, the nucleation islands start to coalescence at a thickness of roughly 5 nm. The critical thickness for a layer slip plotted in figure 5.29 is calculated to approximately ≤ 4 nm for $In_xGa_{1-x}As$ films with $x \geq 0.15$. So, the nuclei might relax portion of their strain, by a slip, even before the a closed film is grown. Depositing more material increases the island density or size. At a certain surface coverage, relaxed islands may zip as proposed above, to reduce the surface energy. This applies tensile strain to the islands and would explain the observed high relaxations degree up to $(120 \pm 10)\%$. Stacking faults and dislocations are introduced at the nuclei impingement points [101, 102]. These were already observed immediately after island coalescence in the TEM images (see figure 5.12b)), far below the critical thickness for the introduction of dislocations. Subsequent overgrowth

reduces the tensile strain introduced by island zipping as on the one hand side, the surface coalescents, so the surface tension is reduced, and on the other hand, compressive strain builds-up during growth and compensates the tensile strain. Note, that the smoothest surfaces were observed for 200 nm thick films. With increasing film thickness, the compressive strain becomes increasingly prominent and closed film may relax by a film slip over the graphene surface. These considerations would explain the larger degree of film relaxation, observed for 200 nm thick $In_xGa_{1-x}As$ films.

The temperature also may play an important role in the relaxation process. Overgrowth of small nuclei at elevated temperature causes the existing nuclei growth rather then the formation of new nuclei on the graphene surface. This results in a larger island size as exemplary shown in figure 5.31 for 15 nm $In_{0.30}Ga_{0.70}As$ deposited by the single- and by the two-step process on graphene covered GaAs. Both samples exhibit a similar surface roughness of $\sigma = (3.0 \pm 0.1)$ nm, but the surface morphology looks different. The film grown by the one-step approach exhibits smaller islands compared to the film grown by the two-step approach. The corresponding relaxation degrees, see table 5.6 and 5.7, indicate less a less tensile strained film grown by the two-step approach. The reason is unclear, but may be due to less pronounced island zipping or due to a stronger tensile strain relaxation by the introduction of defects at elevated temperature. Both mechanism mainly dependent on the overgrowth temperature rather then the lattice mismatch or the indium concentration and would explain the constant dislocation density observed in the last subsection for 200 nm thick $In_xGa_{1-x}As$ films grown by the two-step approach.

In summary, 15 nm and 30 nm thick $In_xGa_{1-x}As$ films were grown on graphene covered GaAs and on bare GaAs for comparison. The films were investigated by HRXRD measurements and Raman-spectroscopy. Films grown on graphene exhibit an uncommonly large relaxation degree (above 100%), indicating a tensile strained film. It was speculated, that the nucleation of the $In_xGa_{1-x}As$ films applies tensile strain due to island zipping. This can be addressed by further investigation on the initial $In_xGa_{1-x}As$ nucleation layer grown on graphene covered GaAs. A suggestion is to perform STEM

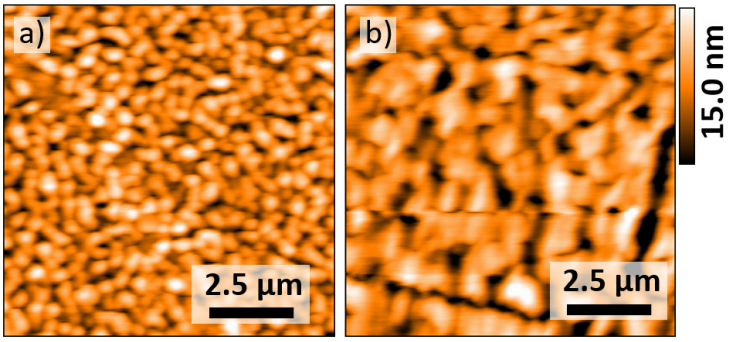

Figure 5.31: AFM image of two 15 nm thick $In_{0.30}Ga_{0.70}As$ films. a) grown by a one-step approach and b) grown by a two-step-approach, respectively

investigations of the nuclei and perform subsequent analysis of the atomic distances to analyse the relaxation degree.

Chapter 6

Conclusion and Outlook

To summarise this dissertation, remote heteroepitaxy growth of $In_xGa_{1-x}As$ films ($0 < x \leq 0.5$) by molecular beam epitaxy on transfer graphene covered GaAs-(001) substrates was investigated for the first time.

First, several cleaning approaches to remove PMMA residuals from the graphene surface and GaAs surface oxides between the GaAs substrate and the graphene layer were tested. It was shown, that thermal annealing up to 620°C is not sufficient, to remove all polymer residuals and GaAs oxides. Instead, a carefully optimised H+Ar-plasma treatment with subsequent thermal annealing in UHV was performed. XPS- and Raman-spectra reveal the PMMA residual and GaAs oxide removal by the plasma treatment while keeping the graphene mainly intact. The XPS measurements further reveal, that the graphene protects the GaAs from re-oxidation in air. The developed process allows the use of wet transferred CVD-graphene for the remote heteroepitaxial growth of $In_xGa_{1-x}As$ films. This was verified by depositing and analysing $In_xGa_{1-x}As$ nuclei on graphene-covered GaAs. SEM images of the surface showed small nuclei on the monolayer graphene grown under the substrate-film interaction, while at edge regions of the graphene a high density of large nuclei is visible, and typical deoxidation holes can be seen on the bare GaAs. Detailed investigation on the nucleation was carried out. The influence of temperature and indium concentration on nucleation behaviour was discussed. While at low temperatures of about 300°C and low indium

concentration of around 15% the most homogeneous surface coverage was observed, at higher temperatures and indium concentrations above $x > 0.5$, larger nuclei are visible and an incomplete surface coverage is revealed. TEM studies on selected $In_{0.15}Ga_{0.85}As$ nuclei showed, that the nuclei are defect-free before coalescence, but defects are observed afterwards. Island zipping or the $In_xGa_{1-x}As$ nucleation on graphene pinholes were discussed as reasons, but further investigations are necessary. STM or STEM measurements of the graphene surface and the nuclei are suggested to reveal the mechanism of defect introduction.

Next, the nuclei were overgrown with thicker $In_xGa_{1-x}As$ films ($0.13 \leq x \leq 0.7$) at 300°C. The surface of the films grown on graphene-covered GaAs was analysed by AFM. Thicker films are smoothest. 200 nm thick $In_{0.13}Ga_{0.87}As$ films exhibit a surface roughness of (1.0 ± 0.1) nm. The films exhibit the (001)-orientation, the same orientation as the GaAs-(001) substrate, which was revealed by ω-2θ-scans along the symmetric reflexes. This clearly indicates a substrate-graphene-InGaAs interaction and thus successful remote epitaxy. Detailed RSMs of the (004)- and (-2-24)-reciprocal lattice reflexes were measured for different azimuth angles. From these measurements, the degree of relaxation and the dislocation density of the $In_xGa_{1-x}As$ films were derived. HRXRD measurements were exemplified on an $In_{0.13}Ga_{0.87}As$ film grown on graphene covered GaAs and grown on bare GaAs for comparison. The $In_xGa_{1-x}As$ films grown on graphene are stronger relaxed in comparison to the films grown on bare GaAs over the entire investigated indium concentration range up to $x = 0.50$. The strain relaxation difference between films grown on graphene and films grown on bare GaAs is largest for low indium concentrations of $x = 0.13$. Absence of layer tilt, a more homogeneous dislocation density and a larger degree of film relaxation point to a different strain relaxation mechanism for films grown on graphene covered GaAs compared to growth on bare GaAs.

The growth of 200 nm thick $In_xGa_{1-x}As$ films by a two-step approach was discussed in relation to reports in the literature. The sample surface is slightly rougher compared to $In_xGa_{1-x}As$ films grown on graphene covered GaAs by a one-step growth at 300°C. The film's degree of relaxation is lar-

ger compared to similar films grown by the one-step approach. However, the $In_xGa_{1-x}As$ films exhibit a constant defect density independent on the indium concentration caused by crystalline mosaicity. Further investigations on the nucleation process may reveal the origin of this mosaicity.

More detailed investigation on the relaxation mechanism of thin films were performed. 15 and 30 nm thick $In_xGa_{1-x}As$ films were grown on graphene covered GaAs and for comparison on bare GaAs. The films were investigated by HRXRD measurements and Raman-spectroscopy. Films grown on graphene exhibit a uncommon large relaxation degree above 100%, which indicates a tensile strained film. It was speculated, that the nucleation of the $In_xGa_{1-x}As$ films applies tensile strain, due to island zipping. However, further investigation of the initial $In_xGa_{1-x}As$ nucleation layer grown on graphene covered GaAs is necessary. A suggestion is, to perform TEM measurements of the nucleation films and subsequent analysis of the atomic distances.

The results show, that the layer nucleation is probably the most delicate step in $In_xGa_{1-x}As$ film growth on graphene covered GaAs. Further optimisation of the nucleation layer will maybe reduce the film's defect density. The goal is probably to achieve layer-by-layer growth even during $In_xGa_{1-x}As$ nucleation, probably at lower growth rates or on patterned graphene samples.

Appendix A

Growth sheets

In the following, the growth sheets of the all grown and characterised samples are given in a numerical order.

- The following samples were grown to investigate the $In_xGa_{1-x}As$ nucleation in section 5.2:
  A1956, A1968, A1969, A1970, A1974, A1982, A2006, A2017, A2028

- The following samples were grown to investigate 200 nm thick $In_xGa_{1-x}As$ films in section 5.3:
  A1848, A1890, A1947, A1955, A1983, A1984, A2031, A2110, A2134

- The following samples were grown to investigate thinner $In_xGa_{1-x}As$ films in section 5.3:
  A1954, A2030, A2032, A2134, A2137

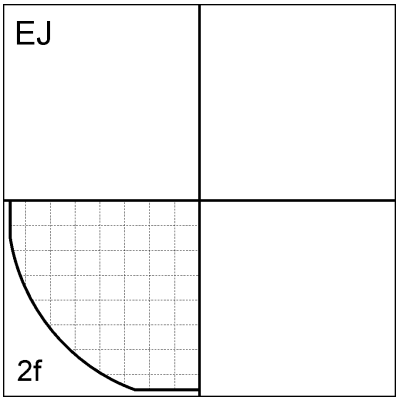

Sample: **A1848**

Material: GaAs

Orientation: (100)

Wafer:

Rotation: 10

Pressure (mBar): 1.0×10^{-9}

Date: 26.02.2021

File: a1848.asl

		300K	77K	4.2K	1K
dark	μ [cm^2 / Vs]				
	n [cm^{-2}]				
illum	μ [cm^2 / Vs]				
	n [cm^{-2}]				

Layer	*Loop*	*T [°C]*	*Dur. [s]*	*Thickn. [nm]*
Substrate				
$In_{0.70}Ga_{0.30}As$		300.0	2000.0	200

growth rate

GaAs	0.025 nm/s
InAs	0.075 nm/s

Comment

p_As4=2.2E-5 mbar
T_bandit=300°

(Grown by T. Henksmeier)

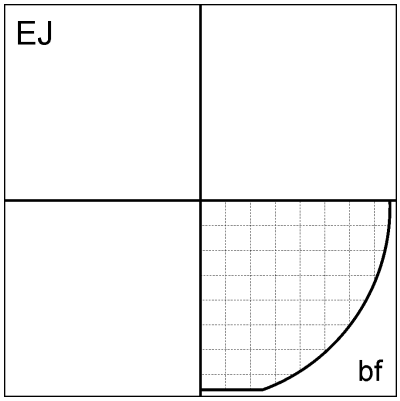

Sample: **A1890**

Material: GaAs

Orientation: (100)

Wafer:

Rotation: 10

Pressure (mBar): 2.5×10^{-9}

Date: 16.03.2021

File: a1890.asl

		300K	77K	4.2K	1K
dark	μ [cm^2 / Vs]				
	n [cm^{-2}]				
illum	μ [cm^2 / Vs]				
	n [cm^{-2}]				

Layer	*Loop*	*T [°C]*	*Dur. [s]*	*Thickn. [nm]*
Substrate				
$In_{0.50}Ga_{0.50}As$		300.0	2000.0	200

growth rate

GaAs	0.04 nm/s
InAs	0.06 nm/s

Comment

p_As4=2.2E-5 mbar
T_bandit=300°C

(Grown by T. Henksmeier)

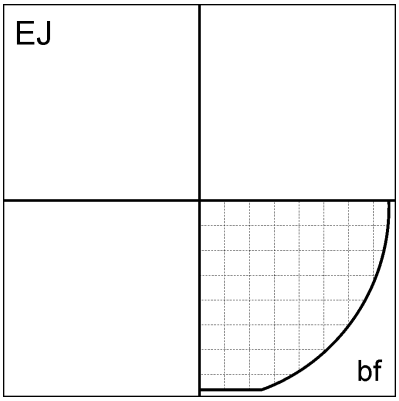

Sample: **A1947**

Material: GaAs

Orientation: (100)

Wafer:

Rotation: 10

Pressure (mBar): 1.9×10^{-9}

Date: 01.05.2021

File: a1947.asl

		300K	77K	4.2K	1K
dark	μ [cm^2 / Vs]				
	n [cm^{-2}]				
illum	μ [cm^2 / Vs]				
	n [cm^{-2}]				

Layer	*Loop*	*T [°C]*	*Dur. [s]*	*Thickn. [nm]*
Substrate				
$In_{0.25}Ga_{0.75}As$		300.0	2000	200

growth rate

GaAs	0.07 nm/s
InAs	0.03 nm/s

Comment

p_As4=2.0E-5 mbar
T_bandit=300°C

(Grown by T. Henksmeier)

UNIVERSITÄT PADERBORN
Die Universität der Informationsgesellschaft

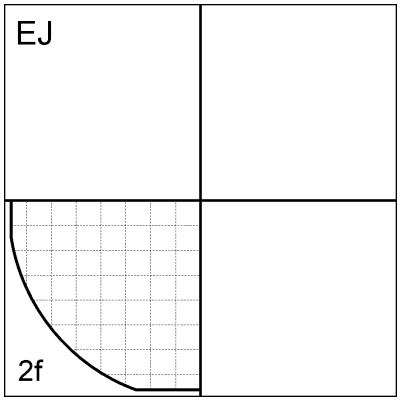

Sample: **A1954**

Material: GaAs

Orientation: (100)

Wafer:

Rotation: 10

Pressure (mBar): 1.0×10^{-8}

Date: 04.05.2021

File: a1954.asl

		300K	77K	4.2K	1K
dark	μ [cm^2 / Vs]				
	n [cm^{-2}]				
illum	μ [cm^2 / Vs]				
	n [cm^{-2}]				

Layer	*Loop*	*T [°C]*	*Dur. [s]*	*Thickn. [nm]*
Substrate				
$In_{0.15}Ga_{0.85}As$		300.0	250.0	25

growth rate

GaAs	0.085 nm/s
InAs	0.015 nm/s

Comment

p_As=1.2E-5 mbar
T_banidt=300°C

(Grown by T. Henksmeier)

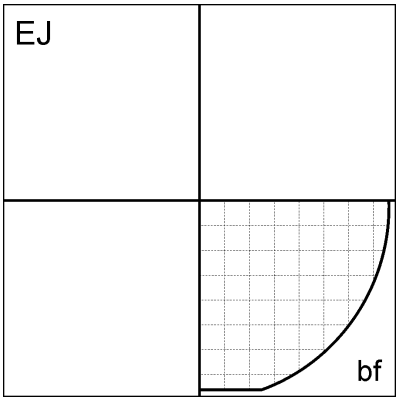

Sample: **A1955**

Material: GaAs

Orientation: (100)

Wafer:

Rotation: 10

Pressure (mBar): 2.3×10^{-8}

Date: 04.05.2021

File: a1955.asl

		300K	77K	4.2K	1K
dark	μ [cm^2 / Vs]				
	n [cm^{-2}]				
illum	μ [cm^2 / Vs]				
	n [cm^{-2}]				

Layer	*Loop*	*T [°C]*	*Dur. [s]*	*Thickn. [nm]*
Substrate				
$In_{0.13}Ga_{0.87}As$		300.0	2000.0	200

growth rate

GaAs	0.085 nm/s
InAs	0.015 nm/s

Comment

p_As4=1.2E-5 mbar
T_bandit=300°C

(Grown by T. Henksmeier)

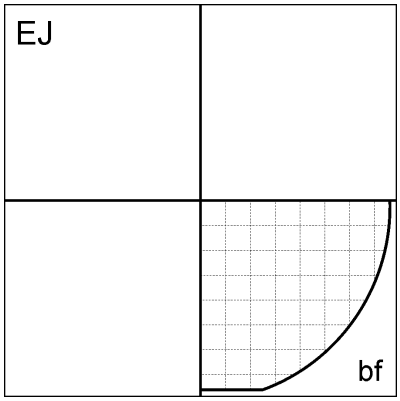

Sample: **A1956**

Material: GaAs

Orientation: (100)

Wafer:

Rotation: 10

Pressure (mBar): 2.2×10^{-8}

Date: 04.05.2021

File: a1956.asl

		300K	77K	4.2K	1K
dark	μ [cm² / Vs]				
	n [cm⁻²]				
illum	μ [cm² / Vs]				
	n [cm⁻²]				

Layer	*Loop*	*T [°C]*	*Dur. [s]*	*Thickn. [nm]*
Substrate				
$In_{0.15}Ga_{0.85}As$		300.0	50.0	5

growth rate

GaAs	0.085 nm/s
InAs	0.015 nm/s

Comment

p_As=0.9E-5 mbar
T_bandit=300°C

(Grown by T. Henksmeier)

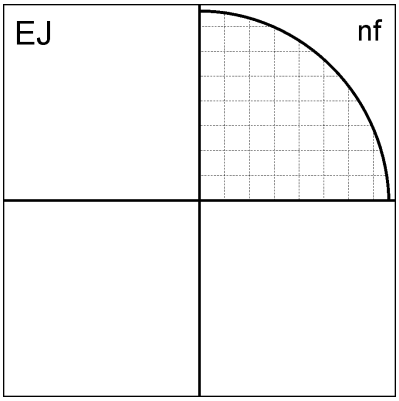

Sample: **A1968**

Material: GaAs

Orientation: (100)

Wafer:

Rotation: 10

Pressure (mBar): 3 x 10^{-9}

Date: 10.05.2021

File: a1968.asl

		300K	77K	4.2K	1K
dark	µ [cm^2 / Vs]				
	n [cm^{-2}]				
illum	µ [cm^2 / Vs]				
	n [cm^{-2}]				

Layer	*Loop*	*T [°C]*	*Dur. [s]*	*Thickn. [nm]*
Substrate				
$In_{0.15}Ga_{0.85}As$		300.0	20.0	2

growth rate

GaAs	0.085 nm/s
InAs	0.015 nm/s

Comment

p_As4=1.2E-5 mbar
T_bandit=300°C

(Grown by T. Henksmeier)

UNIVERSITÄT PADERBORN
Die Universität der Informationsgesellschaft

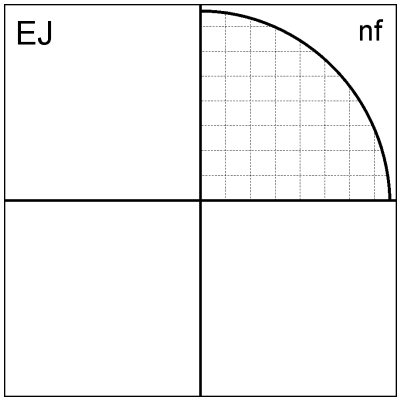

Sample: **A1969**

Material: GaAs

Orientation: (100)

Wafer:

Rotation: 10

Pressure (mBar): 3.2×10^{-9}

Date: 10.05.2021

File: a1969.asl

		300K	77K	4.2K	1K
dark	μ [cm² / Vs]				
	n [cm⁻²]				
illum	μ [cm² / Vs]				
	n [cm⁻²]				

Layer	*Loop*	*T [°C]*	*Dur. [s]*	*Thickn. [nm]*
Substrate				
$In_{0.15}Ga_{0.85}As$		300.0	5.0	0.5

growth rate

GaAs	0.085 nm/s
InAs	0.015 nm/s

Comment

p_As4=0.9E-5 mbar
T_Bandit=300°C

(Grown by)

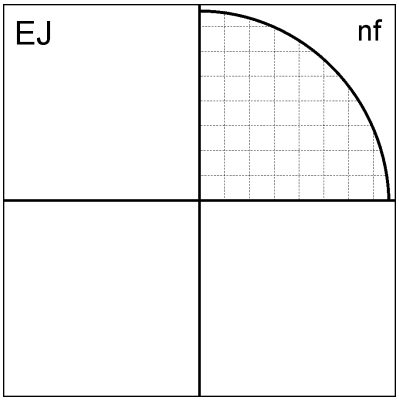

Sample: **A1970**

Material: GaAs

Orientation: (100)

Wafer:

Rotation: 10

Pressure (mBar): 6 x 10^{-9}

Date: 10.05.2021

File: a1970.asl

		300K	77K	4.2K	1K
dark	µ [cm^2 / Vs]				
	n [cm^{-2}]				
illum	µ [cm^2 / Vs]				
	n [cm^{-2}]				

Layer	*Loop*	*T [°C]*	*Dur. [s]*	*Thickn. [nm]*
Substrate				
$In_{0.15}Ga_{0.85}As$		385.0	50.0	5

growth rate

GaAs	0.085 nm/s
InAs	0.015 nm/s

Comment

p_As4=1.8E-5 mbar
T_Bandit=385°C

(Grown by T. Henksmeier)

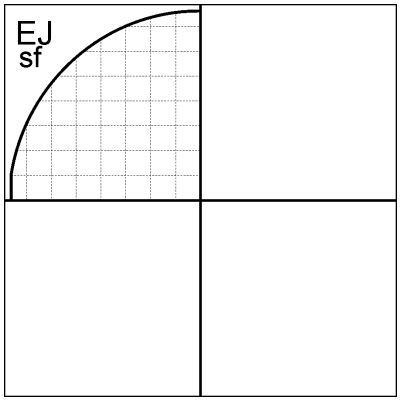

Sample: **A1974**

Material: GaAs

Orientation: (100)

Wafer:

Rotation: 10

Pressure (mBar): 4.3×10^{-9}

Date: 12.05.2021

File: a1974.asl

		300K	77K	4.2K	1K
dark	μ [cm² / Vs]				
	n [cm⁻²]				
illum	μ [cm² / Vs]				
	n [cm⁻²]				

Layer	*Loop*	*T [°C]*	*Dur. [s]*	*Thickn. [nm]*
Substrate				
$In_{0.15}Ga_{0.85}As$		480.0	50.0	5

growth rate

GaAs	0.085 nm/s
InAs	0.015 nm/s

Comment

p_As4=2.0E-5 mbar
T_bandit=485°C

(Grown by T. Henksmeier)

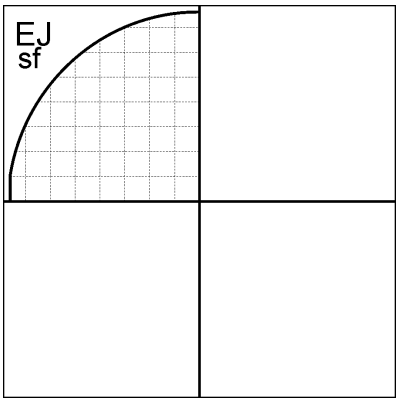

Sample:	**A1982**
Material:	GaAs
Orientation:	(100)
Wafer:	
Rotation:	10
Pressure (mBar):	1.98×10^{-9}
Date:	18.05.2021
File:	a1982.asl

		300K	77K	4.2K	1K
dark	μ [cm^2 / Vs]				
	n [cm^{-2}]				
illum	μ [cm^2 / Vs]				
	n [cm^{-2}]				

Layer	*Loop*	*T [°C]*	*Dur. [s]*	*Thickn. [nm]*
Substrate				
$In_{0.50}Ga_{0.50}As$		300.0	50.0	5

growth rate

GaAs	0.05 nm/s
InAs	0.05 nm/s

Comment

p_As=1.1E-5 mbar
T_bandit=300°C

(Grown by T. Henksmeier)

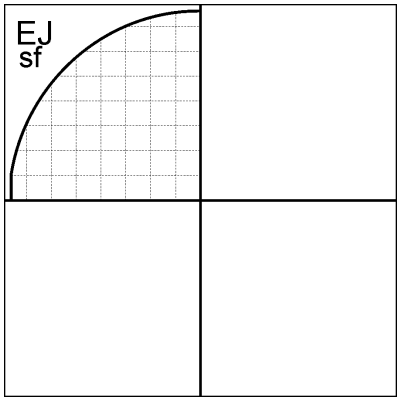

Sample:	**A1983**
Material:	GaAs
Orientation:	(100)
Wafer:	
Rotation:	10
Pressure (mBar):	2.9 x 10^{-9}
Date:	18.05.2021
File:	a1983.asl

		300K	77K	4.2K	1K
dark	μ [cm^2 / Vs]				
	n [cm^{-2}]				
illum	μ [cm^2 / Vs]				
	n [cm^{-2}]				

Layer	*Loop*	*T [°C]*	*Dur. [s]*	*Thickn. [nm]*
Substrate				
$In_{0.15}Ga_{0.85}As$		300.0	5.0	0.5
$In_{0.15}Ga_{0.85}As$		385.0	1995.0	199.5

growth rate

GaAs	0.085 nm/s
InAs	0.015 nm/s

Comment

Nucleation:
p_As4=0.9E-5 mbar
T_bandit=300°C

Overgrowth:
p_As4=1.9E-5 mbar
T_bandit=385°C

(Grown by T. Henksmeier)

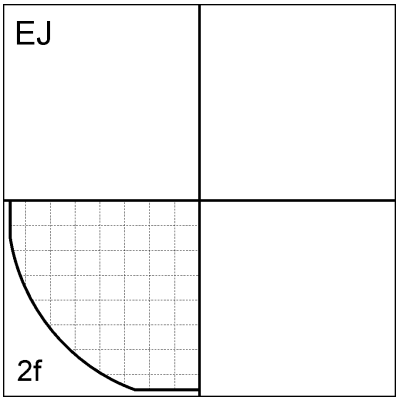

Sample: **A1984**

Material: GaAs

Orientation: (100)

Wafer:

Rotation: 10

Pressure (mBar): 3 x 10^{-8}

Date: 18.05.2021

File: a1984.asl

		300K	77K	4.2K	1K
dark	μ [cm^2 / Vs]				
	n [cm^{-2}]				
illum	μ [cm^2 / Vs]				
	n [cm^{-2}]				

Layer	*Loop*	*T [°C]*	*Dur. [s]*	*Thickn. [nm]*
Substrate				
$In_{0.50}Ga_{0.50}As$		300.0	5	0.5
$In_{0.50}Ga_{0.50}As$		385.0	1980.0	198

growth rate

GaAs 0.05 nm/s

InAs 0.05 nm/s

Comment

Nucleation:
p_As4=0.9E-5 mbar
T_bandit=300°C

Overgrowth:
p_As4=2.2E-5 mbar
T_bandit=385°C

(Grown by T. Henksmeier)

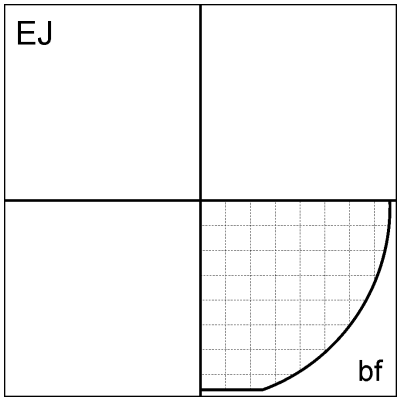

Sample: **A2006**

Material: GaAs

Orientation: (100)

Wafer:

Rotation: 10

Pressure (mBar): 1.7×10^{-9}

Date: 24.05.2021

File: a2006.asl

		300K	77K	4.2K	1K
dark	μ [cm^2 / Vs]				
	n [cm^{-2}]				
illum	μ [cm^2 / Vs]				
	n [cm^{-2}]				

Layer	*Loop*	*T [°C]*	*Dur. [s]*	*Thickn. [nm]*
Substrate				
$In_{0.30}Ga_{0.70}As$		300.0	50.0	5

growth rate

GaAs	0.07 nm/s
InAs	0.03 nm/s

Comment

p_As4=1.2E-5 mbar
T_bandit=300°C

(Grown by T. Henksmeier)

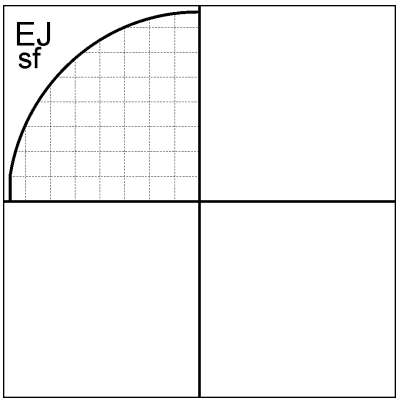

Sample: **A2017**

Material: GaAs

Orientation: (100)

Wafer:

Rotation: 10

Pressure (mBar): 4.7×10^{-9}

Date: 27.05.2021

File: a2017.asl

		300K	77K	4.2K	1K
dark	μ [cm² / Vs]				
	n [cm⁻²]				
illum	μ [cm² / Vs]				
	n [cm⁻²]				

Layer	*Loop*	*T [°C]*	*Dur. [s]*	*Thickn. [nm]*
Substrate				
InAs		300.0	50.0	5

growth rate
InAs 0.1 nm/s

Comment
p_As4=1.2E-5 mbar
T_bandit=300°C

(Grown by T. Henksmeier)

UNIVERSITÄT PADERBORN
Die Universität der Informationsgesellschaft

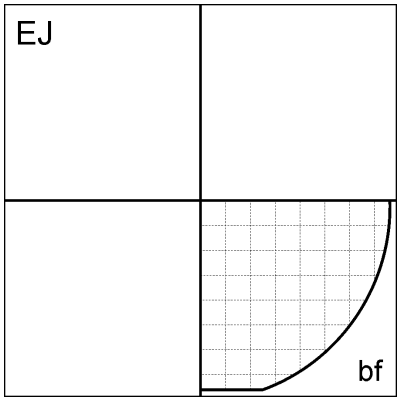

Sample: **A2028**

Material: GaAs

Orientation: (100)

Wafer:

Rotation: 10

Pressure (mBar): 2×10^{-9}

Date: 04.06.2021

File: a2028.asl

		300K	77K	4.2K	1K
dark	μ [cm² / Vs]				
	n [cm⁻²]				
illum	μ [cm² / Vs]				
	n [cm⁻²]				

Layer	*Loop*	*T [°C]*	*Dur. [s]*	*Thickn. [nm]*
Substrate				
$In_{0.75}Ga_{0.25}As$		300.0	50.0	5

growth rate

GaAs	0.015 nm/s
InAs	0.085 nm/s

Comment

p_As4=0.9E-5 mbar
T_bandit=300°C

(Grown by T. Henksmeier)

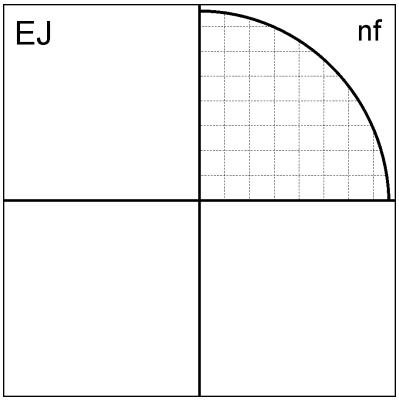

Sample: **A2030**

Material: GaAs

Orientation: (100)

Wafer:

Rotation: 10

Pressure (mBar): 5 x 10^{-9}

Date: 14.06.2021

File: a2030.asl

		300K	77K	4.2K	1K
dark	μ [cm^2 / Vs]				
	n [cm^{-2}]				
illum	μ [cm^2 / Vs]				
	n [cm^{-2}]				

Layer	*Loop*	*T [°C]*	*Dur. [s]*	*Thickn. [nm]*
Substrate				
$In_{0.15}Ga_{0.85}As$		300.0	10.0	0.5
$In_{0.15}Ga_{0.85}As$		385.0	290.0	29.5

growth rate

GaAs 0.085 nm/s

InAs 0.015 nm/s

Comment

Nucleation:
p_As4=1.2E-5 mbar
T_bandit=300°C

Overgrowth:
p_As4=1.8E-5 mbar
T_bandit=385°C

(Grown by T. Henksmeier)

UNIVERSITÄT PADERBORN
Die Universität der Informationsgesellschaft

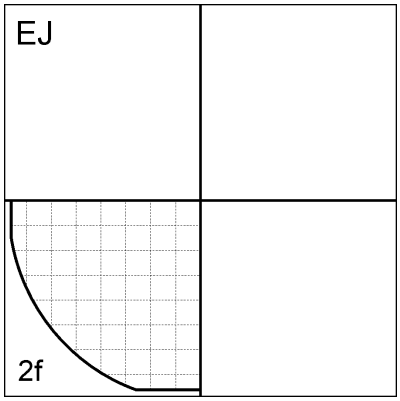

Sample:	**A2031**
Material:	GaAs
Orientation:	(100)
Wafer:	
Rotation:	10
Pressure (mBar):	1 x 10^{-8}
Date:	14.07.2021
File:	a2031.asl

		300K	77K	4.2K	1K
dark	µ [cm^2 / Vs]				
	n [cm^{-2}]				
illum	µ [cm^2 / Vs]				
	n [cm^{-2}]				

Layer	*Loop*	*T [°C]*	*Dur. [s]*	*Thickn. [nm]*
Substrate				
$In_{0.30}Ga_{0.70}As$		300.0	10.0	0.5
$In_{0.30}Ga_{0.70}As$		385.0	1999.9	200

growth rate

GaAs	0.07 nm/s
InAs	0.03 nm/s

Comment

Nucleation:
p_As4=1.0E-5 mbar
T_bandit=300°C

Overgrowth:
p_As4=2.0E-5 mbar
T_bandit=385°C

(Grown by T. Henksmeier)

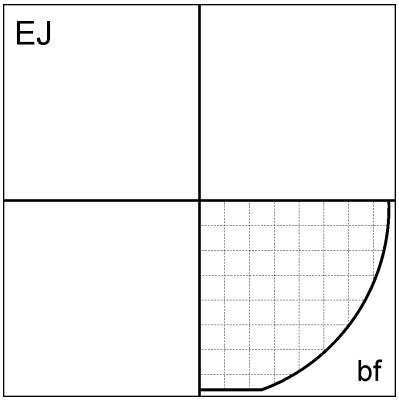

Sample:	**A2032**
Material:	GaAs
Orientation:	(100)
Wafer:	
Rotation:	10
Pressure (mBar):	2 x 10^{-9}
Date:	14.06.2021
File:	a2032.asl

		300K	77K	4.2K	1K
dark	µ [cm^2 / Vs]				
	n [cm^{-2}]				
illum	µ [cm^2 / Vs]				
	n [cm^{-2}]				

Layer	*Loop*	*T [°C]*	*Dur. [s]*	*Thickn. [nm]*
Substrate				
$In_{0.28}Ga_{0.72}As$		300.0	10.0	0.5
$In_{0.28}Ga_{0.72}As$		385.0	150.0	14.5

growth rate

GaAs	0.07 nm/s
InAs	0.03 nm/s

Comment

Nucleation:
p_As4=0.9E-5 mbar
T_bandit=300°C

Overgrowth:
p_As4=1.9E-5 mbar
T_bandit=385°C

(Grown by T. Henksmeier)

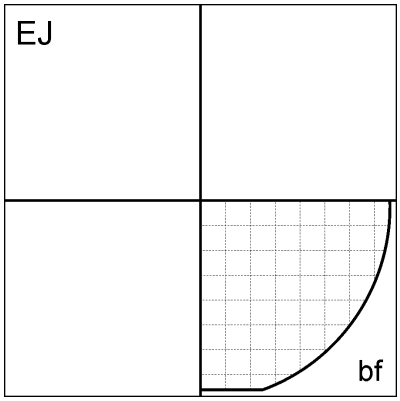

Sample: **A2110**

Material: GaAs

Orientation: (100)

Wafer:

Rotation: 10

Pressure (mBar): 3.5×10^{-9}

Date: 14.07.2021

File: a2110.asl

		300K	77K	4.2K	1K
dark	μ [cm² / Vs]				
	n [cm⁻²]				
illum	μ [cm² / Vs]				
	n [cm⁻²]				

Layer	*Loop*	*T [°C]*	*Dur. [s]*	*Thickn. [nm]*
Substrate				
$In_{0.17}Ga_{0.83}As$		300.0	5.0	0.5
$In_{0.17}Ga_{0.83}As$		385.0	2215.0	199.5

growth rate

GaAs	0.015 nm/s
InAs	0.075 nm/s

Comment

Nucleation:
p_As4=1.0E-5 mbar
T_bandit=300°C

Overgrowth:
p_As4=2.0E-5 mbar
T_bandit=385°C

(Grown by T. Henksmeier)

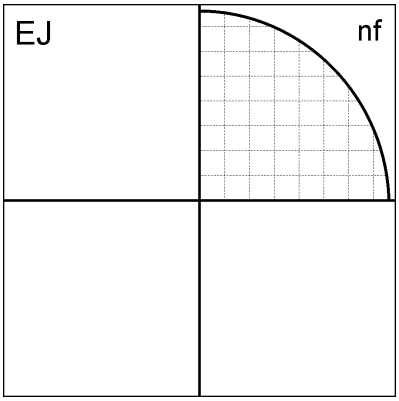

Sample: **A2134**

Material: GaAs

Orientation: (100)

Wafer:

Rotation: 10

Pressure (mBar): 3.5×10^{-9}

Date: 20.07.2021

File: a2134.asl

		300K	77K	4.2K	1K
dark	μ [cm² / Vs]				
	n [cm⁻²]				
illum	μ [cm² / Vs]				
	n [cm⁻²]				

Layer	*Loop*	*T [°C]*	*Dur. [s]*	*Thickn. [nm]*
Substrate				
$In_{0.30}Ga_{0.70}As$		300.0	150	15

growth rate

GaAs	0.07 nm/s
InAs	0.03 nm/s

Comment

p_As4=2.0E-5 mbar
T_bandit=300°C

(Grown by T. Henksmeier)

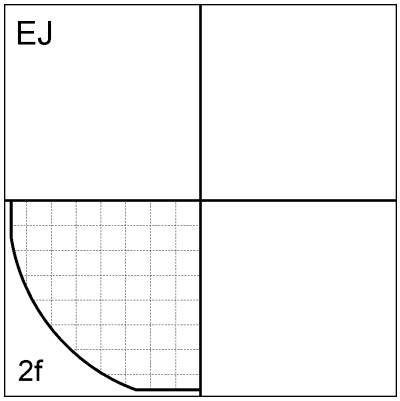

Sample: **A2137**

Material: GaAs

Orientation: (100)

Wafer:

Rotation: 10

Pressure (mBar): 4.1×10^{-9}

Date: 20.07.2021

File: a2137.asl

		300K	77K	4.2K	1K
dark	μ [cm² / Vs]				
	n [cm⁻²]				
illum	μ [cm² / Vs]				
	n [cm⁻²]				

Layer	*Loop*	*T [°C]*	*Dur. [s]*	*Thickn. [nm]*
Substrate				
$In_{0.15}Ga_{0.85}As$		300.0	300	30

growth rate

GaAs	0.085 nm/s
InAs	0.015 nm/s

Comment

p_As4=0.9E-5 mbar
T_bandit=300°C

(Grown by T. Henksmeier)

Bibliography

[1] Ayers, J. E. 25 - Low-Temperature and Metamorphic Buffer Layers. In Kuech, T. F. (ed.) *Handbook of Crystal Growth (Second Edition)*, Handbook of Crystal Growth, 1007–1056 (North-Holland, Boston, 2015).

[2] Kujofsa, T. & Ayers, J. E. Equilibrium Lattice Relaxation and Misfit Dislocations in Step-Graded In(x)Ga(1–x)As/GaAs (001) and In(x)Al(1–x)As/GaAs (001) Metamorphic Buffer Layers. *Journal of Electronic materials* **45**, 2831–2836 (2016).

[3] Kumar, R., Bag, A., Mukhopadhyay, P., Das, S. & Biswas, D. Comparison of Different Grading Schemes in InGaAs Metamorphic Buffers on GaAs Substrate: Tilt Dependence on Cross-Hatch Irregularities. *Applied Surface Science* **357**, 922–930 (2015).

[4] Liang, D., Wei, T., Wang, J. & Li, J. Quasi van der Waals epitaxy nitride materials and devices on two-dimension materials. *Nano Energy* **69**, 104463 (2020).

[5] Kum, H. *et al.* Epitaxial growth and layer-transfer techniques for heterogeneous integration of materials for electronic and photonic devices. *Nature Electronics* **2**, 1–12 (2019).

[6] Kim, J. *et al.* Principle of direct van der Waals epitaxy of single-crystalline films on epitaxial graphene. *Nature communications* **5**, 4836 (2014).

[7] Koma, A. Van der Waals epitaxy—a new epitaxial growth method for a highly lattice-mismatched system. *Thin Solid Films* **216**, 72–76 (1992). Papers presented at the International Workshop on Science and Technology of Thin Films for the 21st Century, Evanston,IL, USA, July 28-August 2, 1991.

[8] Alaskar, Y. *et al.* Towards van der Waals Epitaxial Growth of GaAs on Si using a Graphene Buffer Layer. *Advanced Functional Materials* **24**, 6629–6638 (2014).

[9] Alaskar, Y. *et al.* Theoretical and experimental study of highly textured GaAs on silicon using a graphene buffer layer. *Journal of Crystal Growth* **425**, 268–273 (2015). The 18th International Conference on Molecular Beam Epitaxy (MBE 2014).

[10] Kim, Y. *et al.* Remote epitaxy through graphene enables two-dimensional material-based layer transfer. *Nature* **544**, 340–343 (2017).

[11] Kong, W. *et al.* Polarity governs atomic interaction through two-dimensional materials. *Nature Materials* **17** (2018).

[12] Bae, S.-H. *et al.* Graphene-assisted spontaneous relaxation towards dislocation-free heteroepitaxy. *Nature Nanotechnology* **15** (2020).

[13] Badokas, K. *et al.* Remote epitaxy of GaN via graphene on GaN/sapphire templates. *Journal of Physics D: Applied Physics* **54**, 205103 (2021).

[14] Jiang, J. *et al.* Carrier lifetime enhancement in Halide Perovskite via remote epitaxy. *Nature Communications* **10** (2019).

[15] Bae, S.-H. *et al.* Integration of bulk materials with two-dimensional materials for physical coupling and applications. *Nature Materials* **18**, 550–560 (2019).

[16] Kum, H. *et al.* Heterogeneous integration of single-crystalline complex-oxide membranes. *Nature* **578**, 75–81 (2020).

[17] Qiao, K. *et al.* Graphene Buffer Layer on SiC as a Release Layer for High-Quality Freestanding Semiconductor Membranes. *Nano Letters* **21**, 4013–4020 (2021). PMID: 33900785.

[18] Kim, H. *et al.* Impact of 2D–3D Heterointerface on Remote Epitaxial Interaction through Graphene. *ACS Nano* **15**, 10587–10596 (2021). PMID: 34081854.

[19] Cheng, K.-Y. Molecular beam epitaxy technology of III-V compound semiconductors for optoelectronic applications. *Proceedings of the IEEE* **85**, 1694–1714 (1997).

[20] Grundmann, M. *The Physicsof Semiconductors* (Springer, 2010).

[21] Pohl, U. W. *Epitaxy of Semiconductors* (Springer, 2013).

[22] Sze, S. M. & Kwog, K. N. *Physics of Semicondutor Devices* (Wiley, 2006).

[23] Shields, A. Semiconductor quantum light sources. *Nature Photonics* **1** (2007).

[24] Bhattacharya, P. *Properties of Lattice-matched and Strained Indium Gallium Arsenide* (INSPEC, the Institution of Electrical Engineers, 1993).

[25] http://www.ioffe.ru/SVA/NSM/Semicond/GaAs/. Properites of GaAs (2021).

[26] http://www.ioffe.ru/SVA/NSM/Semicond/InAs/. Properties of InAs (2021).

[27] Vegard, L. Die Konstitution der Mischkristalle und die Raumfüllung der Atome. *Zeitschrift für Physik* **5**, 17–26 (1921).

[28] Varshni, Y. P. Temperature dependence of the energy gap in semiconductors. *Physica* (1967).

[29] Herman, M. A., Richter, W. & Sitter, H. *Epitaxy - Physical Principles and Technical Implementation* (Springer, 2004).

[30] Venables, J. A., Spiller, G. D. T. & Hanbucken, M. Nucleation and growth of thin films. *Reports on Progress in Physics* **47**, 399–459 (1984).

[31] Young, T. III. An essay on the cohesion of fluids. *Philosophical Transactions of the Royal Society of London* **95**, 65–87 (1805).

[32] Berger, P. R., Chang, K., Bhattacharya, P., Singh, J. & Bajaj, K. K. Role of strain and growth conditions on the growth front profile of In(x)Ga(1-x)As on GaAs during the pseudomorphic growth regime. *Applied Physics Letters* **53**, 684–686 (1988).

[33] Whaley, G. J. & Cohen, P. I. Summary Abstract: The growth of strained InGaAs on GaAs: Kinetics versus energetics. *Journal of Vacuum Science & Technology B: Microelectronics Processing and Phenomena* **6**, 625–626 (1988).

[34] Grandjean, N. & Massies, J. Extension of the layer-by-layer growth regime of In(x)Ga(1-x)As on GaAs (001). *Semiconductor Science and*

Technology **8**, 2031–2034 (1993).

[35] Anderson, P. M., Hirth, J. P. & Lothe, J. *Theory of Dislocations* (2017).

[36] Yarlagadda, B. *et al.* X-ray characterization of dislocation density asymmetries in heteroepitaxial semiconductors. *Applied Physics Letters* **92**, 202103 (2008).

[37] Sorokin, S. *et al.* Peculiarities of strain relaxation in linearly graded In(x)Ga(1–x)As/GaAs(001) metamorphic buffer layers grown by molecular beam epitaxy. *Journal of Crystal Growth* **455**, 83–89 (2016).

[38] Vanhollebeke, K., Moerman, I., Van Daele, P. & Demeester, P. Compliant substrate technology: Integration of mismatched materials for opto-electronic applications. *Progress in Crystal Growth and Characterization of Materials* **41**, 1–55 (2000).

[39] Christensen, N. E., Satpathy, S. & Pawlowska, Z. Bonding and ionicity in semiconductors. *Phys. Rev. B* **36**, 1032–1050 (1987).

[40] Ichimiya, A. & Cohen, P. I. *Reflection high-energy electron diffraction* (Cambridge University Press, 2004).

[41] Birkholz, M. *Thin Film Analysis by X-Ray Scattering* (Wiley, 2006).

[42] Bragg, W. H. & Bragg, W. L. The reflection of X-rays by crystals. *Proc. R. Soc. Lond. A* **88**, 428–438 (1913).

[43] Arthur, J. R. Interaction of Ga and As_2 Molecular Beams with GaAs Surfaces. *Journal of Applied Physics* **39**, 4032–4034 (1968).

[44] Arthur, J. R. & LePore, J. J. GaAs, GaP and GaAs(x)P(1-x) Epitaxial Films Grown by Molecular Beam Deposition. *Journal of Vacuum Science and Technology* **6**, 545–548 (1969).

[45] Cho, A. Y. Morphology of Epitaxial Growth of GaAs by a Molecular Beam Method: The Observation of Surface Structures. *Journal of Applied Physics* **41**, 2780–2786 (1970).

[46] Holloway, P. H. & McGuire, G. E. *Handbook of Compound Semiconductors* (Noyes Publications, 1996).

[47] Sharma, N. L. *Molecular Beam Epitaxy of Tailored (In,Ga)As/GaAs Quantum Dot Heterostructures.* Ph.D. thesis, Paderborn University (2017).

[48] MBE-Komponenten GmbH. UHV-System Reuter Zeichnung (2014).

[49] Trapp, A. *Molecular beam epitaxy of quantum dots on misoriented GaAs(111)B by droplet epitaxy.* Ph.D. thesis, Paderborn University (2019).

[50] k-Space Associates, Inc.2021 *Manual KSA-BandiT.*

[51] Hasegawa, S. *Reflection High-Energy Electron Diffraction*, 1–14 (American Cancer Society, 2012).

[52] Däweritz, L. & Hey, R. Reconstruction and defect structure of vicinal GaAs(001) and Al(x)Ga(1-x)As(001) surfaces during MBE growth. *Surface Science* **236**, 15–22 (1990).

[53] Vasquez, R. P., Lewis, B. F. & Grunthaner, F. J. X-ray photoelectron spectroscopic study of the oxide removal mechanism of GaAs (100) molecular beam epitaxial substrates in in situ heating. *Applied Physics Letters* **42**, 293–295 (1983).

[54] Lee, J., West, K., Baldwin, K. & Pfeiffer, L. Smoothness and cleanliness of the GaAs (100) surface after thermal desorption of the native oxide for the synthesis of high mobility structures using molecular beam epitaxy. *Journal of Crystal Growth* **356**, 46–52 (2012).

[55] Mirecki Millunchick, J., Riposan, A., Dall, B., Pearson, C. & Orr, B. Surface reconstructions of In(x)Ga(1-x)As alloys. *Surface Science* **550**, 1–7 (2004).

[56] Lee, H.-C. Review of inductively coupled plasmas: Nano-applications and bistable hysteresis physics. *Applied Physics Rewiew* (2018).

[57] Jansen, H., Gardeniers, H., de Boer, M., Elwenspoek, M. & Fluitman, J. A survey on the reactive ion etching of silicon in microtechnology. *Journal of Micromechanics and Microengineering* **6**, 14–28 (1996).

[58] Rossnagel, S. M., Westwood, W. D. & Cuomo, J. J. *Handbook of Plasma Processing Technology* (Noyes publications, 1990).

[59] Oxford Instruments plc. 2021 Inductivly couple plasma - reactive ion etching. URL `https://plasma.oxinst.com/technology/icp-etching`.

[60] Lagmuir, I. Oscillations in ionized gases. *Phys. Rev.* **33**, 195–210 (1928).

[61] Nanosurf AG. *Manual: AFM working principle.*

[62] NanoAndMore GmbH. AFM cantilever. URL https://www.nanoandmore.com/AFM-Probe-PPP-XYCONTR.

[63] Kidd, P. *X'Pert MRD User Guide*. Panalytical.

[64] Fatemi, M., Chaudhuri, J., Mittereder, J. & Christou, A. X-ray double-crystal analysis of misorientation and strain in GaAs/Si and related heterostructures. *Journal of Applied Physics* **73**, 1154–1160 (1993).

[65] Ul-Hamid, A. *A Beginners' Guide to Scanning Electron Microscopy* (Springer, 2018).

[66] Goldstein, J. I. *et al. Scanning Electron Microscopy and X-Ray Microanalysis* (Springer, 2018).

[67] Weber, W. H. & Merlin, R. *Raman Scattering in Materials Science* (Springer, 2000).

[68] Schrader, B. *Infrared and Raman Spectroscopy: Methods and Applications* (Wiley, 2008).

[69] Rüsing, M. *In depth Raman analysis of the ferroelectrics $KTiOPO_4$ and $LiNbO_3$: role of domain boundaries and defects*. Ph.D. thesis, Paderborn University (2018).

[70] Private communication with Elias Kluth (2021).

[71] Private communication with PD Dr. Martin Fenerberg, Elias Kluth and Johann Friedeman Schulz (2021).

[72] Hüfner, S. *Photoelectron Spectroscopy: Principles and Applications* (Springer, 2003).

[73] Private communication with Martin Voigt (2021).

[74] Williams, D. B., Carter, D. B. & Barry, C. *Transmission Electron Microscopy* (Springer, 2009).

[75] TEM short manual (2010). URL https://warwick.ac.uk/fac/sci/physics/current/postgraduate/regs/mpagswarwick/ex5/techniques/structural/tem/.

[76] Private communication with Dr. Thomas Riedl (2021).

[77] ACS-Materials, ACS Material, LLC959 E Walnut Street 100, Pasadena, CA 91106. *Manual trivial transfer graphene* (2021). URL https://www.acsmaterial.com/trivial-transfer-graphenetm.html.

[78] Ferrah, D. *et al.* CF_4/H_2 Plasma Cleaning of Graphene Regenerates

Electronic Properties of the Pristine Material. *ACS Applied Nano Materials* **2**, 1356–1366 (2019).

[79] Cunge, G. *et al.* Dry efficient cleaning of poly-methyl-methacrylate residues from graphene with high-density H_2 and H_2-N_2 plasmas. *Journal of Applied Physics* **118**, 123302 (2015).

[80] Cheng, Z. *et al.* Toward Intrinsic Graphene Surfaces: A Systematic Study on Thermal Annealing and Wet-Chemical Treatment of SiO_2-Supported Graphene Devices. *Nano Letters* **11**, 767–771 (2011). PMID: 21218829.

[81] Lin, Y.-C. *et al.* Graphene Annealing: How Clean Can It Be? *Nano Letters* **12**, 414–419 (2012). PMID: 22149394.

[82] Suk, J. W. *et al.* Transfer of CVD-Grown Monolayer Graphene onto Arbitrary Substrates. *ACS Nano* **5**, 6916–6924 (2011). PMID: 21894965.

[83] Pirkle, A. *et al.* The effect of chemical residues on the physical and electrical properties of chemical vapor deposited graphene transferred to SiO_2. *Applied Physics Letters* **99**, 122108 (2011).

[84] Karlsson, L. H. *et al.* Graphene on graphene formation from PMMA residues during annealing. *Vacuum* **137**, 191–194 (2017).

[85] Zhuang, B., Li, S., Li, S. & Yin, J. Ways to eliminate PMMA residues on graphene - superclean graphene. *Carbon* **173**, 609–636 (2021).

[86] Mehedi, H.-A. *et al.* High density H_2 and He plasmas: Can they be used to treat graphene? *Journal of Applied Physics* **124**, 125304 (2018).

[87] Hug, D. *et al.* Anisotropic etching of graphite and graphene in a remote hydrogen plasma. *npj 2D Mater Appl* **1** (2017).

[88] Shi, Z. *et al.* Patterning Graphene with Zigzag Edges by Self-Aligned Anisotropic Etching. *Advanced Materials* **23**, 3061–3065 (2011).

[89] Luo, Z. *et al.* Thickness-Dependent Reversible Hydrogenation of Graphene Layers. *ACS Nano* **3**, 1781–1788 (2009). PMID: 19492823.

[90] Lim, Y.-D. *et al.* Si-Compatible Cleaning Process for Graphene Using Low-Density Inductively Coupled Plasma. *ACS Nano* **6**, 4410–4417 (2012). PMID: 22515680.

[91] Mao, H., Wang, R., Zhong, J., Zhong, S. & Chen, W. Mildly O_2 plasma treated CVD graphene as a promising platform for molecular sensing.

Carbon **76**, 212–219 (2014).

[92] Peltekis, N. *et al.* The effect of downstream plasma treatments on graphene surfaces. *Carbon* **50**, 395–403 (2012).

[93] Yun, H. *et al.* Removal of photoresist residues and healing of defects on graphene using H_2 and CH_4 plasma. *Applied Surface Science* **463**, 802–808 (2019).

[94] Rebaud, M. *et al.* Chemical Treatments for Native Oxides Removal of GaAs Wafers. *ECS Transactions* **69**, 243–250 (2015).

[95] Kang, M.-G., Sa, S.-H., Park, H.-H., Suh, K.-S. & Kyung-Hui Oh. The characterization of etched GaAs surface with HCl or H_3PO_4 solutions. *Thin Solid Films* **308-309**, 634–642 (1997).

[96] Lukeš, F. Oxidation of Si and GaAs in air at room temperature. *Surface Science* **30**, 91–100 (1972).

[97] Hallam, T., Berner, N. C., Yim, C. & Duesberg, G. S. Strain, Bubbles, Dirt, and Folds: A Study of Graphene Polymer-Assisted Transfer. *Advanced Materials Interfaces* **1**, 1400115 (2014).

[98] Davydova, A., Despiau-Pujo, E., Cunge, G. & Graves, D. B. H^+ ion-induced damage and etching of multilayer graphene in H_2 plasmas. *Journal of Applied Physics* **121**, 133301 (2017).

[99] Despiau-Pujo, E., Davydova, A., Cunge, G. & Graves, D. B. Hydrogen Plasma Processing of Graphene Surface. *Plasma Chem Plasma Process* **36**, 213–229 (2016).

[100] Leonhardt, D., Ghosh, S. & Han, S. M. Origin and removal of stacking faults in Ge islands nucleated on Si within nanoscale openings in SiO2. *Journal of Applied Physics* **110**, 073516 (2011).

[101] Floro, J. A. *et al.* The dynamic competition between stress generation and relaxation mechanisms during coalescence of Volmer–Weber thin films. *Journal of Applied Physics* **89**, 4886–4897 (2001).

[102] Nix, W. & Clemens, B. Crystallite coalescence: A mechanism for intrinsic tensile stresses in thin films. *Journal of Materials Research* **14**, 3467–3473 (1999).

[103] Nishinaga, T. Handbook of Crystal Growth: Thin Films and Epitaxy: Second Edition **3**, 1–1346 (2014).

[104] Lin, H. *et al.* X–ray diffraction analysis of step–graded In(x)Ga(1-x)As buffer layers grown by molecular beam epitaxy. *Journal of Crystal Growth* **323**, 17–20 (2011). Proceedings of the 16th International Conference on Molecular Beam Epitaxy (ICMBE).

[105] Groenen, J. *et al.* Optical-phonon behaviour in Ga(1–x)In(x)As: The role of microscopic strains and ionic plasmon coupling. *Physical Review B* **58**, 10452-10462 (1998).

[106] Ohta, K. *et al.* Anisotropci Surface Mirgration of Ga Atoms on GaAs(001). *Journal of Crystal Growth* **95**, 71-74 (1989).

[107] People, R. & Bean, J. C. Calculation of critical layer thickness versus lattice mismatch for Ge(x)Si(1–x)/Si strained-layer heterostructures. *Applied Physics Letters* **47**, 322–324 (1985).

List of Figures

List of Tables

Acronyms

AFM atomic force microscopy. 4, 23, 33, 35
As arsenic. 27

CVD chemical vapour deposition. 3

FWHM full width at half maximum. 37

Ga gallium. 27
GaAs gallium arsenide. 3
GaN gallium nitride. 3
GaP gallium phosphide. 3

HRXRD high-resolution X-ray diffraction. 4, 16, 23, 28, 35, 37

ICP inductively coupled plasma. 31
In indium. 27
InGaP indium gallium phosphide. 3

LPE liquid phase epitaxy. 8

MBE molecular beam epitaxy. 4, 8, 23, 24
MOCVD metalorganic chemical vapor deposition. 3, 8

PMMA Poly(methyl methacrylate). 31, 47

RF radio frequency. 31
RHEED reflection high-energy electron diffraction. 4, 16, 27
RIE reactive-ion etching. 4, 23, 31

SEM scanning electron microscopy. 4, 23, 41

SiC silicon carbide. 3

TEM transmission electron microscopy. 4, 23, 43

TSP-IGP ion-getter pump armed with titanium supplementation filaments. 25

UHV ultra-high vaccum. 8, 24

XPS X-ray photoelectron spectroscopy. 4, 23, 42

Appendix B

List of Publications

Part of this thesis have already been published in journals and conference proceedings. During the PhD studies, the following publications and submission to conferences were published:

Scientific publications

- **T. Henksmeier**, S. Shvarkov, A. Trapp, D. Reuter, Molecular beam epitaxy growth and temperature-dependend electrical characterisation of carbon doped GaAs on GaAs(111)B, J. Cryst. Growth, **512**, 164-168 (2019).

- M. Deppe, **T. Henksmeier**, J. W. Gerlach, D. Reuter, D. J. As, Molecular Beam Epitaxy Growth and Characterization of Germanium-Doped Cubic $Al_xGa_{1-x}N$, Phys. Status Solidi B, **257**, 1900532 (2020).

- **T. Henksmeier**, M. Eppinger, B. Reineke, T. Zentgraf, C. Meier, D. Reuter, Selective Etching of (111)B-Oriented $Al_xGa_{1-x}As$-Layers for Epitaxial Lift-Off, physica status solidi (a), **218**, 2000408 (2020).

- M. Hajlaoui, S. Ponzoni, M. Deppe, **T. Henksmeier**, D. J. As, D. Reuter, T. Zentgraf, G. Springholz, C. M. Schneider, S. Cramm,

M. Cinchetti, Extremely low-energy ARPES of quantum well states in cubic-GaN/AlN and GaAs/AlGaAs heterostructures, Scientific Reports, **11**, 19081 (2021).

- (**under review**) **T. Henksmeier**, J.F. Schulz, E. Kluth, M. Feneberg, R. Goldhahn, A. M. Sanchez, M. Voigt, G. Grundmeier, D. Reuter, Remote Epitaxy of $In_xGa_{1-x}As(001)$ on Graphene Covered GaAs(001) Substrates, J. Cryst. Growth (2021).

- (**under review**) M. Kobecki, A. V. Scherbakov, S. M. Kukhtaruk, D. D. Yaremkevich, **T. Henksmeier**, A. Trapp, D. Reuter, V. E. Gusev, A. V. Akimov, M. Bayer, Giant photoelasticity of polaritons for detection of coherent phonons in a superlattice with quantum sensitivity (2021).

Submission to conferences

- **T. Henksmeier**, S. Shvarkov, A. Trapp, D. Reuter, Molecular beam epitaxy growth and temperature-dependend electrical characterisation of carbon doped GaAs on GaAs(111)B„ ICMBE, Shanghai (2018).

- **T. Henksmeier**, S. Shvarkov, A. Trapp, D. Reuter, Molecular beam epitaxy growth and temperature-dependend electrical characterisation of carbon doped GaAs on GaAs(111)B, DPG-Tagung, Regensburg (2019).

- **T. Henksmeier**, J.F. Schulz, E. Kluth, M. Feneberg, R. Goldhahn, A. M. Sanchez, M. Voigt, G. Grundmeier, D. Reuter, Remote heteroepitaxy of $In_xGa_{1-x}As$ on GaAs, ICMBE, online conference (2021).

Acknowledgements

To this end I want to express my appreciation to all the people supporting me during my entire PhD studies.

- First of all, I would like to thank Prof. Dr. Dirk Reuter for the opportunity to work in his group and for his guidance during the entire period. I can truly say, he is always available for his students.
- I thank also the Co-Reviewers, Prof. Dr. Artur Zrenner, Prof. Dr. Wolf Gero Schmidt and Dr. Christof Eigner for their effort and time reading the thesis.
- I thank my office mate Falco Meier and the entire work group for their companionship and fruitful discussions.
- I am grateful for the perfect MBE support from Bastian Aisenbrey.
- I thank Anja Blank for her support of any kind of administrative stuff.
- Thanks to Dennis Deutsch, Mario Littmann , Falco Meier and Viktoria Zolantanosha for proof reading and Rebeccah Grotemeyer for spelling check.
- I thank my collaboration partners for helpful measurements and fruitful discussions: Elias Kluth, Johan Friedeman Schulz, PD. Dr. Martin Feneberg for Raman-spectroscopy measurements, Markus Voigt and Prof. Dr. Guido Grundmeier for XPS-measurements and Prof. Dr. Ana Sanchez and Dr. Thomas Riedl for TEM-investigations.
- Last but not least, I want to express my gratitude towards my family, especially my parents and grandparents for any kind of support, especially my granddad. Although he was really curious and interested about my work he cannot see me finishing it. This is for you!

Erklärung der Selbständigkeit

Hiermit versichere ich, Tobias Henksmeier, die vorliegende Arbeit selbständig verfasst und keine anderen als die angegebenen Quellen und Hilfsmittel benutzt, sowie die Zitate kenntlich gemacht zu haben.

Paderborn, 5. November 2021 Tobias Henksmeier